

Metamorphic mineral reactions: Porphyroblast, corona and symplectite growth

FRED GAIDIES^{1,*}, R. MILKE², W. HEINRICH³ and R. ABART⁴

¹ *Department of Earth Sciences, Carleton University, 1125 Colonel By Drive, Ottawa, ON, K1S 5B6, Canada, e-mail: Fred.Gaidies@carleton.ca*

² *Institute of Geological Sciences, Free University Berlin, Malteserstr. 74-100, Haus N Raum N 16 12249 Berlin, Germany, e-mail: milke@zedat.fu-berlin.de*

³ *Helmholtz-Zentrum Potsdam, Deutsches GeoForschungsZentrum (GFZ) Telegrafenberg, D-14473 Potsdam, Germany, e-mail: whsati@gfz-potsdam.de*

⁴ *University of Vienna, Department of Lithospheric Research, Althanstrasse 14, 1090 Vienna, Austria, e-mail: rainer.abart@univie.ac.at*

* *Corresponding author*

Much of the Earth's dynamics is related to mineral reactions in the solid-state. Classically, this is referred to as metamorphic crystallization (Kretz, 1994). Based on the chemical compositions of the phases involved in a metamorphic mineral reaction, two basic reaction types may be distinguished. Reactions that involve only structural re-arrangements, while the compositions of the reactant and product phases are identical, are referred to as partitionless and 'polymorphic phase transformations'. If, in contrast, one or more reactant phases are replaced by one or more product phases with different compositions, this implies that chemical components are supplied to or removed from the reaction interfaces separating the reactants from the product phases. In the absence of advective transport *via* a fluid or melt, the necessary chemical mass transport can occur only by diffusion. Accordingly, this reaction type is partitioning and is referred to as 'diffusive phase transformation'. Some treatments of the kinetics of mineral reactions are based on partitionless polymorphic phase transformations and are reviewed only briefly in this chapter. However, because most metamorphic mineral reactions are partitioning diffusive phase transformations, the following discussion will focus mainly on this reaction type.

In this chapter, three types of reactions that play a key role in metamorphic crystallization are addressed. During prograde metamorphism continuous supply of aqueous fluid by dehydration reactions may facilitate relatively rapid inter-crystalline diffusion so that a state close to chemical equilibrium on the scale of mineral grains and beyond may be attained resulting in 'porphyroblastic mineral growth'. Interface-reaction controlled and diffusion-controlled growth are two end-member models in the kinetics of porphyroblastic growth and differ in terms of the spatial extent of chemical equilibration and its influence on the distribution and compositional zoning of porphyroblasts. The first section of this chapter may serve as a review of some of the key works in metamorphic petrology addressing the factors that control the abundance and size distribution of porphyroblasts and their chemical zoning patterns.

During retrograde stages of metamorphism or during metamorphic overprint of a previously largely dehydrated rock, crystallization may take place in a relatively 'dry' environment, where inter-crystalline diffusion is comparatively sluggish. In such a situation, reaction microstructures such as 'reaction bands' or 'corona structures' may develop. Typically, both the reactant and product phases are present providing evidence of incomplete reaction and indicating an overall disequilibrium situation. Chemical equilibrium may be restricted to microscopic domains along the phase boundaries or may not be attained at all. Nevertheless, important rate and time information may be obtained from the analysis of such reaction microstructures, if the processes underlying their formation are known and their rates are calibrated. The formation mechanisms of reaction bands and corona microstructures are discussed in the second section of this chapter.

Finally, the mechanisms underlying symplectite formation, another phenomenon that is typically associated with metamorphic overprint of magmatic or metamorphic rocks, will be addressed in the third section of this chapter. Symplectites are spatially highly organized, fine-grained intergrowths of two or more different phases, replacing a more coarser-grained precursor phase at a sharp reaction interface. Symplectite microstructures are characterized by a specific length scale of phase alternation, by specific lamellar or rod-shaped microstructure and compositional patterns. In this chapter different avenues for extracting petrogenetic information from symplectite microstructures are discussed.

1. Porphyroblast growth

Porphyroblasts are grains of metamorphic minerals that are characterized by a size significantly larger than that of the matrix phases. The mechanisms and rates of porphyroblastic growth have been the focus of research for more than 50 years and are still an active topic of modern metamorphic petrology (*e.g.* Hollister, 1966; Jones and Galwey, 1966; Kretz, 1966, 1969, 1973, 1974, 1993; Foster, 1981, 1999; Loomis, 1982, 1986; Cashman and Ferry, 1988; Carlson, 1989, 1991b, 2002, 2011; Miyazaki, 1991, 1996, 2015; Spear *et al.*, 1991a; Carlson *et al.*, 1995; Denison and Carlson, 1997; Daniel and Spear, 1998, 1999; Spear and Daniel, 1998, 2001; Hirsch *et al.*, 2000; Gaidies *et al.*, 2008a,b, 2011; Hirsch, 2008; Schwarz *et al.*, 2011; Ketcham and Carlson, 2012; Kelly *et al.*, 2013; Petley-Ragan *et al.*, 2016).

The scenarios developed to describe porphyroblastic growth differ in terms of the assumptions made about the spatial extent of chemical equilibration of the components involved in the respective metamorphic phase transformation and its impact on the size distribution and chemical composition of the porphyroblasts. In general, porphyroblastic growth is understood as the result of the interplay of various atomic-scale processes during the metamorphic phase transformation, including the dissolution of reactants, the attachment and detachment of atoms at the interface between the crystallizing product and its surrounding matrix, and the long-range diffusion of components between the reactant and product sites. The kinetics of porphyroblastic growth are closely related to the energy barriers associated with the interface processes and the diffusion across the bulk system. This is in stark contrast to nucleation, the process that necessarily precedes growth (see Gaidies, 2017, this volume). Whereas the critical energy barrier to nucleation is associated largely with the formation of the interface, energy barriers for growth are associated with the movement of the interface

into the metastable matrix by the interplay of atomic jumps across the interface and long-range diffusion. In general, energy barriers to diffusion may be considered smaller than those for nucleation, possibly explaining the relatively large sizes but low abundances of porphyroblasts in metamorphic rocks.

Commonly, two end-member scenarios of porphyroblastic growth are distinguished: (1) In models of 'interface-reaction controlled growth', long-range diffusion is assumed to be significantly faster than the attachment and detachment processes at the propagating crystal/matrix interface so that chemical disequilibrium is expected to develop only in the vicinity of the interface. (2) 'Diffusion-controlled growth' is assumed to result from interface processes significantly faster than the diffusion across the bulk of the system. In this case, local chemical equilibrium is assumed commonly only at the interface, and gradients in the chemical potentials are expected to develop across the rock matrix as the porphyroblast grows. Because the spatial extent of chemical equilibration influences directly the size distribution and chemical composition of porphyroblasts in natural systems, methods that integrate microstructural and chemical datasets with quantitative models of metamorphic crystallization allow evaluation of the applicability of these end-member scenarios providing insight into the mechanisms and rates of porphyroblastic growth.

In the following, a brief introduction to the kinetics associated with interface reaction and diffusion-controlled crystal growth is provided, and the implications for the microstructural and chemical evolution of porphyroblasts are discussed. Statistical methods developed to investigate the abundance and size distribution of porphyroblasts in three dimensions (3D) are reviewed and examples for the spatial disposition of porphyroblasts in contact and regional metamorphic rocks are presented. In addition, the reader is introduced to the numerical simulation of metamorphic crystallization that may help to decipher metamorphic pressure-temperature-time (P - T - t) paths by considering the microstructural and compositional record contained in the spatial disposition of chemically zoned garnet porphyroblasts.

1.1. Interface-reaction controlled porphyroblast growth

Crystal growth controlled by the rate of attachment and detachment processes at the crystal/matrix interface may be modelled at the atomic level where atoms continuously and independently cross the entire interface. The bulk of these attachment and detachment processes may be referred to as interface-reaction, driven by the drop in the chemical potentials of the atoms as they cross the interface. If the chemical compositions of the phases separated by the interface are identical then the phase transformation is partitionless, and the energetics of the interface-reaction will be a function of the activation energies associated with the atomic jumps across the interface and the thermodynamic driving force for the interface movement. For such a specific case, the formalism outlined by Balluffi *et al.* (2005) for interface-reaction controlled growth during solidification may be used.

According to Balluffi *et al.* (2005), the rate with which the interface moves away from the centre of a spherical stable phase β into the metastable phase α is the growth

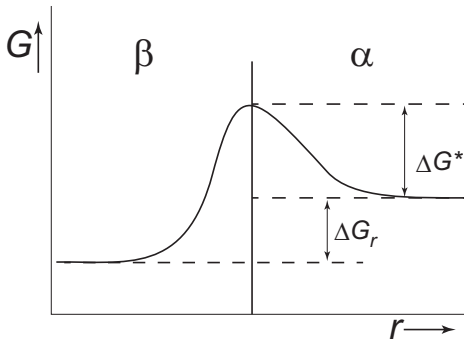


Figure 1. Chemical driving force for growth, ΔG_r , and activation energy associated with the atomic jump from α to β , ΔG^* , at the α/β interface for partitionless interface reaction-controlled growth. Modified after Christian (2002) and Balluffi *et al.* (2005).

rate, dr/dt , where r refers to the spatial coordinate of the interface (Fig. 1). The flux of α atoms across the interface is given by

$$Nv \exp\left(\frac{-\Delta G^*}{k_B T}\right) \quad (1)$$

where N is the total number of atoms per unit area of the interface, v is their vibrational frequency, ΔG^* is the activation energy associated with the jump across the interface, and k_B is Boltzmann's constant. Similarly, and assuming that the vibrational frequencies are identical, the jump frequency associated with the transfer of atoms of β across the interface is given by

$$Nv \exp\left(\frac{-(\Delta G^* + \Delta G_r)}{k_B T}\right) \quad (2)$$

where ΔG_r is the chemical driving force for the interface movement, acting on each atom, and is defined by the difference in the two local minima of the Gibbs energy centred on α and β (Fig. 1). It is important to note that ΔG_r increases with departure from equilibrium reflecting the diffusiveness of the interface and the energy barrier associated with the atomic jumps across it.

The net rate of transfer from α to β is the difference of (1) and (2) which, multiplied by the molecular volume of β , Ω , gives the interface-reaction controlled growth rate

$$\frac{dr}{dt} = Nv \left[\exp\left(\frac{-\Delta G^*}{k_B T}\right) - \exp\left(\frac{-(\Delta G^* + \Delta G_r)}{k_B T}\right) \right] \Omega \quad (3)$$

Rearranging yields

$$\frac{dr}{dt} = Nv \left[\exp\left(\frac{-\Delta G^*}{k_B T}\right) \left[1 - \exp\left(\frac{-\Delta G_r}{k_B T}\right) \right] \right] \Omega \quad (4)$$

which for $\Delta G_r \ll k_B T$ simplifies to

$$\frac{dr}{dt} = M \Delta G_r \quad (5)$$

with the interface mobility, M , defined as

$$M = \frac{\Omega N v}{k_B T} \exp\left(\frac{-\Delta G^*}{k_B T}\right) \quad (6)$$

Note that for the more common case of partitioning phase transformations, the chemical compositions of the phases on either side of the interface are different. Hence, atoms of different components will cross the interface, each with component-specific energy barriers associated with the atomic jumps. In this case, the simple formalism outlined above cannot be used to derive expressions for M , and a phenomenological approach may be used instead.

Expression 5 is strictly valid only for the movement of planar interfaces. A more general expression accounting also for the influence of interface curvature on the overall Gibbs energy change during crystal growth is

$$\frac{dr}{dt} = M \left(\Delta G_r - \frac{2\sigma}{R} \right) \quad (7)$$

where σ is the interfacial energy and R is the radius of interface curvature (see Petrishcheva and Abart 2017, this volume). According to equation 7, for relatively small crystals and reactions close to equilibrium, the bulk energy term may approach values similar in magnitude to the interfacial term so that the thermodynamic driving force effectively acting on the interface decreases, and the growth rate becomes size-dependent reflecting the increase in Gibbs energy with interface curvature. Only in that case, and amplified by large interfacial energies, small crystals will grow slower than larger ones for a given step in time and under the same conditions. In terms of porphyroblastic growth, compositional gradients that develop as the interface moves would be steeper in smaller crystals compared with larger but would be the same for crystals of identical size if these crystals grew simultaneously (Fig. 2), independent of their positions in the rock. Such a scenario, where crystals are smaller than a critical size so that their interface curvatures reduce the thermodynamic driving force for growth, may be referred to as ‘size-dependent interface-reaction controlled growth’.

In most cases, however, interface curvature and the contribution of the interfacial energy term to the Gibbs energy of a crystal during growth may be too small so that the rate with which a porphyroblast grows will be size-independent (see expression 5). As a result, for crystals that are larger than the critical size for size-dependent interface-reaction controlled growth, porphyroblasts will grow with the same radial rate for a given step in time and P - T - X space, and identical compositional gradients will develop, independent of the sizes and positions of the porphyroblasts in the rock (Fig. 2). The interface during ‘size-independent interface-reaction controlled growth’ moves proportional to time according to

$$r \propto t \quad (8)$$

Note that this simple relation holds only if M and ΔG_r can be considered constant, such as for an infinitesimal step in P - T - X - t space. However, as P - T alter during metamorphism, variations in the growth rate of a porphyroblast may be expected

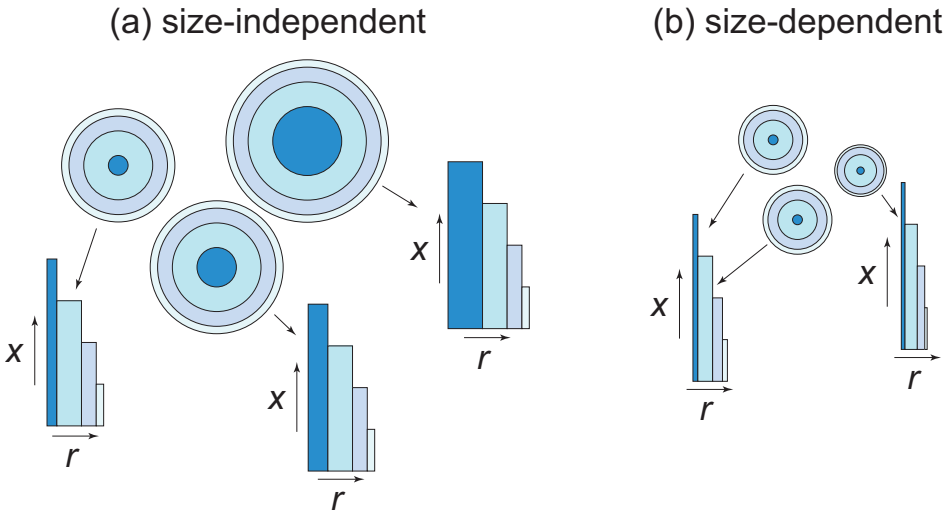


Figure 2. Two possible scenarios of interface reaction-controlled growth: (a) relatively large crystals grow with rates that change proportional to time and chemical driving force, independent of crystal size. (b) Slow growth and steep compositional gradients of small crystals due to the large interface curvature reducing the driving force for growth at any point in time. In both cases, growth rates are position-independent.

reflecting changes in the interface mobility and the chemical driving force for growth. The chemical driving force for growth relates directly to the thermodynamically effective bulk-rock composition so that chemical fractionation, commonly associated with the growth of refractory phases such as garnet or plagioclase may also influence the growth rate of a porphyroblast.

The departure from equilibrium at the interface between porphyroblast and matrix during interface reaction-controlled growth reflects the kinetics of the interface processes relative to the change of the thermodynamic driving force that acts on the interface during metamorphism. If the interface processes are fast relative to the change of the chemical driving forces for porphyroblastic growth then chemical reaction may be close to equilibrium and crystal growth may be modelled as a succession of equilibrium states. Scenarios where significant degrees of disequilibrium at propagating interfaces may be expected include porphyroblastic growth in rocks subjected to relatively fast changes in the chemical driving force for growth, and containing a fluid phase along their grain- and phase-boundary networks facilitating rapid long-range diffusion, such as during prograde metamorphism of pelites in contact aureoles.

1.2. Diffusion-controlled porphyroblast growth

If long-range diffusion of nutrients and waste products is sufficiently slow compared to their attachment and detachment at the interface as the porphyroblast grows, then gradients in the chemical potentials of the associated chemical components will

develop across the rock matrix, and the composition of the matrix at the interface will be position-dependent. The rate of growth will then be controlled by the diffusion of components through the matrix surrounding the porphyroblast associated with the supply of nutrients and the removal of waste products. It is important to note that if the long-range diffusion of a component controls the rate of porphyroblastic growth but the component itself does not mix on a crystallographic site of the porphyroblast then the chemical composition of the porphyroblast may be position-independent. Assuming local equilibrium at the interface and ignoring any influence of interface curvature on the Gibbs energy of a crystal, the classic formalism by Zener (1949) may be adopted to derive an expression for the rate of diffusion-controlled spherical growth. More general expressions for diffusion-controlled growth involving solution phases and considering finite interface mobilities for different geometries are discussed in sections 2 and 3 of this chapter.

According to Zener (1949), c_i^α and c_i^β may be referred to as the equilibrium concentrations of component i at the interface of the matrix and porphyroblast, respectively (Fig. 3), and D_i may be the diffusivity of i through the matrix, so that

$$(c_i^\beta - c_i^\alpha)dr = D_i \left(\frac{\partial c_i}{\partial r} \right) dt \quad (9)$$

Rearrangement results in the kinetic law for diffusion-controlled spherical growth in an infinite matrix

$$\frac{dr}{dt} = \frac{D_i}{(C_i^\beta - C_i^\alpha)} \left(\frac{\partial C_i}{\partial r} \right) \quad (10)$$

assuming that differences in the molecular volumes of α and β can be ignored. Following Zener (1949), r varies with t according to

$$r = \alpha \sqrt{D_i t} \quad (11)$$

with α defined as

$$\alpha = K \frac{\sqrt{c_i^\infty - c_i^\alpha}}{\sqrt{c_i^\beta - c_i^\infty}} \quad (12)$$

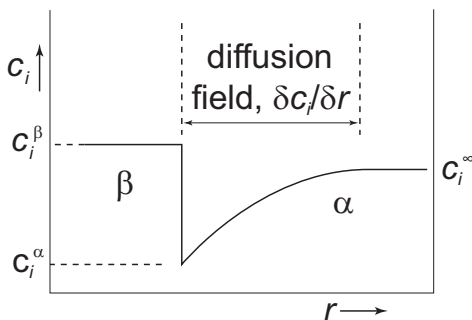


Figure 3. Diffusion-controlled partitioning growth of an isolated grain of stable β at the expense of an infinite metastable α matrix assuming local equilibrium with respect to component i at the α/β interface. Modified after Zener (1949).

and K varying between 1.4 and 2.4 as c_i^∞ varies between c_i^α and c_i^β . In other words, the interface during diffusion-controlled growth moves proportional to the square root of time whereas a linear growth law is obtained for size-independent interface reaction-controlled growth (see expression 8).

The compositional gradient in the vicinity of the porphyroblast, $\partial c_i / \partial r$, controls the rate of diffusion-controlled interface movement, and decreases with an increase of porphyroblast size. This decrease in compositional gradient is related to the width of the diffusion field surrounding the porphyroblast (Fig. 3) which is wider for larger grains compared to smaller ones. As a result, diffusion-controlled growth is size-dependent, with smaller grains growing with a greater radial growth rate than larger ones. In contrast to interface reaction-controlled growth, chemical potential gradients develop in the rock matrix during porphyroblastic growth controlled by long-range diffusion (*e.g.* Carlson, 1989, 1991; Carlson *et al.*, 1995). Both the radial growth rates and the compositional gradients that develop in the porphyroblast as it grows reflect the positions and orientations of the interfaces in the diffusion zone. Hence, initially similarly sized grains may grow with different rates according to the local diffusion field, and may develop asymmetric compositional gradients as governed by the varying availability of nutrients along their interfaces. Systematic variations in the chemical potential gradients across diffusion fields around porphyroblasts with uneven surfaces may result in the morphological instability of these surfaces. Gradients in the metastable matrix may be steeper in the vicinity of protruding elements of the porphyroblast surface compared with flat surface areas. This leads to locally increased diffusive fluxes of the nutrients towards the growth front resulting in growth rate variations along the interface, amplifying the protrusions and, hence, destabilizing flat surfaces (Mullins and Sekerka, 1964). Because morphological instability of growth fronts and dendritic growth are uncommon during porphyroblast growth in metamorphic rocks, Miyazaki (2015) questions the significance of the diffusion-controlled growth scenario in the kinetics of porphyroblast crystallization.

1.3. Statistical analysis of the spatial disposition of crystal centres and sizes

The spatial distribution of porphyroblast centres and sizes may provide insight into the kinetics of associated metamorphic mineral reactions (*e.g.* Kretz, 1974; Carlson, 1989). For example, a ‘random spatial distribution’ of porphyroblast sizes may be expected to develop during interface reaction-controlled growth because the rates of porphyroblast growth would be independent of the positions of the crystals in this kinetic scenario. Furthermore, if the energetically preferable nucleation sites (see Gaidies, 2017, this volume) are distributed uniformly across the rock volume then a random distribution of porphyroblast centres may also be envisaged during interface reaction-controlled kinetics. Interactions between neighbouring crystals during interface-reaction controlled growth take place only if nucleation sites are close to each other so that the crystals impinge as their interfaces move. Hence, deviations from a random spatial disposition of porphyroblast centres may be expected only if preferable nucleation sites or chemical components are distributed inhomogeneously, such as during the static metamorphism of sedimentary layering. In such a case, the number of crystal centres

for a given rock volume may be significantly larger than in a random distribution and the spatial pattern may be referred to as 'clustered'.

A random spatial distribution of porphyroblast centres and sizes may also develop during diffusion-controlled porphyroblast growth but only at length scales between neighbouring crystals exceeding the effective diffusion length. For shorter length-scales, an ordered texture is expected to form during diffusion-controlled growth as a consequence of the competition for nutrients between porphyroblasts (*e.g.* Carlson, 1991). This ordering is characterized by a positive correlation between the sizes of porphyroblasts and their distances to each other caused by the interference of diffusion fields of neighbouring crystals. Whereas the decrease of porphyroblast size with a decrease of next-neighbour distance may indicate diffusion-controlled growth, the positive correlation of the distance between porphyroblasts and their abundances may reflect diffusion-controlled nucleation.

In order to study the 3D distribution of porphyroblasts statistically, X-ray computed tomography (XR-CT) (*e.g.* Ketcham and Carlson, 2001) is commonly used as it allows investigation of the relatively large rock volumes required for statistically meaningful analyses (*e.g.* Chernoff and Carlson, 1997, 1999; Petley-Ragan *et al.*, 2016). The methods developed to conduct the statistical analyses of the spatial distribution of crystals utilize microstructural information, such as the *x-y-z* coordinates of each grain centre, grain radius or semi-major axis. *Reduce3D* (Hirsch *et al.*, 2000; Hirsch, 2011) may be the most advanced software to conduct sophisticated statistical analyses of porphyroblast distributions. In the following, the theoretical background of the most useful statistics commonly applied to the study of the spatial disposition of porphyroblasts is reviewed and examples of applications to natural rocks are discussed.

1.3.1. Theoretical background

In the statistical analysis of the spatial distribution of porphyroblast centres and sizes, single-scale and scale-dependent statistics have been applied. These statistics have been used to determine whether the porphyroblasts of a given volume of rock can be characterized by a clustered, random or ordered spatial distribution (*e.g.* Kretz, 1973, 1993; Carlson, 1989; Denison and Carlson, 1997) aiding in the analysis of the kinetics of porphyroblastic growth. A fundamental assumption in the interpretation of the pattern statistics is that the spatial distribution of crystal centres and sizes is a result of nucleation and growth and is not modified by secondary processes such as resorption or relative displacement associated with deformation.

The single-scale statistics commonly used in the pattern statistics include the ordering and clustering indices (Kretz, 1966, 1969), and the impingement and isolation indices (Carlson, 1989; Hirsch, 2000). A limitation of the single-scale statistics is their inability to consider variations in the spatial distribution of porphyroblasts with distance because they reflect global averages of microstructural observations such as porphyroblast size and distances between porphyroblasts across the rock volume studied. Hence, the more sophisticated approaches inherent in scale-dependent correlation functions such as the *L'*-function (*L'*F), the pair correlation function

(PCF) and the mark correlation function (MCF') (e.g. Daniel and Spear, 1999) are preferred to the single-scale measures (Carlson, 2011). These scale-dependent correlation functions allow for the quantification of textural relationships across a range of length scales instead of global averages. The most useful scale-dependent correlation functions may be the PCF and MCF' as they can be used to quantify the 3D distribution of porphyroblast centres and sizes for any test distance across the rock volume of interest. These correlation functions will be outlined below. Additional information about other scale-dependent statistics, such as the L'-function, or the single-scale statistics may be found in Daniel and Spear (1999) and Hirsch *et al.* (2000).

In *Reduce3D* (Hirsch *et al.*, 2000; Hirsch, 2011), both the PCF and MCF' statistics of the natural dataset are compared with the statistics obtained through the numerical simulation of interface reaction-controlled non-clustered nucleation and spherical growth. The number density of the crystals as well as the size and shape of the sample volume and the crystal size frequency relationships used in the simulation are identical to the natural dataset. However, the numerical simulation produces a crystal array which lacks any ordering and clustering trends so that the corresponding statistics can be used as a null hypothesis case. Any deviations in the statistics of the natural crystal array compared to the null hypothesis case may then be interpreted to indicate either clustering or ordering providing insight into the mechanisms and rates of porphyroblast crystallization. The shaded regions in the diagrams produced with *Reduce3D* represent the 2σ range obtained from 100 simulations of interface reaction-controlled non-clustered spherical crystallization. Examples of these ranges are illustrated as envelopes in Figs 4 and 5.

The artificial array of spherical crystals produced by *Reduce3D* in order to simulate non-clustered interface reaction-controlled nucleation and growth may be considered a random spatial distribution of crystal centres and sizes for distances at which these

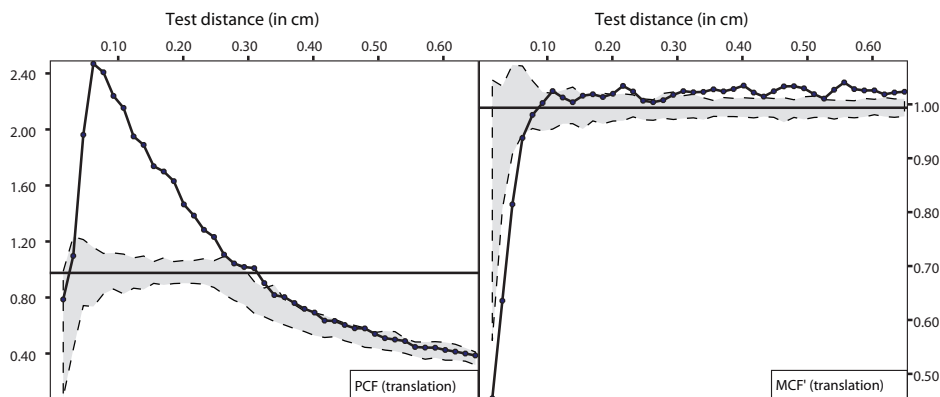


Figure 4. Results of spatial statistical correlation functions (PCF and MCF') calculated with *Reduce3D* (Hirsch, 2011) for garnet in a metapelite from the Lesser Himalayan Belt in Sikkim, India (24-99 of Gaidies *et al.*, 2015). The blue band corresponds to theoretical results (with 2σ envelope) obtained for a random distribution of spheres. Sphere-normalized radius is used as mark.

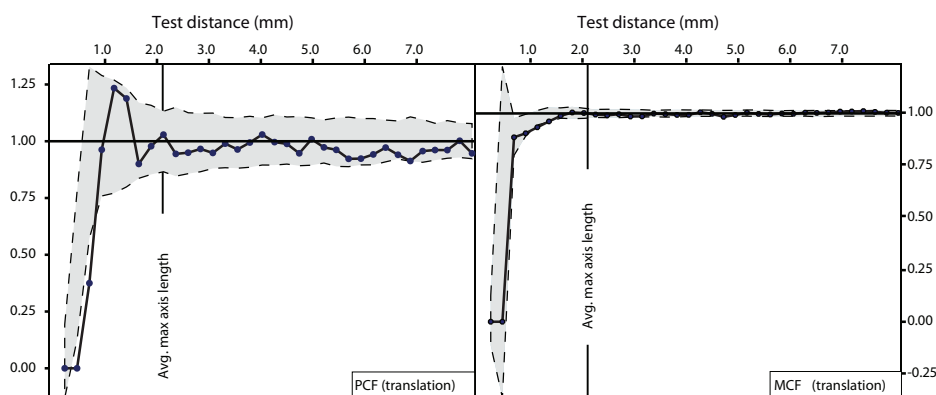


Figure 5. Statistical results of PCF and MCF' calculations for cordierite in a hornfels from the Bugaboo contact aureole (Petley-Ragan *et al.*, 2016) using *Reduce3D* (Hirsch, 2011). The blue areas correspond to a random distribution of porphyroblasts (with 2σ envelope). Sphere-normalized radii are used for the calculation of PCF, and the semi-major axes are used for the MCF'.

crystals do not touch. However, there is always a deviation from randomness towards ordering at shorter distances even in the artificial array. The ordering with respect to the distribution of crystal centres is due to the 'volume effect' where crystals cannot nucleate inside a pre-existing crystal. This effect results in a decrease in the number of crystal centres with a decrease in test distance for scales shorter than the average diameter of the crystal population. Ordering with respect to the size of crystals at distances shorter than the average crystal size is a result of the 'Strauss hard-core process' (Strauss, 1975; Ripley, 1981; Baddeley and Turner, 2000; Illian *et al.*, 2008). This process results in an ordered pattern in a population of objects in 3D at length scales at which these objects touch each other. It is characterized by a positive correlation between the sizes of the objects and the distances between their centres because the centres of the objects can only get closer to each other if the sizes of the objects decrease. Accordingly, in a population of differently sized spheres, the Strauss hard-core process results in ordering at length scales less than the average diameter of the spheres.

The volume effect and Strauss hard-core process are considered in the numerical simulation of non-clustered interface reaction-controlled nucleation and growth by *Reduce3D* based on the assumption that crystals can be approximated as spherical objects. Accordingly, the largest crystals are placed at random positions in the model rock volume, and the remaining space is filled successively with crystals of decreasing size. This is in line with a nucleation and growth algorithm where the final sizes of the crystals reflect the time of their nucleation. Such a crystallization sequence may be expected during interface reaction-controlled growth assuming that secondary processes such as resorption or deformation did not alter crystal sizes. During the random placement of successively smaller crystals, *Reduce3D* tests whether crystal centres are positioned within the model volume occupied by previously placed crystals.

Such a placement is permitted by the software but only if the distance between the centres of the overlapping crystals is equal to or larger than the difference of their radii effectively simulating the formation of interpenetrating crystal pairs. If the distance between the centres of the overlapping crystals is smaller than the difference of their radii then the placement is not permitted and new random positions are tested until this placement criterion is fulfilled. Additional tests are run by the software to minimize the error that forms if highly interpenetrating crystal pairs are misidentified as larger single crystals in the 3D dataset.

Pair correlation function, PCF. The pair correlation function, $g(r)$, is a measure of the number of crystal centres, n , within a spherical shell volume of the sample region, $V(W)$, which increases with test distance, r , around the centre of each crystal i . It is defined as (Hirsch *et al.*, 2000)

$$g(r) = \frac{\rho(r)}{\lambda^2} \quad (13)$$

where $\rho(r)$ is given as

$$\rho(r) = \sum_{i=1}^n \sum_{\substack{j=1 \\ (j \neq i)}}^n \frac{e_h(t)}{4\pi r^2} \quad (14)$$

with

$$t = r - \|\vec{x}_i - \vec{x}_j\| \quad (15)$$

and

$$\lambda^2 = \frac{n(n-1)}{[V(W)]^2} \quad (16)$$

$\|\vec{x}_i - \vec{x}_j\|$ is the distance between crystals i and j , and $e_h(t)$ is the Epanecnikov kernel function of bandwidth h , given by

$$e_h(t) = \frac{3}{4h} \left(1 - \frac{t^2}{h^2} \right) \text{ for } |t| \leq h \quad (17)$$

With $h = c\lambda^{-1/2}$ and c commonly ranging between 0.1 and 0.2. The Epanecnikov kernel function is 0 where $|t| > h$.

The sample region W increases with test distance to account for the change in crystal abundance as the shell volume grows. This is done around each crystal to achieve an average statistic for each test distance. The thickness of the spherical shell is determined by h allowing all crystal centres within the shell to be considered. Crystals closer to the middle of the shell are weighted more heavily than those that fall close to the outer edge of the shell. PCF values >1 for a given test distance reflect a greater abundance of crystal centres compared to a random distribution at that length scale. Such a result indicates clustering of crystal centres at the corresponding test distance,

possibly indicating the uneven distribution of energetically preferable nucleation sites or chemical heterogeneities. PCF values of <1 for test distances larger than the average diameter of the crystal population result from crystal centre abundances which are smaller than expected in a random distribution indicative of an ordered pattern. Ordering at test distances shorter than the average diameter of the crystal population needs to be compared to results obtained from the numerical simulations of non-clustered interface reaction-controlled nucleation and growth. Values <1 that are positioned below the 2σ envelope may then be unrelated to the volume effect and may be interpreted to reflect ordering due to the suppression of nucleation in the diffusion fields of porphyroblasts associated with diffusion-controlled crystallization.

Mark correlation function, MCF'. The MCF' is similar to the PCF in that it also accounts for crystals present within a spherical shell around each crystal modelled using the Epanecnikov kernel function, e_h . In addition, the MCF' allows us to consider a crystal feature, or mark, such as radius or volume.

The mark correlation function, $k(r)$, is defined as (Hirsch *et al.*, 2000)

$$k(r) = \frac{\kappa_{mm}(r)}{\kappa_{mm}(\infty)} \quad (18)$$

with

$$\kappa_{mm}(r) = \frac{\rho_{mm}(r)}{\rho(r)} \quad (19)$$

and

$$\kappa_{mm}(\infty) = \bar{m}^2 \quad (20)$$

where \bar{m} is the arithmetic mean value of the mark for the entire crystal population. $\rho_{mm}(r)$ is defined as

$$\rho_{mm}(r) = \sum_{i=1}^n \sum_{\substack{j=1 \\ (j \neq i)}}^n \frac{m_i m_j e_h(t)}{4\pi r^2} \quad (21)$$

where m_i is the mark value of the i th crystal. Hence, the MCF' allows comparison of the arithmetic mean value of the mark for crystals separated by a certain test distance with the arithmetic mean mark value for the entire population. For example, if radius is used as the mark, and the mean radius of the crystals separated by a certain test distance is smaller than the mean radius of the population then the MCF' value will be <1 . Such a statistic can be expected as a result of Strauss hard-core ordering at test distances shorter than the average diameter of the crystal population. In case the MCF' value is less than those of the 2σ envelope for that test distance then Strauss hard-core ordering is not responsible for this pattern. Instead, a reduction in porphyroblast growth rates associated with the interference of diffusion fields of neighbouring crystals may be inferred. Such a scenario may be expected if porphyroblast growth is diffusion-

controlled. MCF' values larger than 1 are indicative of relatively large crystals at that test distance compared to the arithmetic mean mark value of the entire crystal population.

Strauss hard-core ordering in populations of non-spherical objects. Because crystals are non-spherical objects, Strauss hard-core ordering develops at distances equal to and less than the length of the average major axis of their best fit ellipsoids as those distances are the longest length scales at which crystals touch (Petley-Ragan *et al.*, 2016). This phenomenon develops in any population of non-spherical hard objects independent of the shape-orientation of the objects, and is not related to diffusion-controlled crystal growth. According to Petley-Ragan *et al.* (2016), there is a weakness in the correlation functions when applied to crystals if the sphere-normalized radius of these crystals is used as mark in the statistics calculations (*e.g.* Carlson, 1989; Daniel and Spear, 1999; Hirsch *et al.*, 2000; Ketcham *et al.*, 2005; Hirsch and Carlson, 2006; Hirsch, 2008). Because the length of the major axis of a non-spherical object exceeds that of the corresponding sphere-normalized diameter, Strauss hard-core ordering operates at length scales larger than the sphere-normalized diameter in a crystal population. Hence, if a sphere-normalized radius were to be used as a mark in the statistics calculations, the scale of ordering through the Strauss hard-core process would be underestimated and its characteristic ordered pattern may, incorrectly, be interpreted to be the result of diffusion-controlled growth. For this reason, Petley-Ragan *et al.* (2016) advocate the use of the semi-major axes of ellipsoids fitted around porphyroblasts as mark instead to account correctly for the Strauss hard-core process and its influence on the spatial distribution of porphyroblasts.

1.3.2. Selected examples of statistical analyses of porphyroblast distributions

Garnet is the prime mineral for the statistical analysis of the spatial distribution of porphyroblasts (*e.g.* Denison *et al.*, 1997; Daniel and Spear, 1999; Hirsch *et al.*, 2000; Ketcham *et al.*, 2005; Hirsch and Carlson, 2006; Hirsch, 2008; Gaidies *et al.*, 2015) given its key importance for the determination of metamorphic *P-T-t* trajectories (*e.g.* Spear, 1993), and because its specific attenuation properties allow it to be detected easily by XR-CT (Denison *et al.*, 1997). Other porphyroblastic phases investigated texturally using XR-CT and 3D pattern statistics include biotite (Hirsch and Carlson, 2006; Petley-Ragan *et al.*, 2016) and cordierite (Petley-Ragan *et al.*, 2016).

Figure 4 illustrates the results of PCF and MCF' calculations applied to a garnet population in a metapelite from the Barrovian garnet zone of the Lesser Himalayan Belt in Sikkim, India (sample 24-99 of Gaidies *et al.*, 2015). The total number of crystals considered for the calculations presented is 1000, and the dimensions of the prismatic sample volume investigated are $\sim 2.5 \text{ mm} \times 20 \text{ mm} \times 20 \text{ mm}$. Garnet is significantly clustered at distances of $< \sim 3 \text{ mm}$ (PCF) and is characterized by a positive correlation between size and nearest neighbour distance for test distances of $< 0.8 \text{ mm}$ (MCF'). Whereas the clustering may reflect an inhomogeneous distribution of nucleation sites or nutrients for garnet crystallization at the respective length scales, the positive correlation of size and position may reflect ordering due to diffusion-controlled growth

as it is developed at length scales larger than Strauss hard-core ordering. Strauss hard-core ordering is expressed in the drop to low statistical values of the null hypothesis envelope at test distances $< \sim 0.7$ mm (Fig. 4). If the ordering of garnet obtained at test distances of < 0.8 mm reflects the interference of diffusion fields during growth of neighbouring crystals then the length scale of ordering may be interpreted as corresponding to the effective width of the diffusion fields. However, it is important to note that the sphere-normalized radii of the garnet porphyroblasts were used for the simulation of Strauss hard-core ordering in this sample. A possible deviation from sphericity of garnet may have increased the length scales at which Strauss hard-core ordering operated (Petley-Ragan *et al.*, 2016) and may not be considered in the statistical results obtained. In addition, resorption or syn- and post-metamorphic deformation may have modified the spatial distribution of garnet grain centres and sizes, which is not considered in the statistical analyses. The drop below values of one in the PCF for test distances $> \sim 3$ mm in both the simulated and natural array (Fig. 4), reflects test distances exceeding the length of the shortest sample dimension.

Whereas evidence for interface reaction-controlled garnet crystallization during regional metamorphism was presented by Daniel and Spear (1999), based on the statistical analysis of the 3D spatial distribution of porphyroblast centres and sizes integrated with compositional zoning data of garnet in rocks from NW Connecticut (USA), diffusion-controlled porphyroblastic growth may be an appropriate end-member scenario for the prograde crystallization of garnet in other regional metamorphic areas (*e.g.* Carlson, 1989; Denison and Carlson, 1997; Spear and Daniel, 2001). This suggests that variations in the thermal or deformational history of rocks may have a significant influence on metamorphic reaction kinetics.

Based on the analysis of the size distribution and compositional zoning of garnet in contact-metamorphic schists from the cordierite zone of a low- P thermal dome near Yellowknife (Canada), Kretz (1993) concluded that porphyroblastic growth was interface reaction-controlled. In a recent study, Petley-Ragan *et al.* (2016) also investigated contact metamorphic rocks. In their study, the spatial distribution of biotite and cordierite porphyroblasts in a hornfels from the contact aureole of the Bugaboo Batholith (SE British Columbia) was analysed. The PCF and MCF' statistics of the cordierite population obtained in that study are illustrated in Fig. 5 and indicate a random spatial disposition of porphyroblast centres (PCF) and sizes (MCF') across all scales investigated. Values below the null hypothesis envelope at small test distances when using the PCF are due to incorrect considerations of the Strauss hard-core process by this correlation function and are not related to diffusion-controlled crystallization (Petley-Ragan *et al.*, 2016). The statistics of the biotite population in the same rock allow for a similar interpretation (Petley-Ragan *et al.*, 2016) indicating that long-range diffusion of nutrients was relatively fast so that diffusion fields around cordierite and biotite crystals did not play a critical role in the spatial disposition of the porphyroblasts. This may indicate that interface processes were either significantly slower than long-range diffusion of nutrients, so that a departure from equilibrium developed only at the interfaces, or that both short and long-range diffusion were fast

relative to the rate with which T changed during contact metamorphism resulting in metamorphism close to equilibrium. A final answer to these questions is largely dependent on appropriate thermodynamic descriptions of the equilibrium phase relations in metapelites at the low metamorphic P associated with the contact metamorphism. Only in that case can observed mineral assemblages and compositions be compared with the predicted equilibrium phase relations. However, systematic incongruities between observed and predicted phase equilibria in the low- P metapelites from the Bugaboo contact aureole indicate that modifications to some of the available thermodynamic models may still be required (Pattison and Debuhr, 2015).

1.4. Quantitative modelling of porphyroblastic garnet crystallization

Given its abundance in metamorphic rocks and its common chemical and isotopic zoning, garnet is arguably the most valuable porphyroblastic phase from which to infer the physicochemical environment of metamorphism (e.g. Spear, 1993; Ague and Carlson, 2013). Quantitative models of porphyroblast crystallization have been developed to predict the compositional zoning that develops in garnet in response to variations in the P - T - X conditions of metamorphism (e.g. Cygan and Lasaga, 1982; Loomis, 1982, 1986; Loomis and Nimick, 1982; Spear *et al.*, 1991b; Konrad-Schmolke *et al.*, 2008). The *DiffGibbs* software (Florence and Spear, 1991; Spear and Florence, 1992; Spear *et al.*, 1991b) was one of the first models designed to predict the zoning of garnet for specified P - T - t paths accounting for chemical fractionation associated with garnet crystallization and intragranular diffusion.

Similar to *DiffGibbs* but based on Gibbs energy minimization, the *THERIA_G* software (Gaidies *et al.*, 2008a) predicts the compositional zoning of garnet that develops during growth along a metamorphic path in P - T - X space considering chemical fractionation, intragranular diffusion in garnet, and diffusional fluxes between garnet and the rock matrix. However, *THERIA_G* differs from all previous models in that it allows the consideration of nucleation and growth of garnet. Hence, the compositional zoning that may develop in an entire garnet population during metamorphism can be predicted and compared with observations in natural samples allowing for a deeper understanding of porphyroblast crystallization.

Gibbs energy minimization (de Capitani and Brown, 1987) is used in *THERIA_G* at any point in P - T - X space to calculate the thermodynamically stable phase relations, such as the chemical compositions and volumes of all the phases present in the stable assemblages. If garnet is part of the thermodynamically stable phase assemblage then circular shells are added to all pre-existing grains according to the implications of size-independent interface reaction-controlled porphyroblastic growth (see expression 5). In other words, garnet is modelled to grow with a radial rate independent of size assuming that interface curvature does not influence the growth rate. The influences of changes to the chemical driving force for porphyroblastic growth, ΔG_r , and interface mobility, M , on garnet growth rate during metamorphism cannot be modelled because chemical equilibrium is not only considered across the rock matrix but also at the garnet/matrix interfaces. Consequently, *THERIA_G* does not account for both long-

range diffusion and interface reaction, but models the evolution of a metamorphic system where chemical disequilibrium is developed only across the garnet porphyroblasts which grow with rates controlled solely by the rate at which the model system propagates through P - T - X space. The compositional gradients that develop in each garnet porphyroblast are constrained by the equilibrium volume and composition of garnet that forms along the P - T - X - t path, the number of garnet crystals per size class, and intracrystalline diffusion. Based on the assumption that bigger crystals nucleated earlier than smaller ones, *THERIA_G* nucleates garnet in pulses where the garnet density of each nucleation pulse is given by the observed number of garnet crystals per size class. A new nucleation pulse starts once garnet grows to a radius that corresponds to the size of the respective radius class. A departure from equilibrium associated with nucleation is not considered.

THERIA_G has been applied successfully to identify the metamorphic P - T - t paths responsible for the compositional zoning in garnet and metamorphic mineral parageneses observed in rocks from different metamorphic terrains (e.g. Gaidies *et al.*, 2008b,c; Hoschek, 2013; Moynihan and Pattison, 2013; Cutts *et al.*, 2014). A recent example of its application to schists of the Barrovian garnet and staurolite zones of the Lesser Himalayan Belt in Sikkim (India) is given in Fig. 6 (Gaidies *et al.*, 2015). The mineral assemblages and compositional zoning of garnet predicted with *THERIA_G* match observations remarkably well suggesting that porphyroblastic nucleation and growth close to equilibrium is a valuable model assumption to obtain high-quality P - T information even for the short timescales associated with the metamorphism during the Himalayan orogeny.

On the other hand, timescales associated with the metamorphism in Sikkim were too short for chemical diffusion to modify substantially garnet growth-zoning in the rocks from the garnet and staurolite zones. Research by George and Gaidies (2016) indicates that crystals from the garnet zone with a radius as small as 200 μm preserved their primary compositional zoning reflecting heating and cooling rates in excess of 100°C/Ma in accordance with independent results based on Lu-Hf garnet geochronology (Anczkiewicz *et al.*, 2014). According to George and Gaidies (2016), the major element concentrations in the rims of the entire garnet population are identical, suggestive of sample-scale equilibration with respect to these elements at the time of cessation of garnet crystallization. Furthermore, garnet crystals of equal size developed equivalent compositional zoning patterns independent of their positions in the rock, and compositional gradients gradually steepen in progressively smaller crystals. These findings may point to size-dependent porphyroblastic growth rates due to an increase of interface curvature for grains that crystallized relatively late during metamorphism, possibly indicating exceedingly small driving forces for porphyroblastic growth or relatively high interfacial energies, according to expression 7.

To conclude this section we note that both the microstructural features such as the spatial disposition and size-distribution of porphyroblasts as well as their chemical zoning, including its possible position dependence bear valuable petrogenetic information. Once nucleation has occurred, the growth of porphyroblasts may be

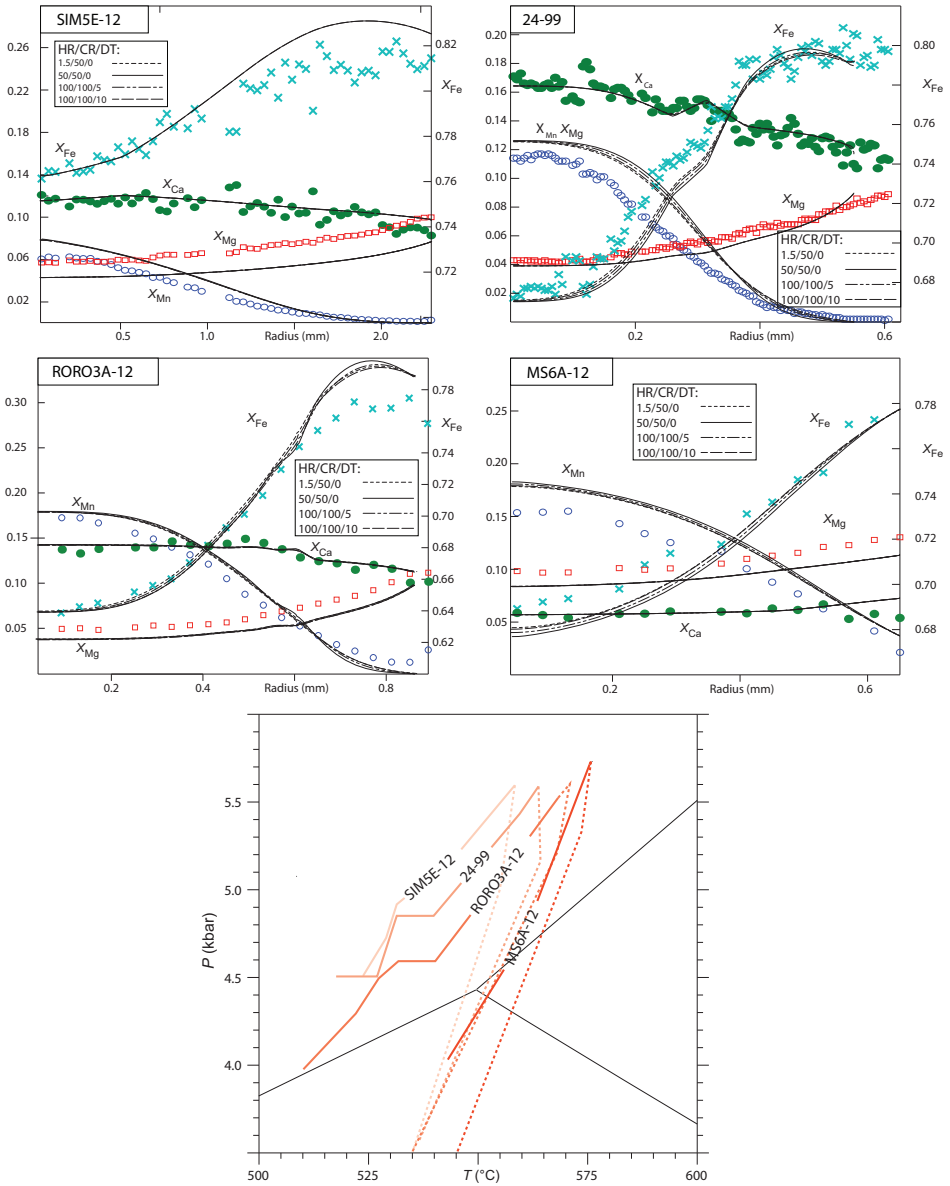


Figure 6. The observed compositional zoning of garnet (symbols) from the Lesser Himalayan Belt of Sikkim (modified after Gaidies *et al.*, 2015) vs. the zoning predicted with $THERIA_G$ (Gaidies *et al.*, 2008a) for different heating and cooling scenarios, and the corresponding metamorphic P - T paths. HR = heating rate, and CR = cooling rate (both in $^{\circ}C/Ma$), DT = dwell time (in Ma).

described by a continuum between two end-member processes represented by interface reaction-controlled and diffusion-controlled growth. Due to its refractory nature, its compositional variability and widespread occurrence, garnet is the most versatile mineral for reconstructing P - T - t trajectories of metamorphic rocks. The integrated analysis of the microstructural features and chemical zoning of garnet populations in metapelitic rocks from different geological environments allows reconstruction of metamorphic conditions with unprecedented accuracy. The task is demanding in terms of material characterization and data reduction. However, advances in instrumentation and increasing computational ability combined with more accurate thermodynamic and kinetic data greatly foster this integrated approach.

2. Interlayer growth – corona formation

When two phases or phase assemblages of different composition that cannot coexist stably are in contact, they may react to form a new phase or phase assemblage. When the product phase or phase assemblage takes the form of a layer or a sequence of layers along the interface between the reactant phases or phase assemblages, the process is referred to as ‘interlayer growth’. In mineralogy the corresponding phenomenon is known as ‘corona’ (Fig. 7a), ‘reaction rim’ (Fig. 7b) or ‘metasomatic reaction band’ (Fig. 7c) (Spry, 1969; Vernon, 2004). Adopting the terminology of Joesten (1977) we refer to the individual mineralogically distinct zones in a corona or in a reaction band as the *layers*. Reaction bands or coronas may comprise a single layer or a sequence of layers. In most cases, the individual layers are polycrystalline, and they may comprise a single or of several minerals.

The stable coexistence of two phases or phase assemblages that prevailed at some point in time may be terminated by changes in pressure and/or temperature or in any other externally controlled physicochemical parameters. For example, plagioclase and

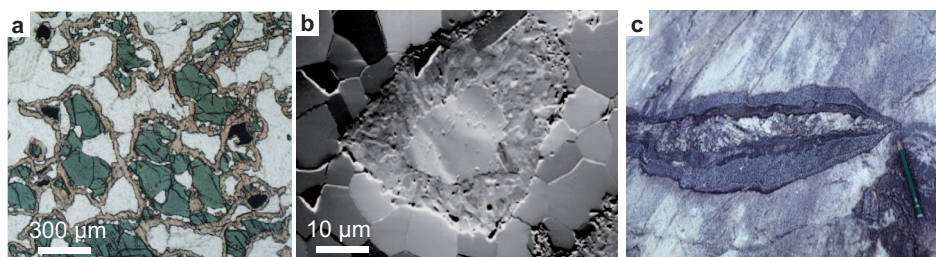


Figure 7. (a) Transmitted light photomicrograph (plane polarized light) of garnet (pale red-grey) + quartz (transparent) coronas at the contacts between plagioclase (transparent) and clinopyroxene (green); sample from Eastern Gats, India, courtesy of M. Raith; (b) forward scatter electron image showing the polycrystalline nature of an experimentally grown enstatite reaction rim produced at 900°C and 1 GPa at forsterite (grain in the centre)–quartz (polycrystalline matrix) interfaces; (c) metasomatic reaction band comprising a tremolite-forsterite layer (inner dark green layer) and a forsterite-calcite layer (outer green layer) between an aplitic dyke (centre) and dolomite marble (host rock); image from Bergell contact aureole, N-Italy.

Fe-Mg-bearing phases such as olivine, orthopyroxene or clinopyroxene may coexist stably at granulite- or amphibolite-facies conditions or during magmatic crystallization, and they may become incompatible and react to form garnet-bearing coronas during eclogite facies overprinting (Joesten, 1986; Ashworth and Birdi, 1990; Johnson and Carlson, 1990; Indares and Rivers, 1995; Bethune and Davidson, 1997; Zhang and Liou, 1997; Cox and Indares, 1999; Keller *et al.*, 2004, 2006, 2008; Larikova and Zaráisky, 2009). The reverse reaction occurring during decompression of eclogites, or high-pressure granulites may produce corona microstructures of Fe-Mg phases such as orthopyroxene or clinopyroxene and plagioclase around garnet (Carlson and Johnson, 1991; Obata, 2011; Obata *et al.*, 2013; Spacek *et al.*, 2013) or plagioclase coronas around kyanite (Tajcmanova *et al.*, 2011). Alternatively, interlayer growth may occur due to the juxtaposition of incompatible rock types such as marble and chert (Joesten and Fisher, 1988; Joesten, 1991; Heinrich, 1993) or of marble and metabasic rocks (Abart *et al.*, 2001; Abart and Sperb, 2001; Fukuyama *et al.*, 2006). The reaction between two incompatible rock types is also known as bimetasomatism or diffusion metasomatism (Korzhinskii, 1959, 1970; Thompson, 1959). Typically, both the reactant and product phases are present in the microstructures produced by interlayer growth indicating that reaction did not go to completion and overall equilibrium was not attained (Carlson, 2002).

Interlayer growth requires that two basic processes occur simultaneously. Because the reactant and product phases have different compositions, interlayer growth requires ‘long-range chemical mass-transfer’ across the layer structure, where the term ‘long range’ refers to distances that are large compared to the typical interatomic spacing. In the absence of migrating melts or fluids, chemical mass-transfer can occur only by diffusion, and in what follows, ‘long-range diffusion’ is implied as the only mode of chemical mass-transport. At the same time, localized reactions must proceed at the ‘reaction interfaces’, which delimit the growing layers on either side. The overall process may be referred to as ‘reactive diffusion’ (Svoboda and Fischer, 2013). Both long-range diffusion and interface reaction may be rate limiting, and the coupling between the two processes determines the overall reaction kinetics.

Much of the basic understanding of interlayer growth dates back to Korzhinskii (1959, 1970) and to Thompson (1959), who applied the concept of ‘local equilibrium’ to derive the chemical potential gradients driving component diffusion from the mineral assemblage zoning across a metasomatic reaction band. Because then, quantitative models for reaction-band and corona formation have been presented by several authors (Fischer, 1973; Frantz and Mao, 1976; Joesten, 1977). In these models long-range diffusion is assumed as the rate-limiting process, and local equilibrium is implied at the reaction interfaces. These models, however, do not provide for deviations from local equilibrium that may arise from additional dissipative processes operating in parallel with long-range diffusion.

In the following, a more general formulation of interlayer growth is presented. To begin with, the kinematic relations linking component fluxes and interlayer growth are addressed and a rate law for diffusion-controlled interlayer growth is derived. In a

second step, the ‘Thermodynamic Extremal Principle’ (TEP) (Onsager, 1931; Ziegler, 1961; Svoboda and Turek, 1991; Svoboda *et al.*, 2005; Martyushev and Seleznev, 2006; Fischer *et al.*, 2014) is applied to derive the corresponding evolution equations that account for additional potentially rate-limiting processes. The TEP is particularly well suited for considering several dissipative processes occurring in parallel, such as the simultaneous operation of long-range diffusion, sluggish interface reactions and non-ideal sources/sinks for vacancies at reaction interfaces and in the bulk. The TEP and some of its applications in materials science are discussed in detail by Svoboda *et al.* (2017, this volume) and only a brief introduction is given here. The TEP is then applied to diffusion-controlled interlayer growth. Finally, the effect of sluggish interface reaction and associated deviations from local equilibrium at the reaction interfaces are addressed in the frame of the TEP.

2.1. The kinematics of interlayer growth

2.1.1. Mass balance at a moving reaction interface

Many mineral reactions involve replacement of a reactant phase by a product phase at a well defined sharp ‘reaction interface’. When the reactant and the product phases have different compositions, the reaction interface can move only when chemical components are supplied to or removed from the reaction interface, implying long-range chemical mass transfer. The velocity of interface motion is related to the component fluxes to and from the reaction interface.

Consider a binary system with components A and B and phases γ and β with compositions $A_{1-X_\gamma}B_{X_\gamma}$ and $A_{1-X_\beta}B_{X_\beta}$, where X_γ and X_β denote mole fractions of component B in phases γ and β , respectively, where $X_\beta > X_\gamma$ (Fig. 8a). Let a γ – β assembly with unit cross-section area extend in x direction, where phase γ to the left and phase β to the right are in contact at an interface extending in the y – z plane (Fig. 8b). Let both components be mobile with component fluxes J_A^γ, J_B^γ and J_A^β, J_B^β in the domains occupied by γ and β , respectively. In general, replacement of one phase by another involves a finite volume change or ‘transformation strain’. As a consequence, the velocity u of the γ – β interface relative to a material point in phase γ is different from the velocity w of the γ – β interface relative to a material point in phase β . Mass balance across the moving γ – β interface requires (Fischer and Simha, 2004)

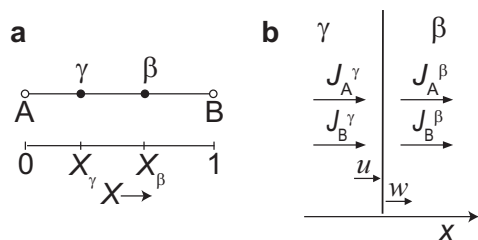


Figure 8. (a) Chemography of a binary system with components A and B and two phases γ and β ; (b) one-dimensional setup with phases γ and β separated by a planar interface perpendicular to the x direction, u and w are the velocities in the x direction of the interface with respect to material points in γ and β , respectively, and $J_A^\gamma, J_B^\gamma, J_A^\beta, J_B^\beta$ are the component fluxes in the domains occupied by the phases γ and β , respectively.

$$\begin{aligned} \frac{1 - X_\gamma}{\Omega_\gamma} w - \frac{1 - X_\beta}{\Omega_\beta} u &= J_A^\beta - J_A^\gamma, \text{ component A,} \\ \frac{X_\gamma}{\Omega_\gamma} w - \frac{X_\beta}{\Omega_\beta} u &= J_B^\beta - J_B^\gamma, \text{ component B} \end{aligned} \quad (22)$$

where Ω_γ and Ω_β denote molar volumes. The expressions on the left hand sides give the rates at which components A and B are consumed or liberated at the moving γ - β interface. The consumption or liberation of components must match the changes in the component fluxes across the interface (right hand side of equations 22). Given that the compositions and molar volumes of γ and β are known, the system of equations 22 provides a relation between interface velocity and component fluxes.

2.1.2. Mass balance during interlayer growth and Kirkendall effect

During interlayer growth the layer of the new phase or the sequence of layers of new phases, in general, grows from the original interface between the reactant phases or phase assemblages into both directions. The corresponding kinematic relations must account for the simultaneous motion of two or more reaction interfaces. We restrict the following discussion to single layer growth; the considerations are, however, similarly applicable to multilayer growth.

Consider the binary system A-B with phases α , β and γ with compositions $A_{1-X_\alpha}B_{X_\alpha}$, $A_{1-X_\beta}B_{X_\beta}$ and $A_{1-X_\gamma}B_{X_\gamma}$, where $X_\alpha < X_\gamma < X_\beta$ (Fig. 9). At $t = 0$ phases α and β extend from $x = 0$ to $x = R_0$, and from $x = R_0$ to $x = +\infty$, respectively. After a short nucleation period a layer of γ grows, and at $t > 0$ the α - γ and the β - γ interfaces are at positions R_α and R_β , respectively, and the original α - β interface is at R_0^* .

In single crystals of ionic substances, diffusion occurs by the motion of ions, and, due to stoichiometric and charge-balance constraints, diffusive fluxes are largely balanced so that $\Sigma \mathbf{J}_i = 0$ (Lasaga, 1998; Glicksman, 2000; Mehrer, 2007). In metals, local charge balance constraints do not apply, and the diffusive fluxes of different components are generally not balanced. The imbalance of component fluxes is compensated by a flux of vacancies \mathbf{J}_0 so that $\Sigma \mathbf{J}_i = -\mathbf{J}_0$. If an ionic substance is polycrystalline such as a mineral layer produced from interlayer growth, electrically neutral components may diffuse, and the component fluxes need not necessarily be balanced. For example the electrically neutral component MgO may diffuse by the simultaneous motion of the charged species Mg^{2+} and O^{2-} , and the resulting flux of MgO is independent of any other diffusive fluxes. Interlayer growth involving decoupled fluxes of neutral components has been reported from different silicate systems (Gardes *et al.*, 2011; Joachim *et al.*, 2011, 2012). To account for the independent diffusion of components we allow for $\Sigma \mathbf{J}_i \neq 0$ and express the relative fluxes of the A and B components as

$$\chi = \frac{J_A}{J_A - J_B} \quad (23)$$

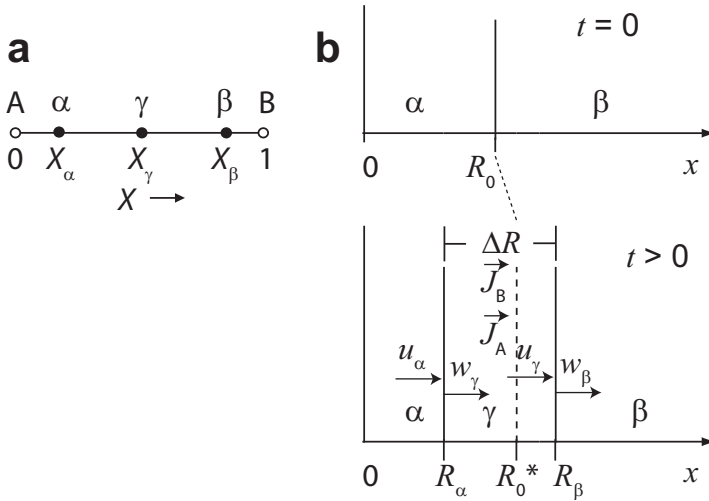


Figure 9. (a) Chemography of binary system with components A and B and phases α , β and γ with compositions $A_{1-X_\alpha}B_{X_\alpha}$, $A_{1-X_\beta}B_{X_\beta}$ and $A_{1-X_\gamma}B_{X_\gamma}$. (b) Model geometry of 1D diffusion-reaction assembly; at $t=0$ phase α occupies the region $0 \leq x \leq R_0$, and phase β occupies the region $x \geq R_0$; at $t>0$ a layer of phase γ forms along the α - β interface; and the α - γ and the β - γ interfaces are at R_α and R_β , respectively; the position of the original α - β interface is indicated by the dashed line labelled R_0^* ; J_A and J_B denote diffusion fluxes of components A and B.

Let phase α be fixed to the global coordinate system. The velocities of the α - γ and the γ - β interfaces are \dot{R}_α and \dot{R}_β , respectively, in the global coordinate system. The interface reactions at the α - γ and the γ - β interfaces do not, in general, conserve volume. As a consequence, the reaction interfaces have different velocities relative to material points in the reactant and product phases. The interface velocities relative to the phases on the left and on the right of the interfaces are denoted u_α , u_γ and w_γ , w_β (Fig. 9). Given that the diffusive fluxes are restricted to the domain occupied by γ , conservation of mass at the α - γ requires (Fischer and Simha, 2004)

$$\frac{(1 - X_\alpha)}{\Omega_\alpha} u_\alpha - \frac{(1 - X_\gamma)}{\Omega_\gamma} w_\gamma = -J_A^{\alpha-\gamma},$$

$$\frac{X_\alpha}{\Omega_\alpha} u_\alpha - \frac{X_\gamma}{\Omega_\gamma} w_\gamma = -J_B^{\alpha-\gamma} \tag{24}$$

and at the γ - β interface it requires

$$\frac{(1 - X_\gamma)}{\Omega_\gamma} u_\gamma - \frac{(1 - X_\beta)}{\Omega_\beta} w_\beta = -J_A^{\gamma-\beta},$$

$$\frac{X_\gamma}{\Omega_\gamma} u_\gamma - \frac{X_\beta}{\Omega_\beta} w_\beta = -J_B^{\gamma-\beta} \tag{25}$$

where $\Omega_\alpha, \Omega_\beta, \Omega_\gamma$ are the molar volumes, and $J_A^{\alpha-\gamma}, J_B^{\alpha-\gamma}$ and $J_A^{\gamma-\beta}, J_B^{\gamma-\beta}$ are the diffusive fluxes at the $\alpha-\gamma$ and the $\gamma-\beta$ interfaces, respectively. If the layer of γ grows only at the reaction interfaces, $J_A^{\alpha-\gamma} = J_A^{\gamma-\beta} = J_A$ and $J_B^{\alpha-\gamma} = J_B^{\gamma-\beta} = J_B$. Referring to equation 23 we note that $J_A = J\chi$ and $J_B = J(\chi - 1)$ and $J_A + J_B = J$. Combining equations 24 and 25 the different interface velocities are expressed in terms of the component fluxes

$$\begin{aligned} u_\alpha &= \Omega_\alpha J \frac{(\chi - 1)(1 - X_\gamma) - \chi X_\gamma}{(1 - X_\alpha)X_\gamma - (1 - X_\gamma)X_\alpha} \\ w_\gamma &= \Omega_\gamma J \frac{(\chi - 1)(1 - X_\alpha) - \chi X_\alpha}{(1 - X_\alpha)X_\gamma - (1 - X_\gamma)X_\alpha} \\ u_\gamma &= \Omega_\gamma J \frac{\chi X_\beta - (\chi - 1)(1 - X_\beta)}{X_\beta(1 - X_\gamma) - (1 - X_\beta)X_\gamma} \\ w_\beta &= \Omega_\beta J \frac{\chi X_\gamma - (\chi - 1)(1 - X_\gamma)}{X_\beta(1 - X_\gamma) - (1 - X_\beta)X_\gamma} \end{aligned} \tag{26}$$

The rate of layer growth is given by

$$\Delta \dot{R} = u_\gamma - w_\gamma = J_A u_A + J_B u_B \tag{27}$$

where

$$\begin{aligned} u_A &= \Omega_\gamma \left(\frac{X_\beta}{X_\beta(1 - X_\gamma) - (1 - X_\beta)X_\gamma} + \frac{X_\alpha}{(1 - X_\alpha)X_\gamma - (1 - X_\gamma)X_\alpha} \right) \\ u_B &= \Omega_\gamma \left(\frac{(X_\beta - 1)}{X_\beta(1 - X_\gamma) - (1 - X_\beta)X_\gamma} + \frac{(X_\alpha - 1)}{(1 - X_\alpha)X_\gamma - (1 - X_\gamma)X_\alpha} \right) \end{aligned} \tag{28}$$

It is seen from equation 27 that the rate of layer growth is related to the fluxes of both components, where the constant parameters u_A and u_B contain only the molar volume of the growing phase γ and the compositions of all three phases.

Recalling that α is fixed to the global coordinate system, the interface velocities in the global coordinate system are given by

$$\dot{R}_\alpha = u_\alpha, \quad \dot{R}_\beta = u_\alpha - w_\gamma + u_\gamma = \dot{R}_\alpha u \tag{29}$$

with

$$u = \frac{\Omega_\gamma}{\Omega_\alpha} \left(\frac{(1 - X_\beta)X_\alpha - (1 - X_\alpha)X_\beta}{X_\beta(1 - X_\gamma) - (1 - X_\beta)X_\gamma} \right) + 1$$

where $u < 0$ for $X_\alpha < X_\gamma < X_\beta$. The rate of layer growth expressed in terms of interface velocity reads

$$\Delta \dot{R} = \dot{R}_\alpha (u - 1) \tag{30}$$

From equation 29 together with the initial condition $R_\alpha(0) = R_\beta(0) = R_0$ the two interface positions are related by

$$R_\beta = u(R_\alpha - R_0) + R_0 \tag{31}$$

Kirkendall effect: The unbalanced flux of components gives rise to the so-called ‘Kirkendall effect’, which describes a net total material transfer relative to a material point in the bulk substance during the interdiffusion of two or more components. The Kirkendall effect was first described for the interdiffusion of copper and zinc in brass, where zinc diffuses faster than copper, and an overall shift of the sample mass relative to an inert marker occurs in the direction of falling zinc concentrations (Smigelskas and Kirkendall, 1947). The Kirkendall effect has also been described in the context of interlayer growth in metal systems (van Loo *et al.*, 2000) and during interlayer growth in silicate systems (Gardés *et al.*, 2011; Joachim *et al.*, 2011, 2012).

The growth rate of an interlayer depends on the fluxes of all components (equation 27), and the fluxes of the individual components cannot, in general, be determined from measured layer-growth rates alone. However, the relative rates at which the two reaction interfaces delimiting a layer on either side move, depend on the individual component fluxes (equations 26). Individual component fluxes can thus be determined, if the position of the so called ‘Kirkendall plane’, that is the trace of the original contact between the reactant phases, is known.

The position of the Kirkendall plane may be evident from discontinuous composition zoning (Fig. 10a) or from a microstructural or textural discontinuity (Fig. 10b) within a layer (Abart *et al.*, 2004; Götze *et al.*, 2010; Keller *et al.*, 2010; Jeřábek *et al.*, 2014). Moreover, in experiment, inert markers may be used for tracing the Kirkendall plane (Fig. 10c). Thereby an inert metal (*e.g.* platinum) is deposited on the surface of one of the reactant crystals and, provided the metal particles are not dragged along by moving grain or phase boundaries, they trace the original interface between the two reactants after the experiment (Gardés *et al.*, 2011; Joachim *et al.*, 2011, 2012).

If the compositions and molar volumes of the phases involved in layer growth are constant, the position of the Kirkendall plane is controlled only by the relative component fluxes, which are, in turn, determined by the respective component mobilities. In an inverse approach, the relative component mobilities can be determined directly from the position of the Kirkendall plane (Abart *et al.*, 2004, 2009; Svoboda *et al.*, 2006b). For example, consider an assembly comprising a crystal of periclase (MgO) to the left and a crystal of corundum (Al₂O₃) to the right, which are in contact at a vertical interface (Fig. 11). Let periclase and corundum react to form a continuous layer of spinel (MgAl₂O₄) along their interface according to the reaction



Layer growth requires that either one or both of the components MgO and Al₂O₃ are transferred across the growing layer (Fig. 11). In general, the spinel layer grows from the original periclase–corundum interface into both directions replacing periclase at the periclase–spinel reaction interface (interface I in Fig. 11) and replacing corundum at the corundum–periclase reaction interface (interface II in Fig. 11).

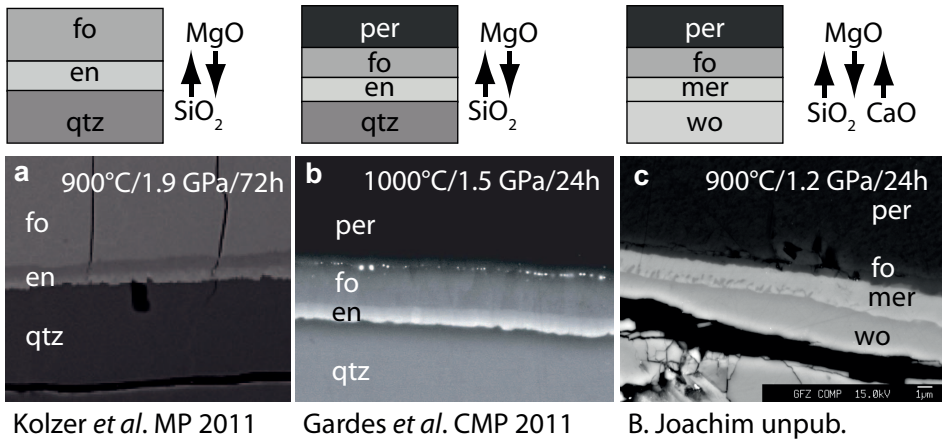


Figure 10. (a) Enstatite (en) layer forming at a forsterite (fo)–quartz (qtz) contact, different grey shades in the enstatite reflect differences in Fe content, the composition jump within the enstatite layer traces the original quartz–forsterite interface; (b) forsterite (fo)–enstatite (en) double layer forming at a periclase (per)–quartz (qtz) contact, bright spots at the periclase–forsterite interface are Pt-markers tracing the original periclase–quartz contact; image courtesy of E. Gardés; (c) forsterite (fo)–merwinite (mer) double layer at a periclase (per)–wollastonite (wo) contact; image courtesy of B. Joachim.

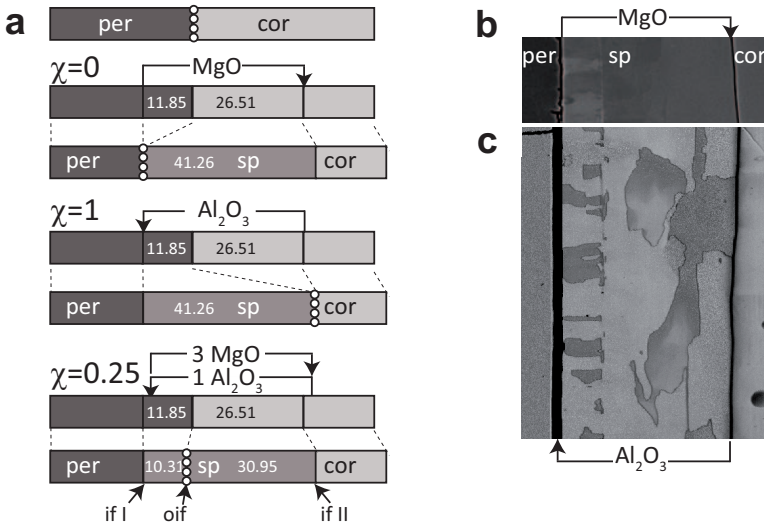
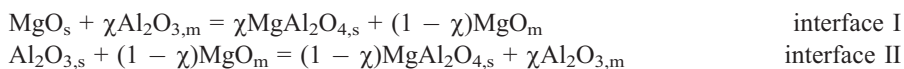


Figure 11. (a) Schematic drawing of layer growth in the system MgO–Al₂O₃; top – starting configuration with a crystal of periclase (per) and corundum (cor) in contact at a vertical interface; white circles indicate inert markers for tracing the original per–cor interface (oif). The panels below show layer growth of spinel (sp) with only MgO mobile ($\chi = 0$), only Al₂O₃ mobile ($\chi = 1$), and with transfer of both MgO and Al₂O₃ in proportions 3:1 ($\chi = 0.25$). The numbers indicate the volumes in cm³ of phases consumed/produced per mole of mobile components transferred; (b) BSE image and (c) forward scattered electron (FSE) image of spinel rim grown at 1350°C – note the change in microstructure of spinel at the original periclase–corundum interface.

The bulk reaction may be split into two half reactions occurring at the two reaction interfaces



where subscripts 's' and 'm' denote 'solid phase' and 'mobile component', respectively. Given that chemical components are neither added nor removed from the system, the two half reactions sum up to the bulk reaction. This implies that $(1 - \chi)$ moles of MgO are liberated at interface I and are transferred to interface II to form spinel by reaction with corundum. At the same time, χ moles of Al_2O_3 are liberated at interface II and are transferred to interface I, where they react with periclase to produce spinel. It can be seen from the half-reactions that the relative rates of MgO and Al_2O_3 mass transfer determine at what proportions spinel grows in the direction of periclase and corundum.

The relative interface velocities as calculated from equations 26 based on the compositions and molar volumes given in Table 1 are shown as functions of χ in Fig. 12a. All interface velocities are normalized to w_{Cor} . The interface velocities u_{Per} and w_{Cor} relative to the reactant phases are independent of χ and reflect merely the volumetric proportions at which the two reactant phases are consumed. For example, irrespective of the mass-transfer scenario, one mole of periclase corresponding to 11.85 cm^3 and one mole of corundum corresponding to 26.51 cm^3 are consumed per mole or 40.26 cm^3 of newly formed spinel (Fig. 11a). In contrast, the interface velocities w_{Sp} and u_{Sp} depend on χ . For $\chi = 0$ indicating that only MgO moves, all growth occurs at the spinel–corundum interface. Any inert markers on the original periclase–corundum interface would be located at the spinel–periclase interface. This scenario implies a large positive transformation strain at the corundum–spinel interface and a negative transformation strain at the periclase–spinel interface. For example, 26.51 cm^3 of corundum are replaced by 41.26 cm^3 of spinel at interface II, and 11.85 cm^3 of corundum are consumed while no

Table 1. Molar volumes and compositions of phases involved in layer growth as shown in Fig. 12. n_{MgO} , $n_{\text{Al}_2\text{O}_3}$, and n_{SiO_2} give the numbers of moles of component per formula unit of phase.

Phase	n_{MgO}	$n_{\text{Al}_2\text{O}_3}$	n_{SiO_2}	Ω (cm^3/mol)
Corundum	0	1	0	26.51
Periclase	1	0	0	11.85
Spinel	1	1	0	41.26
Quartz	0	0	1	23.38
Forsterite	2	0	1	44.87
Enstatite	1	0	1	31.92

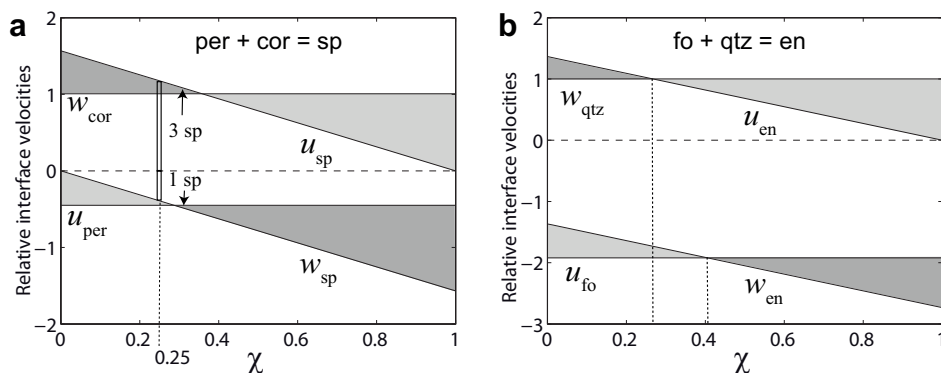


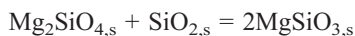
Figure 12. (a) Relative interface velocities for spinel (sp) layer growth at a periclase (per)–corundum (cor) contact in the system MgO–Al₂O₃; all velocities are normalized to w_{cor} , vertical bar drawn at $\chi = 0.25$ shows the relative rates at which spinel grows from the original interface into the directions of periclase and corundum; (b) relative interface velocities for enstatite (en) layer growth at a forsterite (fo)–quartz (qtz) contact in the system MgO–SiO₂; all velocities are normalized to w_{qtz} .

spinel is formed at interface I (Fig. 11a). In contrast, for $\chi = 1$, indicating that only Al₂O₃ is transferred between the two reaction interfaces, all growth occurs at the spinel–periclase interface, and any inert markers on the original periclase–corundum interface would be located at the spinel–corundum interface. This scenario implies a large positive transformation strain at the periclase–spinel interface and a negative transformation strain at the corundum–spinel interface. For example, 11.85 cm³ of periclase are replaced by 40.26 cm³ of spinel at interface I and 26.51 cm³ of corundum are consumed while no spinel is formed at interface II.

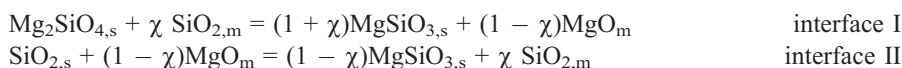
In the general case, where $0 < \chi < 1$, the trace of the original periclase–corundum interface is located within the spinel layer at a position depending on χ , and the transformation strain will be distributed more evenly over both reaction interfaces. The triangular areas shaded in dark grey in Fig. 12 indicate domains with positive transformation strain implying that the volume of spinel formed at the respective interface is larger than the volume of the reactant phase consumed. The triangular areas shaded in light grey indicate negative volume strain. The proportions of spinel growing into the direction of corundum and periclase can be read from intersecting a vertical line drawn from w_{sp} to u_{sp} with the horizontal line at zero velocity, such as indicated for $\chi = 0.25$.

In an inverse approach, the relative fluxes of the two components can be determined from tracing the position of the original periclase–corundum contact within the layer of newly formed spinel. In the case illustrated in Fig. 11b the position of the original periclase–corundum interface can be discerned from a discontinuity of the microstructure within the spinel layer at about 1/4 of the rim thickness on the side of periclase. This indicates $\chi \approx 0.25$ corresponding to the transfer of 1 mole of Al₂O₃ per 3 moles of MgO. This points to interdiffusion of $2\text{Al}^{3+}/3\text{Mg}^{2+}$ in an otherwise immobile oxygen sub-lattice (Götze *et al.*, 2010; Keller *et al.*, 2010; Jeřábek *et al.*, 2014).

The relations are somewhat different for enstatite-layer growth in the system MgO–SiO₂. When forsterite (Mg₂SiO₄) and quartz (SiO₂) are put into contact at sufficiently high temperature, they react to form enstatite (MgSiO₃) according to the reaction



Layer growth requires that either one or both of the components MgO and SiO₂ are transferred across the growing layer. The bulk reaction may be split into two half reactions occurring at the two reaction interfaces (Abart *et al.*, 2004)



Here $\chi = \frac{J_{\text{SiO}_2}}{J_{\text{MgO}} - J_{\text{SiO}_2}}$, and for $\chi = 0$, which indicates that only MgO and no SiO₂ moves, enstatite grows into both directions at the same rate, and the original forsterite–quartz interface is located in the centre of the enstatite layer (Fig. 12b). For $\chi = 1$, indicating that only SiO₂ and no MgO moves, all growth occurs at the forsterite–enstatite interface. The vertical dashed lines indicate constant volume replacement at the quartz–enstatite (left line at $\chi \approx 0.28$) and the forsterite–enstatite (right line at $\chi \approx 0.41$) interfaces. In this χ range the mechanical effects of growth are minimized, all other mass-transfer scenarios imply more severe transformation strains at the reaction interfaces. Milke *et al.* (2009b) presented experimental evidence for a feedback between mechanical effects and enstatite layer growth at forsterite–quartz contacts. They found different layer-growth rates when quartz grains were immersed in a forsterite matrix and when forsterite grains were immersed in a quartz matrix, which they ascribed to the different degree of mechanical-chemical feedback depending on the effective viscosity of the matrix phase (Schmid *et al.*, 2009).

The entire range of diffusive coupling, from largely independent component fluxes to charge-balanced interdiffusion has been documented for interlayer growth in silicate and oxide systems. For example, Gardés *et al.* (2011) demonstrated that during layer growth in the MgO–SiO₂ system under ‘dry’ conditions at 1.5 GPa and 1100°C to 1400°C only the MgO component, supposedly represented by cooperative movement of Mg²⁺ and O²⁻, was mobile, whereas the SiO₂ component remained in place. This is evident from the position of the Kirkendall plane at the periclase–forsterite contact during forsterite–enstatite double layer growth between periclase and quartz (see Pt markers in Fig. 10c). Similar findings were reported by Joachim *et al.* (2011) from layer growth in the system MgO–CaSiO₃, where MgO was the only mobile component under dry conditions. In contrast, charge-balanced interdiffusion of 2Al³⁺ and 3Mg²⁺ was identified as the mass-transfer scenario during the growth of magnesio-aluminate spinel (Carter, 1961; Rossi and Fulrath, 1963; Pfeiffer and Schmalzried, 1989; Götze *et al.*, 2010, 2014; Keller *et al.*, 2010) (Fig. 10b).

It must be noted that the direct link between component mobilities and the position of the Kirkendall plane is valid only for diffusion-controlled interlayer growth, where local equilibrium is maintained at the reaction interfaces. If, however, several dissipative processes such as sluggish interface reactions operate in parallel to long-range diffusion, the position of the Kirkendall plane is no longer diagnostic for the relative component mobilities (Svoboda *et al.*, 2010, 2011; Abart *et al.*, 2016).

2.2. Diffusion-controlled interlayer growth

2.2.1. Rate law for diffusion-controlled interlayer growth

Consider a binary system with components A and B and with phases α , β and γ (Fig. 13a). Let the g - X surfaces of α , β and γ be so sharp convex downwards that their equilibrium compositions are essentially fixed with $X_\alpha < X_\gamma < X_\beta$ (Fig. 13b). Let the assemblage $\alpha + \beta$ be metastable with respect to the assemblages $\alpha + \gamma$ and $\beta + \gamma$. At time $t = 0$, α and β are put into contact. After a short nucleation period, a layer of γ forms (Fig. 13a). Reaction is driven by the associated lowering of Gibbs energy as indicated by $\Delta_r G$ in Fig. 13b. Following Thompson (1959) we assume that, despite the bulk system being out of equilibrium, local equilibrium prevails at the α - γ and at the β - γ interfaces. At given pressure and temperature, local equilibrium between the two phases defines the chemical potentials of both components at the interface between the two phases. In a molar Gibbs energy diagram this is represented by the intersections of the common tangent to the g - X surfaces of the two phases with the ordinate axes at pure A ($\mu_A^{\alpha-\gamma}$, $\mu_A^{\gamma-\beta}$) and B ($\mu_B^{\alpha-\gamma}$, $\mu_B^{\gamma-\beta}$) compositions (Fig. 13b). The differences in the chemical potentials of the A and B components between the γ - β and the α - γ interfaces are related to $\Delta_r g$ by

$$\Delta\mu_A = \frac{\Delta_r g}{1 - X_\gamma} \quad \text{and} \quad \Delta\mu_B = \frac{-\Delta_r g}{X_\gamma} \quad (32)$$

In Fig. 13c the chemical potentials are shown, where a linear variation of the chemical potentials across the γ layer has been assumed. Given that component mobility is independent of position throughout the γ layer, this corresponds to constant flux. This, in turn, implies that γ grows only at the α - γ and the β - γ interfaces, and no sources or sinks for components A and B exist within the γ layer. The gradients in the chemical potentials and thus the driving force for diffusion of the A and B components across the layer of γ are obtained by dividing $\Delta\mu_A$ and $\Delta\mu_B$ by the layer width

$$\nabla\mu_A = \frac{\Delta_r g}{1 - X_\gamma} \frac{1}{\Delta R}, \quad \nabla\mu_B = \frac{\Delta_r g}{X_\gamma} \frac{1}{\Delta R} \quad (33)$$

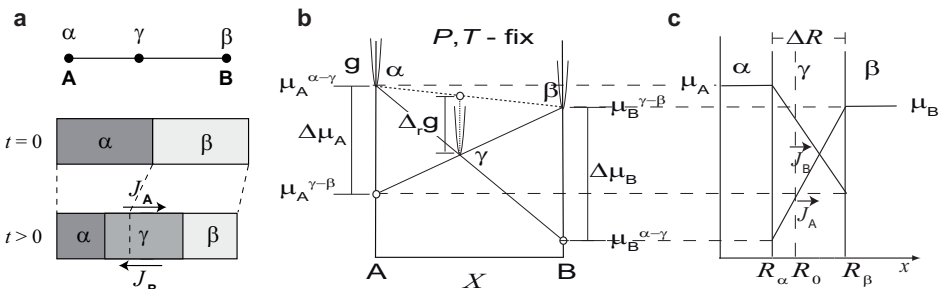


Figure 13. (a) Composition phase diagram and schematic drawing of a reaction-diffusion assembly of a binary system A–B with phases α , β and γ , where $\alpha + \beta$ react to form γ ; (b) schematic molar Gibbs-energy diagram; (c) variation of chemical potentials across the diffusion-reaction assembly; R is the spatial coordinate, and ΔR is the layer width; the vertical dashed line indicates the position of the Kirkendall plane.

According to equation 27 the rate of interlayer growth is proportional to the fluxes of the A and B components, J_A and J_B , respectively, so that

$$\frac{\partial \Delta R}{\partial t} = J_A u_A + J_B u_B \quad (34)$$

where u_A and u_B are taken from equation 28. The component fluxes are related to the gradients of the respective chemical potentials (Svoboda *et al.*, 2006a) (see also Petrishcheva and Abart 2017, this volume)

$$J_i = - \sum_j L_{ij} \nabla \mu_j, \quad \text{where } i, j = A, B \quad (35)$$

and L_{ij} are the phenomenological coefficients of diffusion. Combining kinematics with the flow law yields

$$\frac{\partial \Delta R}{\partial t} = \frac{\lambda}{\Delta R}, \text{ and rearrangement yields } \Delta R d\Delta R = \lambda dt \quad (36)$$

where

$$\lambda = \Delta_r g \frac{L_{AA} u_A X_\gamma + L_{AB} (u_A + u_B) (X_\gamma - 1) + L_{BB} u_B (X_\gamma - 1)}{X_\gamma (X_\gamma - 1)}$$

For a given set of kinetic parameters L_{ij} and for a given overall driving force $\Delta_r g$ the rate of layer growth decreases with layer thickness ΔR . For given layer thickness, the rate of layer growth is directly proportional to the overall driving force and increases with increasing values of the L_{ij} . Integration yields

$$(\Delta R)^2 = \lambda t \quad (37)$$

which is the parabolic growth law expected for diffusion-controlled interlayer growth in planar geometry. Parabolic growth has indeed been observed experimentally (see below), and it has been referred to as diffusion-controlled interlayer growth. Deviations from the parabolic rate law may occur when the effective component diffusivities change during layer growth or when other dissipative processes such as sluggish interface reaction or activity of non-ideal sources or sinks for vacancies are operative in parallel to long-range diffusion. Before we develop a model that accounts for several dissipative processes operating in parallel, we make a few general remarks.

2.2.2. Layer sequence

During diffusion-controlled interlayer growth in a binary system with phases of fixed composition, the number and the sequence of layers comprising the reaction band is determined exclusively by the equilibrium phase relations. If, for example, in the binary system A–B the two-phase assemblage $\alpha + \beta$ is metastable with respect to assemblages containing phase γ as shown in Fig. 13, only a single layer of γ is formed. If, however, the two-phase assemblage $\alpha + \beta$ is metastable with respect to assemblages containing either one or both of the phases γ and δ as shown in Fig. 14, two layers will

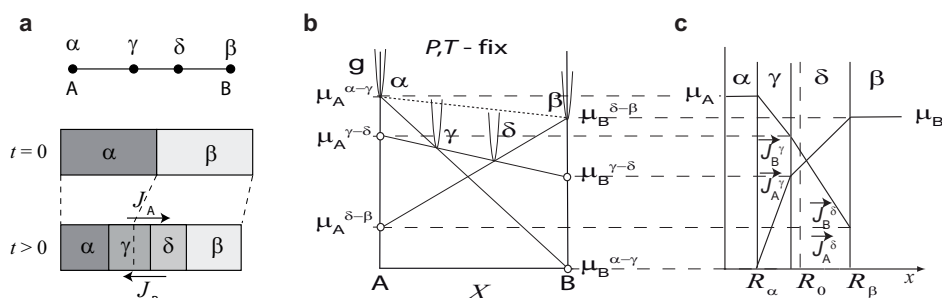


Figure 14. (a) Composition phase diagram and schematic drawing of a reaction-diffusion assembly of a binary system A–B with phases α , β and γ and δ , where $\alpha + \beta$ react to form γ and δ ; (b) schematic molar Gibbs-energy diagram; (c) variation of chemical potentials across the diffusion-reaction assembly; R is the spatial coordinate; the vertical dashed line indicates the position of the Kirkendall plane.

develop, and the layer sequence will be such that the γ layer is in contact with α and the δ layer is in contact with β . In the local-equilibrium scenario, the number of layers forming is determined by the number of stable phases with their compositions between the compositions of the reactant phases, and the sequence of mineral layers is such that the compositions of the layers vary in a monotonic manner across the reaction band.

The situation is fundamentally different during diffusion-controlled interlayer growth in ternary or higher-order systems. Using the ‘steady-diffusion model’ of Fischer (1973) it was demonstrated in a seminal work by Joesten (1977) that the sequence, phase content and width of the individual layers is determined by the relative fluxes of the mobile components. The steady-diffusion model is based on mass balance at layer boundaries, on the assumption of local equilibrium in the bulk and at layer contacts, and on diffusion driven by chemical potential gradients. Based on the Joesten approach, relative component mobilities were determined from reaction bands and corona structures (Joesten, 1977; Frantz and Mao, 1979; Foster, 1981; Grant, 1988; Joesten and Fisher, 1988; Abart *et al.*, 2001; Larikova and Zarsky, 2009).

2.2.3. Grain-boundary- vs. volume-diffusion

Experimentally observed layer-growth rates reflect the rates of bulk diffusive mass transfer across the growing layer or sequence of layers. They do not, however, give direct information on diffusion mechanisms and pathways. The diffusion coefficients extracted must thus be considered as ‘effective diffusion coefficients’, which integrate both, volume- and grain-boundary diffusion (Joesten, 1991). It was found generally in experiment that diffusion through polycrystalline layers is substantially faster than expected for diffusion in a single crystal of the same material. This suggests that grain-boundary diffusion may contribute significantly to bulk diffusion through a polycrystal (Fisler and Mackwell, 1994; Fisler *et al.*, 1997; Dohmen and Milke, 2010; Gardés and Heinrich, 2011).

Direct evidence for the significance of grain-boundary diffusion during interlayer growth was found in the system MgO–SiO₂, where the growth of enstatite layers between forsterite and quartz, forsterite-enstatite double layers between periclase and

quartz (Gardés *et al.*, 2011), and perovskite layers between periclase and quartz (Nishi *et al.*, 2013) do not follow a parabolic rate law. TEM observations revealed pronounced grain-coarsening as the reaction proceeded. Due to the coarsening, the number of grain boundaries available for grain-boundary diffusion decreased during the course of the reaction. From this Gardés *et al.* (2011) inferred that in their experiments most of the chemical mass transfer occurred by grain-boundary diffusion. Making use of this effect, grain-boundary diffusion coefficients for the diffusion of MgO in polycrystals of forsterite, enstatite (Gardés *et al.*, 2011), and of perovskite (Nishi *et al.*, 2013) were extracted. By contrast, growth of a layer of polycrystalline akermanite between monticellite and wollastonite strictly followed a parabolic rate law, although similar grain coarsening occurred indicating that grain-boundary diffusion only played a minor role and interlayer growth was essentially controlled by volume diffusion (Joachim *et al.*, 2011).

2.2.4. Influence of water

Mineral reactions may be enhanced substantially by the presence of even minute amounts of water (see Milke *et al.* 2017, this volume). On the other hand, nucleation and growth may be suppressed in ‘dry’ systems so that thermodynamic equilibrium is never attained (Harlov and Milke, 2002). The influence of minute amounts of water on reaction kinetics is difficult to quantify. Although infrared spectroscopy is a very sensitive method for the determination of water, results from infrared spectroscopy obtained from quenched samples probably do not reflect the availability of water at the *P-T* conditions of interest. The effect of trace amounts of water on the kinetics of interlayer growth was addressed in several studies in the systems MgO–SiO₂–H₂O and CaO–MgO–SiO₂–H₂O (Fisler *et al.*, 1997; Yund, 1997; Milke *et al.*, 2001, 2007, 2009, 2013; Gardés *et al.*, 2011, 2012; Joachim *et al.*, 2012; Milke *et al.* 2017, this volume). In the MS(H) system, growth of enstatite layers between forsterite and quartz in the presence of trace amounts of water is about four orders of magnitude faster than in a dry system. A systematic evaluation of this reaction using powder experiments with different water contents identified four different kinetic regimes (Gardés *et al.*, 2012; Milke *et al.* 2017, this volume). Intergranular transport of MgO is a function of the bulk water to solid ratio, and most of the ‘wet’ rim-growth experiments reported in the literature probably represent diffusion-controlled MgO transport under ‘hydrous-saturated grain boundary conditions’. The jump from the virtually dry regime to conditions at ‘hydrous-saturated grain boundaries’ is probably very narrow (Milke *et al.*, 2013). If only a few ppm of water are present, it may concentrate at the reaction interface (Abart *et al.*, 2004). Reactions occurring by diffusion along wetted grain boundaries or fluid-filled pores may produce specific microstructures (Milke *et al.*, 2009a). By combining 3D imaging and FTIR analysis, Milke *et al.* (2013) showed that a few tens of ppm of water may have a profound influence on the resulting microstructures. Formation of porosity at the reaction front – ‘active porosity’ – and within the newly formed layer – ‘passive porosity’ – is a characteristic feature. In line with Gardés *et al.* (2012) they still found transport-controlled kinetics in their experiments.

In addition, variable amounts of water may change the relative component mobilities. For enstatite-rim growth in water-saturated conditions it has been shown that the SiO_2 component becomes mobile in addition to MgO , but is still less mobile than MgO (Abart *et al.*, 2004; Gardés *et al.*, 2012). Joachim *et al.* (2012) investigated interlayer growth in the $\text{CaO-MgO-SiO}_2\text{-H}_2\text{O}$ system based on the overall reaction monticellite + wollastonite = diopside + merwinite. They observed systematic changes in microstructure evolution with changes in water content, which they ascribed to changes in the relative component mobility with changing water content (see Section 3 below). Finally, it was shown with TEM that water may be present as a separate phase at grain and phase boundaries even in overall water-deficient conditions (Grant *et al.*, 2014). These findings highlight the tremendous effect that minute amounts of water may have on mineral reactions. It is an indispensable pre-requisite for a sensible interpretation of reaction rims and corona structures from natural rocks that the amount of water present during reaction is known. New experimental and analytical methods are required to address this problem (see Milke *et al.* 2017, this volume).

2.3. Thermodynamic model for interlayer growth

2.3.1. The Thermodynamic Extremal Principle (TEP)

The evolution of a non-equilibrium material system is described by the rates at which its characteristic parameters such as the phase content, phase compositions or grain-size change, where these rates are functions of the characteristic parameters themselves. Constraints on the coupling among the different kinetic processes, by which system evolution occurs, can be obtained from extremal principles in the frame of the thermodynamics of irreversible processes. For example, Onsager (1931) derived the famous reciprocity relations based on maximizing the rate of entropy production associated with heat flow in an anisotropic medium. A more general variational approach, which is referred to as the ‘Thermodynamic Extremal Principle’ (TEP), was provided by Ziegler (1961). The TEP formulated in terms of the characteristic system parameters (Svoboda and Turek, 1991) proved to be a versatile tool for modelling irreversible processes in complex systems. The TEP is used in several studies described below, and a brief introduction is given here. For a detailed account of the approach the reader is referred to the chapter by Svoboda *et al.* (2017, this volume).

The rates of the characteristic system parameters are determined by thermodynamic fluxes j_i . We assume system evolution close to equilibrium, so that linear kinetics applies (De Groot and Mazur, 1984). The thermodynamic fluxes j_i are then related to the corresponding thermodynamic forces \mathcal{F}_k as (Callen, 1985)

$$j_i = \sum_k L_{ik} \mathcal{F}_k \quad (38)$$

where L_{ik} is a matrix of kinetic coefficients. The dissipation Q associated with the fluxes reads (Prigogine, 1967; Callen, 1985)

$$Q = \sum_i \mathcal{F}_i j_i \quad (39)$$

According to the TEP the independent thermodynamic fluxes attain the values that maximize the dissipation. In addition, in a closed system, the dissipation must be equal to the negative rate of the system Gibbs energy \dot{G} . The system evolution is thus governed by the constrained maximization

$$\text{Max } Q + \lambda (Q + \dot{G}) \quad (40)$$

where λ is a Lagrange multiplier. Noting that in the frame of linear kinetics, the dissipation function is quadratic in the fluxes (combined equations 38 and 39) this yields (Svoboda and Turek, 1991)

$$-\frac{1}{2} \sum_i \frac{\partial^2 Q}{\partial j_i \partial j_i} j_i = \frac{\partial \dot{G}}{\partial j_i} \quad (41)$$

The dissipation function and the rate of Gibbs energy are homogeneous functions of the fluxes of order 2 and 1, respectively, and $\frac{\partial^2 Q}{\partial j_i \partial j_i}$ as well as $\frac{\partial \dot{G}}{\partial j_i}$ are constants so that equation 41 represents a system of linear equations in the fluxes. Solving equations 41 for the fluxes provides a numerical scheme for describing system evolution in terms of the rates of the characteristic system parameters. The strategy is to integrate the fluxes over sufficiently small time steps and to update successively the system parameters. The TEP has been employed for describing system evolution in several non-equilibrium settings (see Svoboda *et al.*, 2017, this volume). The relation of the TEP to other extremal principles such as Prigogine's extremal principle were discussed in detail by Fischer *et al.* (2014).

2.3.2. Evolution equations for diffusion-controlled interlayer growth

Stoichiometry: We refer to the binary system A–B shown in Fig. 13a. The stoichiometric reaction equation reads

$$v_\alpha \mathbf{n}_\alpha + v_\beta \mathbf{n}_\beta = \mathbf{n}_\gamma \quad (42)$$

where

$$\mathbf{n}_j = \begin{pmatrix} n_A^j \\ n_B^j \end{pmatrix} = (n_A^j + n_B^j) \begin{pmatrix} 1 - X_j \\ X_j \end{pmatrix}, \quad j = \alpha, \beta, \gamma \quad (43)$$

is the composition vector of phase j , with n_A^j and n_B^j giving the numbers of moles of components A and B contained in one formula unit of phase j , and X_j is the mole fraction of component B in phase j ; v_α , v_β are the stoichiometric coefficients and v_γ has been set to unity.

Kinematics: The kinematics of layer growth is described by equations 29 and 31. In the following it is assumed that diffusion through the layer of γ occurs according to ideal thermodynamic behaviour, and equation 23 may be expressed as (Abart *et al.*, 2009)

$$\chi = \frac{D_A}{D_A + D_B} \quad (44)$$

where D_A and D_B are the 'effective self-diffusion coefficients' integrating both the contributions from diffusion through the grain interiors and along the grain boundaries.

Dissipation: We assume linear kinetics (De Groot and Mazur, 1984) so that equation 38 holds. Neglecting the off-diagonal terms of the coefficient matrix and inserting into equation 39 yields an expression for the local dissipation due to diffusion

$$q = \frac{J_i^2}{L_{ii}} \quad (45)$$

The total dissipation function is obtained from integrating over the entire γ layer

$$Q_{\text{diff}} = \int_{R_\alpha}^{R_\beta} \left(\frac{J_A^2}{L_{AA}} + \frac{J_B^2}{L_{BB}} \right) A dx \quad (46)$$

where A is cross-sectional area, which is henceforth set to unity. The fluxes J_A and J_B are expressed in terms of \dot{R}_α using equations 23 and 26 and are inserted into equation 46. Integration yields

$$Q_{\text{diff}} = \frac{1}{\tilde{D}} R_\alpha \dot{R}_\alpha^2 \left(\frac{R_\beta}{R_\alpha} - 1 \right) \quad (47)$$

where \tilde{D} is

$$\tilde{D} = -\frac{D}{R_g T} \frac{(\chi - 1)(1 - X_\gamma) - \chi X_\gamma}{[(1 - X_\alpha)X_\gamma - (1 - X_\gamma)X_\alpha]^2} \frac{\Omega_\alpha^2}{\Omega_\gamma} (1 - X_\gamma)X_\gamma \quad (48)$$

with R_g and T being the gas constant and absolute temperature, respectively; D is a combined effective diffusion coefficient accounting for diffusion of both, the A and B components. The effective tracer-diffusion coefficients of the A and B components are related to D as (see equation 44).

$$D_A = D\chi \text{ and } D_B = D(1 - \chi) \quad (49)$$

Gibbs energy: The rate of Gibbs energy change per unit area of the γ -layer is

$$\dot{G} = \Delta G_{\text{rim}} \dot{R}_\alpha \quad (50)$$

where

$$\Delta G_{\text{rim}} = -\frac{1}{\Omega_\alpha v_\alpha} \Delta_r G$$

and $\Delta_r G$ is the Gibbs energy of reaction (42) per mole of the product phase.

Evolution equation: Both the dissipation associated with diffusion of the A and B components as well as the free-energy change during reaction have now been expressed in terms of the single kinetic variable \dot{R}_α . For the case of only one internal variable the TEP (equation 40) degenerates to the constraint

$$Q = -\dot{G}$$

For the problem at hand this yields

$$R_\alpha \dot{R}_\alpha \left(1 - \frac{R_0 + u(R_\alpha - R_0)}{R_\alpha} \right) = \tilde{D} \Delta G_{\text{rim}} \quad (51)$$

where equation 31 has been used to eliminate R_β .

It is convenient to introduce a reaction progress variable

$$y = 1 - \frac{R_\alpha}{R_0}$$

which varies from 0 at $t = 0$ to 1, when α has been consumed. Noting that $dR_\alpha = -R_0 dy$, equation 51 is rewritten in terms of y as

$$R_0^2 [y(1 - u)] dy = \tilde{D} \Delta G_{\text{rim}} dt \quad (52)$$

Direct integration yields

$$\frac{R_0^2}{2} (1 - u) y^2 = \tilde{D} \Delta G_{\text{rim}} \quad (53)$$

Layer thickness is related to y as

$$\Delta R = R_0 (1 - u) y \quad (54)$$

and the evolution equation in terms of layer thickness reads

$$(\Delta R)^2 = \tau \quad (55)$$

where normalized time τ has been introduced with

$$\tau = 2(1 - u) \tilde{D} \Delta G_{\text{rim}} t \quad (56)$$

Equation 55 represents the parabolic rate law, which is expected for diffusion-controlled layer growth in planar geometry (compare equation 37). The parabolic rate law implies that diffusion-controlled interlayer growth is particularly efficient during early stages, and that the rate of layer growth decreases with increasing layer thickness, where diffusion becomes successively more inefficient. For a given layer width, the rate of layer growth depends on the thermodynamic driving force as given by ΔG_{rim} and on the combined diffusion coefficient \tilde{D} . Finally, it depends on the composition jumps at the reaction interfaces as expressed by the parameter u . In an inverse approach, effective component diffusivities can be obtained from experimentally observed layer growth rates. Combining equations 55 and 56 we obtain

$$(\Delta R)^2 = 2(1 - u) \tilde{D} \Delta G_{\text{rim}} t$$

which defines a straight line through the origin in a plot of $(\Delta R)^2$ vs. t with the slope $2(1 - u) \tilde{D} \Delta G_{\text{rim}}$. Given that for a specific reaction u and ΔG_{rim} are known, a linear fit to interlayer growth data plotted in this coordinate frame provides \tilde{D} . Noting that $\tilde{D} = \tilde{D}(D)$ (equation 48) the individual component diffusivities can be obtained by applying equation 49.

Following the approach outlined above, corresponding evolution equations were also derived for diffusion-controlled growth of a single layer in cylindrical and spherical geometry (Abart *et al.*, 2009). Evolution equations for diffusion-controlled multilayer growth in a binary system and planar geometry were presented by Svoboda *et al.* (2006b). Finally, a thermodynamic model for diffusion-controlled interlayer growth in multicomponent systems was developed by Svoboda *et al.* (2011).

Interlayer growth has indeed been demonstrated to follow a parabolic rate law in a number of experiments (Zaraysky *et al.*, 1989; Liu *et al.*, 1997). This has motivated a

series of interlayer-growth experiments in simple model systems aiming to determine effective diffusion coefficients from observed layer growth rates. The systems investigated so far include the binary systems MgO–SiO₂ (Brady and McCallister, 1983; Fislér *et al.*, 1997; Yund, 1997; Milke *et al.*, 2001; Gardés *et al.*, 2011), CaCO₃–SiO₂ (Milke and Heinrich, 2002), MgO–Al₂O₃ (Carter, 1961; Rossi and Fulrath, 1963; Watson and Price, 2001; Götze *et al.*, 2010; Keller *et al.*, 2010), and the ternary system MgO–CaO–SiO₂ (Joachim *et al.*, 2011, 2012). For a detailed account of the experimental details of interlayer growth see Milke *et al.* (2017, this volume).

Although the number of systems investigated so far is rather small, some general conclusions can be drawn at least for the system MgO–CaO–SiO₂ ternary system. It was generally observed that under dry conditions the SiO₂ and CaO components are rather immobile, whereas MgO can diffuse readily (Gardés *et al.*, 2011; Joachim *et al.*, 2011). The addition of even small amounts of water may have substantial impact on component mobility and the relative mobilities among MgO, CaO and SiO₂ may change. In particular, CaO and SiO₂ become successively more mobile with increasing water content (Milke *et al.*, 2001; Abart *et al.*, 2004, 2012; Gardés *et al.*, 2011, 2012; Joachim *et al.*, 2011).

2.3.3. Effect of sluggish interface reaction

In the above derivation, diffusion of the A and B components was considered as the only dissipative process. This implies that the reaction interfaces are perfectly mobile and local equilibrium prevails at the reaction interfaces. Perfectly mobile interfaces move without a local thermodynamic driving force, and the chemical potentials of the A and B components are continuous across the interfaces. This requires that the interface reactions proceed without any dissipation. In fact, interface reactions are dissipative processes, and, as a consequence, reaction interfaces have finite mobility (Balluffi *et al.*, 2005). To account for the potential effects of sluggish interface reaction, the dissipation associated with interface motion must be considered in addition to the dissipation due to diffusion (Dybkov, 1986; Gamsjäger, 2007; Abart and Petrishcheva, 2011). The above derivation for diffusion-controlled interlayer growth is still valid, but it needs to be extended to account for the sluggish motion of the reaction interfaces. This is done by adding a term which describes the dissipation associated with interface motion. In the following we briefly review the derivation of Abart and Petrishcheva (2011) to obtain the corresponding evolution equation.

Dissipation due to interface motion: For quantifying the dissipation associated with migration of the α – γ and the γ – β interfaces we imply that in the regime of linear kinetics interface velocity is related linearly to the driving force (Christian, 2002)

$$\dot{R}_\alpha = M_\alpha F_\alpha, \quad \dot{R}_\beta = M_\beta F_\beta \quad (57)$$

where M_α and M_β are the mobilities of the α – γ and the γ – β interfaces, respectively, and F_α and F_β are the corresponding driving forces. Combining equations 57 and 39 we obtain for the dissipation due to interface motion

$$Q_{\text{if}} = \frac{\dot{R}_\alpha^2}{M_\alpha} + \frac{\dot{R}_\beta^2}{M_\beta} \quad (58)$$

where Q_{if} refers to the motion of an interface segment of unit area. Using equations 29 and 31 to eliminate \dot{R}_β and taking dissipation due to diffusion from equation 47 the total dissipation per unit area of the γ -layer reads

$$Q_{tot} = \frac{1}{\tilde{D}} R_\alpha \dot{R}_\alpha^2 \left(\frac{R_\beta}{R_\alpha} - 1 \right) + \dot{R}_\alpha^2 \left(\frac{1}{M_\alpha} + \frac{u^2}{M_\beta} \right) \quad (59)$$

Evolution equation: \dot{R}_α is the only kinetic variable, and the TEP (equation 40) reduces to $Q = -\dot{G}$. For the problem at hand this yields

$$R_\alpha \dot{R}_\alpha \left(1 - \frac{R_0 + u(R_\alpha - R_0)}{R_\alpha} \right) - R_\alpha \left(\frac{\tilde{D}}{M_\alpha} + \frac{u^2 \tilde{D}}{M_\beta} \right) = \tilde{D} \Delta G_{rim} \quad (60)$$

where \dot{G} was taken from equation 50. In terms of the reaction progress variable y , equation 60 reads

$$[y(1 - u)R_0^2 + (a + u^2b)R_0]dy = \tilde{D} \Delta G_{rim} dt \quad (61)$$

where

$$a = \frac{\tilde{D}}{M_\alpha} \quad \text{and} \quad b = \frac{\tilde{D}}{M_\beta}$$

Integration of equation 61 yields

$$\frac{R_0^2}{2} (1 - u)y^2 + R_0(a + u^2b)y = \tilde{D} \Delta G_{rim} t \quad (62)$$

and inserting $\frac{\Delta R}{R_0(1-u)}$ for y we obtain

$$(\Delta R)^2 + \kappa \Delta R = \tau \quad (63)$$

where τ was taken from equation 56, and $\kappa = 2(a + u^2b)$.

Equation 63 describes mixed kinetics of layer growth with finite interface mobility. Model curves calculated from equation 63 for different values of κ are shown in Fig. 15. The parameter κ compares the efficiency of diffusion to the ease of interface motion. When interface mobilities are large compared to the diffusion coefficient, κ is small. In the case of purely diffusion-controlled layer growth $\kappa = 0$, and equation 63 reduces to the parabolic rate law of equation 55. The corresponding model curve is the straight line labelled $\kappa = 0$ in Fig. 15a. In contrast, when interface mobilities are small compared to the diffusion coefficient, κ is large, and the linear term on the left hand side dominates corresponding to a linear rate law. For a given value of κ the linear term dominates, when ΔR is small, *i.e.* during the initial stages of layer growth. With increasing layer thickness the quadratic term becomes more important, and layer growth becomes successively more parabolic. The transition from dominantly interface-reaction control to dominantly diffusion control is shown in Fig. 15b. During the initial growth stages the dissipation associated with interface motion dominates. With increasing layer thickness the dissipation associated with diffusion becomes dominant. The overall process becomes less efficient with increasing layer

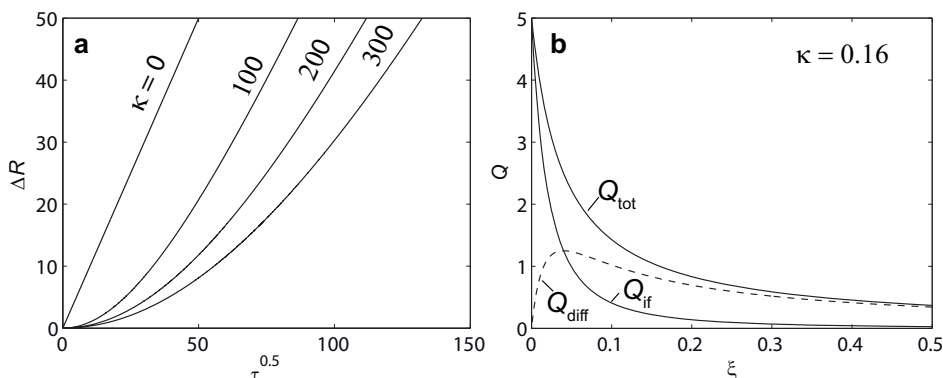


Figure 15. (a) Growth behaviour of a reaction layer in planar geometry, axes scales are in arbitrary units, κ describes the relative ease of long-range diffusion and interface reaction, $\kappa = 0$ and $\kappa = \infty$ correspond to pure diffusion-control and pure interface-reaction control, respectively – see text for further explanation; (b) contribution of diffusion (Q_{diff}) and interface motion (Q_{if}) to the total dissipation function (Q_{tot}) for a given value of κ and for reaction progress ξ ranging from 0 to 0.5.

thickness due to the increasing diffusion distance. As a consequence, the total dissipation decreases with reaction progress.

As may be expected from the above considerations, layer growth is found to follow a linear rate law only as long as the layers are thin with thicknesses on the order of several tens of nanometres (Cserhati *et al.*, 2008; Götze *et al.*, 2014). If layer thickness is of magnitude $1 \mu\text{m}$ or more, parabolic growth is generally observed. Only rarely was the transition from interface reaction-controlled to diffusion-controlled growth observed experimentally (Götze *et al.*, 2014). A gradual evolution from interface reaction-controlled to diffusion-controlled interlayer growth was suggested by Balashov and Lebedeva (1991).

2.3.4. Interlayer growth involving solution phases

When solution phases are involved in layer growth, new features including composition zoning and variations in the element partitioning at the reaction interfaces may appear. A schematic molar Gibbs energy diagram of a binary system with components A and B and three solution phases α , β and γ is shown in Fig. 16a. If the reaction interfaces are perfectly mobile, this implies local equilibrium at the reaction interfaces, and the compositions of the phases on either side of a reaction interface adhere to equilibrium element partitioning. If, however, the reaction interfaces have finite mobilities, equilibrium partitioning does not hold any more at a moving interface (Gamsjäger, 2007). Such a situation is illustrated schematically for the γ - β interface in Fig. 17. Given the γ - β interface has finite mobility, it only can propagate, when chemical potential jumps across the interface provide a local driving force for interface motion. For example, at the γ - β interface the chemical potential of component B is larger on the side of β than on the side of γ (Fig. 17). This provides a driving force for the transfer of component B from β to γ , which is required for the reaction interface to propagate

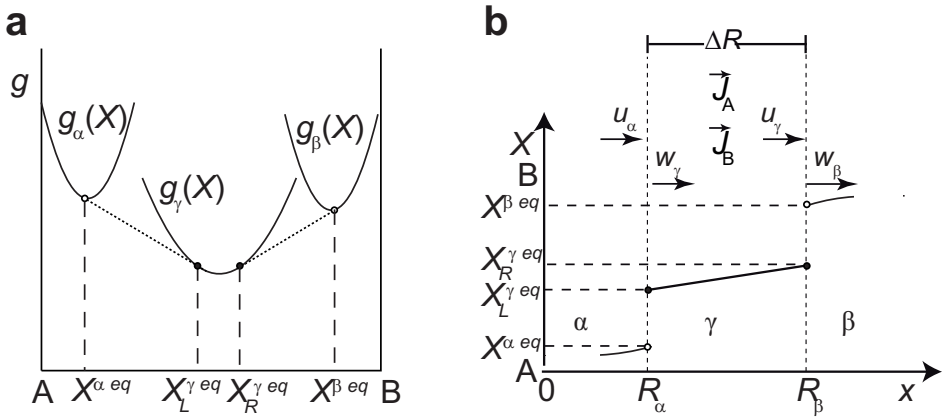


Figure 16. (a) Schematic molar Gibbs energy diagram of the binary system A–B with solution phases α , β and γ ; $X^{\alpha eq}$, $X^{\beta eq}$, $X_L^{\gamma eq}$ and $X_R^{\gamma eq}$ are the equilibrium compositions of α , β and of γ at the left and right reaction interfaces, respectively, as obtained from the common tangent construction; (b) composition variation across the γ layer and composition jumps at the α – γ and γ – β interfaces during diffusion-controlled growth (local equilibrium scenario), R_α and R_β are the positions of the α – γ and γ – β interfaces, u_α , u_γ , w_γ and w_β are the interface velocities, and J_A and J_B are component fluxes.

further into the reactant phase β . With similar reasoning an opposite jump in the chemical potential of component A can be argued for. The jump in the chemical potential of component B at the γ – β interface is labelled $\Delta\mu_B^{\gamma-\beta}$ in Fig. 17b. It can be seen from the tangent construction that this chemical potential jump implies that $X^\gamma < X^{\gamma eq}$ and $X^\beta > X^{\beta eq}$ at the γ – β interface. The extent to which the element

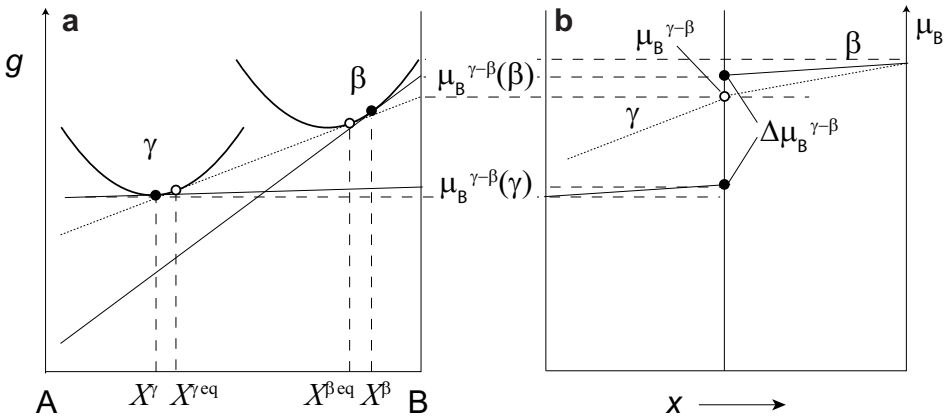


Figure 17. (a) Schematic molar Gibbs energy diagram showing the phase relations at a moving reaction interface in a binary system A–B, where solid-solution phase γ grows at the expense of solid-solution phase β ; local equilibrium scenario indicated by dotted tangent and open circle symbols for tangential points; finite interface mobility scenario indicated by solid tangents and filled circle symbols for tangential points; (b) corresponding chemical potential jumps at the reaction interface.

partitioning deviates from local equilibrium is determined by the coupling among the interface reactions at both the γ - α and the γ - β interfaces and long-range diffusion of the A and B components across the growing layer of γ . It is not clear, *a priori*, how these processes are coupled. Constraints on the coupling can be obtained from the TEP.

A thermodynamic model applying the TEP to layer growth with finite interface mobility and non-ideal sources and sinks for vacancies at the reaction interfaces was applied to analyse systematic deviations from equilibrium element partitioning observed during growth of magnesio-aluminate spinel at periclase-corundum interfaces (Abart *et al.*, 2016). The scenario where two phases of fixed composition react to form an intermediate solid-solution was considered. The corresponding molar Gibbs energy diagram is shown in Fig. 18a. From a set of kinematic equations relating the fluxes of the two components to interface motion and to the compositions of the intermediate solid-solution phase at the reaction interfaces, the system evolution expressed in terms of the kinetic variables was constrained to four degrees of freedom. The TEP (equations 40, 41) was then applied to solve for the kinetic variables. For a comprehensive presentation of the thermodynamic analysis the reader is referred to the original work by Abart *et al.* (2016). Here only a few salient features of the system evolution are summarized.

A systematic evolution of the compositions of the solution phase at the reaction interfaces starting with large deviations from equilibrium element partitioning during early growth and successive evolution towards local equilibrium with increasing layer thickness is predicted (Fig. 18b,c). The rate at which local equilibrium at the reaction interfaces is approached increases with increasing interface mobilities (Fig. 18c). The element partitioning at the moving reaction interfaces turned out to be a sensitive monitor for deviations from local equilibrium. In contrast, deviations from parabolic growth behaviour are comparatively subtle and can be detected only for substantial deviation from local equilibrium. Abart *et al.* (2016) showed that Mg-aluminate spinel

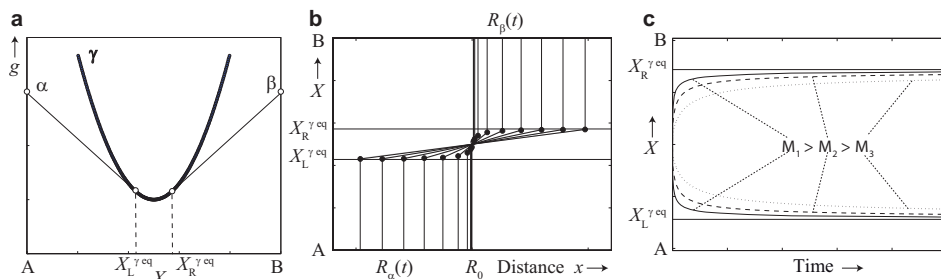


Figure 18. (a) Schematic molar Gibbs energy diagram for binary system A–B with phases α and β of fixed composition and intermediate solid-solution phase γ ; $X_L^{\gamma \text{eq}}$ and $X_R^{\gamma \text{eq}}$ are the equilibrium compositions of γ at the left and right interfaces; (b) evolution of compositions across the growing layer of γ , compositions of γ at the α - γ and γ - β interfaces are indicated as black dots, horizontal lines labelled $X_L^{\gamma \text{eq}}$ and $X_R^{\gamma \text{eq}}$ are the respective equilibrium compositions of γ ; (c) evolution of the compositions of γ at the reaction interfaces for three different interface mobilities, modified from Abart *et al.* (2016).

grown at a temperature of 1350°C and 1 bar started to grow with an $X_{\text{Al}_2\text{O}_3}$ about 0.03 off the equilibrium values at both reaction interfaces, and after 150 h the interface compositions of the spinel approached local equilibrium partitioning to within 0.01. Although this is a relatively small effect in the system investigated by Abart *et al.* (2016), this example testifies to the systematic departure from local equilibrium at a moving reaction interface in a high-temperature environment. Given that reaction interfaces always have finite mobility, it emerges that local equilibrium can generally not be attained at a moving reaction interface. Potentially this effect may have implications for a number of applications in geochemical and petrological modelling. It remains to be seen whether the effect is big enough to be detected in different systems and, if so, how far from local equilibrium the element partitioning can be at a propagating reaction front.

Irrespective of interface mobility other interesting effects may arise from the partitioning of minor and trace elements at a moving reaction interface. For example, Milke *et al.* (2011) investigated the growth of an enstatite layer at the contact between San Carlos olivine and quartz. Whereas San Carlos olivine has a Ni content of about 0.4 wt.%, the Ni content of the orthopyroxene growing at the expense of the olivine is substantially lower. As there is no other sink for Ni available, Ni is forced to diffuse back into the reactant olivine. This produces a zone of Ni enrichment in the olivine ahead of the propagating reaction interface. A similar phenomenon was documented from partial replacement of rutile by a corona of titanite during amphibolite-facies metamorphism of a metabasite by Lucassen *et al.* (2010). There, Nb, which is present in the rutile at ~300 ppm and has a lower concentration of 100 ppm in the titanite, was forced to diffuse back into the remaining rutile ahead of the rutile-titanite reaction front. The Nb content of relict rutile turned out to be a strong function of the degree of conversion to titanite. Small grains of relict rutile showed Nb contents as high as 1200 ppm. Reaction rim or corona formation may thus have a substantial impact on trace-element contents. This effect needs to be taken into consideration in any geochemical analysis of metasomatic reaction bands or coronas (Milke *et al.*, 2011).

To conclude this section we state that, in general, layer growth follows mixed kinetics which is governed by the coupling among long-range diffusion and the processes localized at the reaction interfaces and controlling interface motion. The most important features amenable to experimentation are layer-growth rate, position of the Kirkendall plane, phase compositions and the internal microstructure and texture. All features must be taken into consideration when analysing experimental layer growth or natural corona structures in mineral and rock systems. The Thermodynamic Extremal Principle (Ziegler, 1961; Svoboda and Turek, 1991; Svoboda *et al.*, 2005; Fischer *et al.*, 2014) is a powerful concept for describing mixed kinetics. Layer growth tends to be interface reaction-controlled during incipient stages and becomes successively more diffusion-controlled with increasing layer thickness. Diffusion-controlled layer growth follows a parabolic rate law, and element partitioning at reaction interfaces corresponds to equilibrium partitioning. In diffusion-controlled layer growth, relative component fluxes as obtained from the position of the Kirkendall

plane, reflect the relative, effective diffusion coefficients of the mobile components. Deviations from parabolic growth may arise from changes in the effective diffusion coefficient due to coarsening of a polycrystalline material or due to changes in the availability of water. So far the potential effects of finite interface mobility and of non-ideal sources and sinks for vacancies at reaction interfaces and in the bulk have been addressed mostly in theoretical work (Deal and Grove, 1965; Schmalzried, 1974; Farrell *et al.*, 1975; Gösele and Tu, 1982; Dybkov, 1986; Abart and Petrishcheva, 2011; Svoboda and Fischer, 2013). The effect of additional dissipative processes on layer growth rates, position of the Kirkendall plane and compositions of solution phases are well understood theoretically and quantitative models accounting for these effects have been presented. At present, the experimental evidence of systematic deviations from local equilibrium at reaction interfaces or from parabolic growth are scarce (Cserhati *et al.*, 2008; Götze *et al.*, 2014; Abart *et al.*, 2016). This does not mean, however, that these effects can be ignored generally. On the contrary, given that interface reactions are dissipative processes, systematic deviations from local equilibrium partitioning at a propagating reaction front are expected generally for diffusive phase transformations. It remains to be investigated how relevant this kinetic control may be for element partitioning in reactive mineral and rock systems.

3. Cellular segregation reactions – symplectite formation

Another important phenomenon related to a specific class of diffusive phase transformations in mineral and rock systems is the formation of symplectites (Spry, 1969; Vernon, 2004). A symplectite is a fine-grained intergrowth of two or more phases replacing a more coarse-grained reactant phase at a sharp reaction interface. An example is shown in Fig. 19. Typically, the phases constituting a symplectite have lamellar or vermicular shape and alternate at close to regular intervals. The long axes of the grains are usually oriented approximately perpendicular to the reaction interface. Based on this feature, which has been referred to as the “law of normality” by Obata

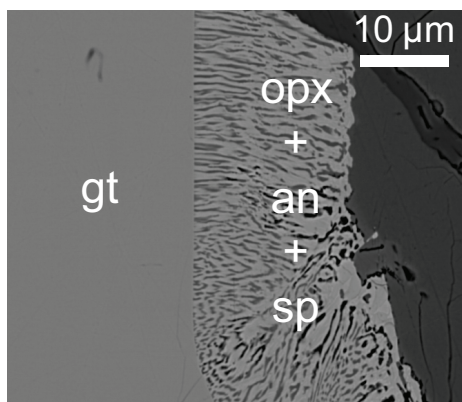


Figure 19. Example of an orthopyroxene (opx)–spinel (sp)–anorthite (an) symplectite replacing garnet from a lower crustal xenolith, Bacony volcanic field, Hungary; image courtesy of J. Degi.

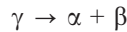
(2011), the trajectories, along which the reaction interface propagated into the precursor phase, can be reconstructed from the shape orientation of the symplectite phases. Symplectite formation may occur isochemically (Degi *et al.*, 2009; Obata *et al.*, 2013), or it may involve composition change on the scale of the symplectitic replacement structure (Mongkoltip and Ashworth, 1983; Nishiyama, 1983; Ashworth and Birdi, 1990; Johnson and Carlson, 1990). Typical examples are myrmekites, where K-feldspar is replaced by a quartz–plagioclase symplectite (Phillips, 1974; Abart *et al.*, 2014), pseudoleucites, where vermicular nepheline–K-feldspar intergrowths replace leucite (Gittins *et al.*, 1980), scapolite–quartz symplectites replacing K-feldspar (Harley and Santosh, 1995) and scapolite–clinopyroxene symplectites replacing garnet (Abart *et al.*, 2001). Symplectite formation may be induced by changes in pressure, temperature or fluid composition, which render the reactant phase metastable with respect to the symplectite assemblage. For example, kelyphites, which are plagioclase- and pyroxene- and/or amphibole-bearing symplectites, replace garnet during the decompression of high-pressure rocks (Messiga and Bettini, 1990; Obata, 2011; Obata and Ozawa, 2011; Obata *et al.*, 2013; Scott *et al.*, 2013). Similarly, omphacite is typically replaced by clinopyroxene–plagioclase symplectites during the decompression of eclogites (Boland and Van Roermund, 1983) or of eclogite-facies marbles (Proyer *et al.*, 2014). Symplectites have also been described from garnet peridotites, where chromian spinel-, orthopyroxene-, clinopyroxene- and olivine-bearing symplectites replace garnet during decompression (Morishita and Arai, 2003; Field, 2008; Spacek *et al.*, 2013). Formation of sapphirine–plagioclase, spinel–plagioclase or corundum plagioclase symplectites from kyanite are another phenomenon associated with decompression (Baldwin *et al.*, 2015). Symplectites may also form layers in a corona structure or in a metasomatic reaction band. In these cases their formation is driven by the supply or removal of mobile components in a chemical potential gradient (Mongkoltip and Ashworth, 1983; Nishiyama, 1983; Carlson and Johnson, 1991; Gallien *et al.*, 2013; Faryad *et al.*, 2015; Joachim *et al.*, 2012). Finally, symplectite formation may also be driven by oxidation such as the precipitation of rutile from hematite–ilmenite solid-solution (Tan *et al.*, 2015), or by dehydrogenation of H⁺-bearing olivine, which may lead to the segregation of chromian spinel- and clinopyroxene-bearing symplectite from the olivine host (Khisina *et al.*, 2013).

Despite their common occurrence, relatively few studies have addressed the kinetics of symplectite formation. In materials science the corresponding phenomenon is referred to as “cellular segregation reaction” (Cahn, 1959) and, due to its practical implications, has received considerable attention. The terminology was motivated by the close to regular alternation of the product phases, which very much resembles a ‘colony of cells’. Such microstructures are well known and were first investigated in steel making where the intimate lamellar intergrowth of ferrite (α -iron – bcc-structure) and cementite (iron carbide Fe₃C) is known as pearlite (Cahn and Hagel, 1962). Pearlite forms during the slow cooling of austenite (γ -iron – fcc-structure) with eutectic composition (Fe with 0.77 wt.% C) below the eutectic temperature of 727°C. Pearlite is one of the strongest materials known on Earth and is used in steel cables. More

generally, cellular segregation reactions are of great interest in materials sciences and several models have been suggested that describe the underlying kinetics.

According to Cahn (1959) two kinds of cellular segregation reactions are discerned (Fig. 20). When a solid-solution phase α_0 is supersaturated with respect to phase β , it may segregate phase β . If segregation occurs at a sharp reaction front and β precipitates as regularly spaced lamellae or rods, this is referred to as ‘cellular precipitation’ (Fig. 20a). In this reaction, one new phase β is formed, whereas phase α only changes its composition. Irrespective of the extent of chemical segregation, precipitation of β always leads to a lowering of the Gibbs energy. The second type of cellular segregation reaction is represented by the so called ‘eutectoidal reaction’ $\gamma \rightarrow \alpha + \beta$, where metastable phase γ is replaced by the assemblage $\alpha + \beta$ at a sharp reaction front (Fig. 20b). In this case, the reaction products α and β must have compositions that are shifted from the original composition of γ further than to composition $X^{\alpha'}$ or $X^{\beta'}$ in Fig. 20b to ensure lowering of Gibbs energy during transformation.

Consider a binary system A-B with phases α , β , γ such as shown in Fig. 21a. Let γ be metastable with respect to the assemblage $\alpha + \beta$ so that there is a driving force for the reaction



A simplified geometry of the corresponding symplectite reaction front is shown in Fig. 21b. Let the reaction front with thickness δ propagate into phase γ at a velocity u . Let the phases within the symplectite take the form of lamellae alternating at a constant interval λ .

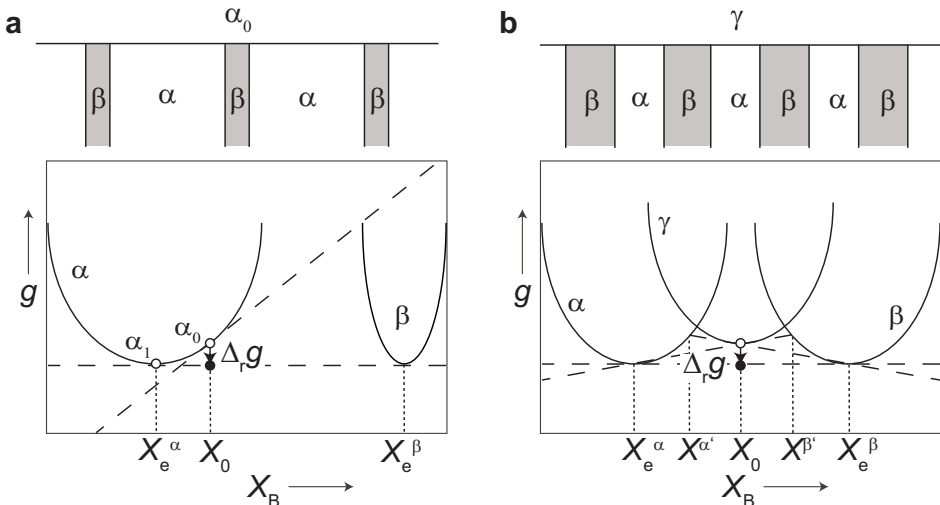


Figure 20. Schematic drawing of reaction microstructure and corresponding molar Gibbs energy diagrams for (a) cellular precipitation reaction $\alpha_0 \rightarrow \alpha_1 + \beta$; (b) eutectoidal $\gamma \rightarrow \alpha + \beta$; X_e^α and X_e^β are the equilibrium compositions of phases α and β in the product assemblage, $X^{\alpha'}$ and $X^{\beta'}$ indicate the minimum shift needed for the eutectoidal reaction to proceed, see text for further explanation.

Symplectite formation requires two processes to proceed in parallel. On the one hand, the material entering the reaction interface from the side of γ has uniform composition, whereas the material that comes out on the other side of the reaction front has segregated into two phases with different compositions. This implies that chemical components are re-distributed by diffusion within the reaction interface. On the other hand, propagation of the reaction interface into the γ phase requires that chemical bonds are broken and atomic rearrangements are made. The sum of these processes is referred to as interface reaction. Either chemical segregation by diffusion within the reaction front or interface reaction may be rate limiting. The coupling between the two processes determines the overall kinetics and microstructure evolution during cellular segregation. In the following we review briefly models of cellular segregation and discuss applications to symplectite formation. We start our considerations with reactions involving only phases of fixed composition and then turn to the more general case, where solid-solutions are involved.

3.1. Eutectoidal reaction involving phases of fixed composition

Let us begin with the system illustrated in Fig. 21a. Given that the g - X curves of all phases are sharply convex downward (Fig. 22a), the equilibrium compositions of the phases may be regarded as essentially fixed with $X_\alpha < X_\gamma < X_\beta$. The reaction thus has fixed stoichiometry given by

$$n_\gamma = v_\alpha n_\alpha + v_\beta n_\beta \quad (64)$$

where n_α , n_β and n_γ are composition vectors as defined in equation 43, and the stoichiometric coefficient v_γ was set to unity. The modal proportions m_α and m_β of α and β in the symplectite are given by

$$m_\alpha = \frac{v_\alpha \Omega_\alpha}{v_\alpha \Omega_\alpha + v_\beta \Omega_\beta} \quad \text{and} \quad m_\beta = 1 - m_\alpha \quad (65)$$

where Ω_α and Ω_β are the molar volumes of the α and the β phases. In general, a finite volume change is associated with transformation. Assuming that the

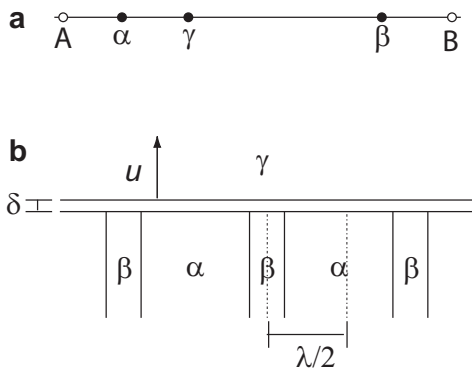


Figure 21. (a) Chemography of binary system A-B with phases α , β and γ ; (b) schematic drawing of a symplectite reaction interface.

transformation strain is negligible in the plane of the reaction interface, any volume change is accommodated by contraction/dilation in the direction perpendicular to the reaction interface. This implies that the reaction interface has different velocities relative to phase γ and to the $\alpha + \beta$ lamellar aggregate. The interface velocities are related through

$$v = u f_{\Omega}$$

where u and v are the interface velocities relative to material points in γ and in the $\alpha + \beta$ aggregate, respectively (Fig. 22), and the volume factor f_{Ω} is given by

$$f_{\Omega} = \frac{v_{\alpha}\Omega_{\alpha} + v_{\beta}\Omega_{\beta}}{\Omega_{\gamma}}$$

It is assumed that, irrespective of the volume factor, γ and the $\alpha + \beta$ aggregate stay in contact at the reaction front. If $f_{\Omega} \neq 1$, this implies that material points in γ and in the $\alpha + \beta$ aggregate move with respect to one another. Reaction is driven by the associated free energy change ΔG

$$\Delta G = \Delta_r \bar{g} + \frac{2}{\lambda} f_{\Omega} \sigma \tag{66}$$

where

$$\Delta_r \bar{g} = \frac{\Delta_r g}{\Omega_{\gamma}}$$

is the free energy change of reaction per unit volume of the reacting phase γ , and σ is the interfacial energy per unit area of an α - β interface.

3.1.1. Zener-Hillert model

An early model for cellular segregation was suggested by Zener (1958) and Hillert (1972). Here it was assumed that chemical segregation occurs by diffusion within the

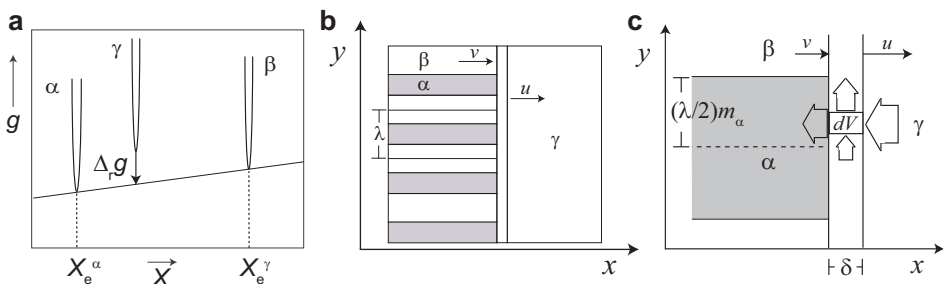


Figure 22. (a) Schematic molar Gibbs energy diagram for the binary system A–B with phases α , β and γ with sharp downwards convex g – X surfaces so that compositions are essentially fixed; (b) geometry of transforming system; (c) component fluxes into and out of the reaction interface associated with interface motion and diffusive flux along the reaction interface in the direction perpendicular to the lamellae in the α – β aggregate (y direction).

reactant phase ahead of the replacement front. Zener argued that diffusion becomes inefficient and hence overall reaction becomes slow towards large values of λ . On the other hand, the reaction rate becomes slow towards small values of λ , because the increasing volume density of interfaces and associated interfacial energy in the product assemblage successively diminishes the thermodynamic driving force (ΔG becomes less negative, see equation 66). The critical lamellar spacing λ_0 at which the driving force for reaction disappears was found from the condition

$$\Delta G = 0 = \frac{\Delta_r g}{\Omega_\gamma} + \frac{2}{\lambda_0} f_\Omega \sigma$$

Zener's model predicts the lamellar spacing λ_{\max} , which maximizes the reaction rate, to be $\lambda = 2\lambda_0$. Zener's model turned out to be a poor description of cellular segregation. Experimental evidence for chemical segregation by diffusion within the reactant phase ahead of the reaction front is missing, and the predictions regarding interlamellar spacing have not been verified experimentally.

3.1.2. Thermodynamic model for eutectoidal reactions

A thermodynamic model based on the dissipation principle (Onsager, 1931; Ziegler, 1961; Svoboda and Turek, 1991; Svoboda *et al.*, 2005; Fischer *et al.*, 2014) (see also section 2.3.1 of this chapter) was employed to describe symplectite formation in mineral systems by Ashworth and Chambers (2000), Degi *et al.* (2009), and Abart *et al.* (2012). Thereby it was assumed that chemical segregation occurs by diffusion within the reaction front. A schematic sketch of the transforming system is shown in Fig. 22.

Material re-distribution within the reaction front: Due to the fact that α and β have different compositions from γ , the material that enters the reaction front from the side of γ at a particular position has different composition from the material that leaves the reaction front on the side of the symplectite. We assume that growth has reached a steady state so that component concentrations within the reaction front remain constant with time. The composition difference between incoming and outgoing material must thus be compensated by corresponding diffusive fluxes within the reaction front in the direction perpendicular to the lamellae of the α - β aggregate (y direction in Fig. 22b,c). The local mass balance for component i in a small-volume element of the reaction front reads

$$\delta \frac{dJ_i}{dy} = uS_i^\alpha \text{ for } 0 \leq y \leq \frac{\lambda}{2} m_\alpha \quad (67)$$

$$\delta \frac{dJ_i}{dy} = uS_i^\beta \text{ for } \frac{\lambda}{2} m_\alpha \leq y \leq \frac{\lambda}{2} \quad (68)$$

where J_i is the diffusive flux of component i in y direction within the reaction front, and S_i^α and S_i^β may be regarded as source/sink terms for component i with

$$S_i^\alpha = \frac{n_i^\gamma}{\Omega_\gamma} - f_\Omega \frac{n_i^\alpha}{\Omega_\alpha}, \quad S_i^\beta = \frac{n_i^\gamma}{\Omega_\gamma} - f_\Omega \frac{n_i^\beta}{\Omega_\beta}$$

Integration over the lamella width yields

$$J_i(y) = \frac{u}{\delta} S_i^\alpha y \text{ for } 0 \leq y \leq \frac{\lambda}{2} m_\alpha \quad (69)$$

$$J_i(y) = \frac{u}{\delta} S_i^\beta y \text{ for } \frac{\lambda}{2} m_\alpha \leq y \leq \frac{\lambda}{2} \quad (70)$$

Dissipation: Adopting the expression for the local dissipation due to diffusion from equation 45 the dissipation function for diffusion reads

$$Q_{\text{diff}} = \iiint \sum_i \frac{J_i^2}{L_{ii}} dV \quad (71)$$

Inserting for J_i from equations 69 and 70 and considering $2/\lambda$ lamellae per square metre of interface yields

$$Q_{\text{diff}} = \frac{u^2 \lambda^2}{12\delta} \sum_i \frac{1}{L_{ii}} \left[(S_i^\alpha)^2 m_\alpha^3 + (S_i^\beta)^2 (1 - m_\alpha)^3 \right] \quad (72)$$

The diffusion within the reaction front causes a resistance against interface motion. It will be convenient to express dissipation due to diffusion within the reaction interface as

$$Q_{\text{diff}} = u^2 \frac{\lambda^2}{\delta} \frac{1}{M_{\text{diff}}} \quad (73)$$

where

$$M_{\text{diff}} = \frac{12}{m_\alpha^3 \sum_i \frac{(S_i^\alpha)^2}{L_{ii}} + (1 - m_\alpha)^3 \sum_i \frac{(S_i^\beta)^2}{L_{ii}}}$$

and

$$\frac{\lambda^2}{\delta} \frac{1}{M_{\text{diff}}}$$

may be interpreted as an interface mobility related to the necessary material redistribution by diffusion within the reaction front (Abart *et al.*, 2012). Note that this mobility depends on λ and δ .

The dissipation due to the motion of an interface with finite intrinsic interface mobility M_{if} and with velocity u reads (see equation 58)

$$Q_{\text{if}} = \frac{u^2}{M_{\text{if}}} \quad (74)$$

The total dissipation is then

$$Q_{\text{tot}} = Q_{\text{if}} + Q_{\text{diff}} \quad (75)$$

Gibbs energy: The rate of Gibbs energy change associated with transformation referring to a unit cross section of the reaction interface is given by

$$\dot{G} = u \left(\Delta_r \bar{g} + \frac{2}{\lambda} f_{\Omega} \sigma \right) \quad (76)$$

Evolution equation: The evolution of the system has been described in terms of a single kinetic parameter u , and the Thermodynamic Extremal principle (equation 40) reduces to the constraint $Q_{\text{tot}} = -\dot{G}$, which yields

$$u = M_{\text{tot}} \Delta G \quad (77)$$

where

$$M_{\text{tot}} = 1 / \left(\frac{\lambda^2}{\delta} \frac{1}{M_{\text{diff}}} + \frac{1}{M_{\text{if}}} \right)$$

may be regarded as the bulk interface mobility, which integrates the contributions from both diffusion within the reaction front and from interface reaction. Note that equation 77 corresponds to a linear rate law indicating that for a given thermodynamic driving force and a given set of kinetic parameters and lamellar spacing, the thickness of a cellular replacement microstructure increases linearly with time. As expected, the velocity of the reaction interface increases with increasing driving force and with increasing bulk interface mobility. Due to the different dependencies of thermodynamic driving force and interface mobility on λ , σ and δ , the velocity of the reaction front shows a complex behaviour as a function of these parameters, which can be seen more clearly, when equation 77 is expanded in the form

$$u = \frac{-\Delta_r \bar{g} - \frac{2}{\lambda} f_{\Omega} \sigma}{\frac{\lambda^2}{\delta} \frac{1}{M_{\text{diff}}} + \frac{1}{M_{\text{if}}}} \quad (78)$$

At small values of λ the reaction front velocity decreases with decreasing λ due to the reduction of the driving force that is associated with new interfaces. At large values of λ reaction-front velocity decreases with increasing λ due to the fact that diffusion becomes successively more inefficient with increasing diffusion length. For a given set of kinetic parameters (M_{if} and M_{diff}) and interfacial energy (σ) interface velocity is maximized at a specific lamellar spacing λ_{max} (Fig. 23a). It is supposed that λ_{max} is automatically selected by the system as it maximizes the rate of free-energy dissipation. At a given degree of reaction overstepping ($\Delta_r \bar{g}$) and a fixed value

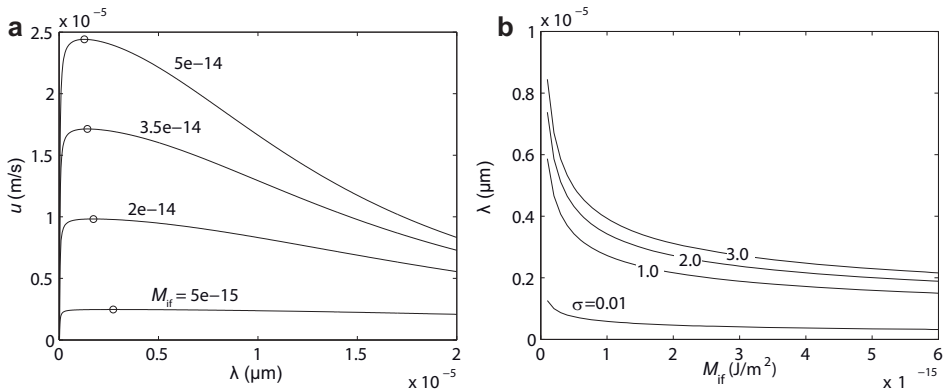


Figure 23. (a) Reaction front velocity u as a function of characteristic spacing λ for different values of M_{if} , small circles indicate u_{max} ; (b) λ_{max} as a function of M_{if} for different values of σ .

of M_{diff} , λ_{max} depends on the intrinsic interface mobility M_{if} and on interface energy σ (Fig. 23b). It increases with increasing σ and with decreasing M_{if} . If intrinsic interface mobility M_{if} is high, all the driving force is available for chemical segregation by diffusion within the reaction interface, which is then rate limiting. In the diffusion-controlled regime the evolving microstructure minimizes diffusion length, and λ_{max} is relatively small. If, however, the intrinsic interface mobility M_{if} is low, and the interface reaction is rate limiting, diffusion can be effective over larger distances, and the resulting λ_{max} is relatively large, ensuring minimum possible formation of new interfaces in the symplectite. The characteristic lamellar spacing of a symplectite is thus controlled by the relative contributions of interface reaction and diffusion within the reaction front to the overall resistance to interface motion.

Apart from qualitative inferences that can be made from an analysis of equation 78, it also provides the basis for quantifying the kinetic parameters from experiment. Remmert *et al.* (2017) grew synthetic symplectites in the CaO–MgO–SiO₂ system. To this end, monticellite with a composition of Ca_{0.88}Mg_{1.12}SiO₄ was treated at a pressure of 1.2 GPa and temperatures ranging from 1000°C to 1200°C and with addition of small amounts of water (0 to 0.5 wt.% of the total charge). The conditions chosen were outside the monticellite stability field, and the reactant monticellite (mtc I) decomposed forming two different types of symplectites (Fig. 24). One type is represented by a cellular aggregate of monticellite II + forsterite (sy I in Fig. 24a). Monticellite II has pure end-member composition (CaMgSiO₄) and is thus somewhat enriched in Ca relative to the original monticellite (Fig. 24b). The underlying reaction may be regarded as ‘cellular precipitation’. The second symplectite type is represented by a lamellar aggregate of merwinite and forsterite (sy II in Fig. 24a), corresponding to a ‘eutectoidal decomposition’. The product merwinite and forsterite appear to be chemically homogeneous and the forsterite-monticellite as well as the merwinite-monticellite sections of the reaction interface are curved with convex shape towards the

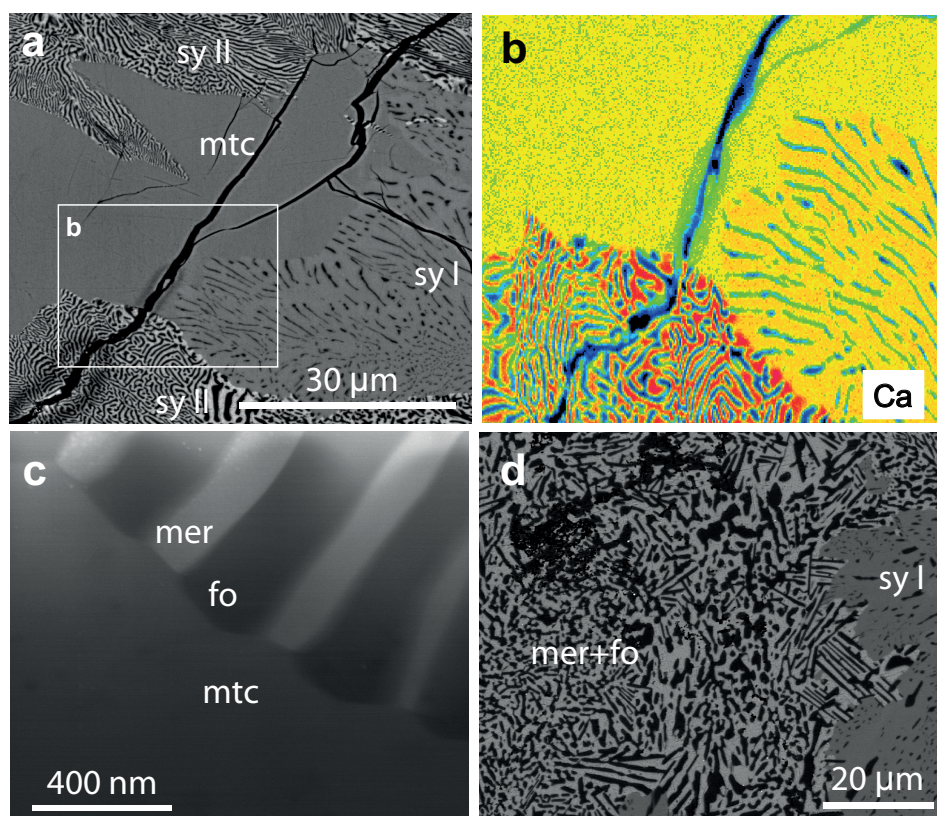


Figure 24. (a) BSE image of sy I (mtc II + fo) and sy II (mer+fo) forming from mtc I ($\text{Ca}_{0.88}\text{Mg}_{1.12}\text{SiO}_4$) at 1.2 GPa, 1000°C; insert indicates location of Ca-distribution map shown in b; (b) Ca-distribution map (red – high Ca-concentration, blue – low Ca-concentration), matrix mtc II in sy I is slightly enriched in Ca relative to mtc I; high Ca-matrix in sy II is merwinite; (c) STEM dark field image of sy II reaction front; note the convex shapes of merwinite and forsterite lamellae towards mtc I; (d) mer+fo assemblage from experiment with addition of 0.5 wt.% water.

reactant monticellite (Fig. 24c) probably reflecting the relatively low mobility of the triple junctions, where all three phases are in contact. These highly organized microstructures were generated only when little water (≤ 0.2 wt.% of the total charge) was added. At higher water contents, the product phases formed a ‘garben’ microstructure rather than a symplectite (Fig. 24d).

Moreover, Remmert *et al.* (2017) found a substantial increase in lamellar spacing with temperature but comparatively little influence of reaction overstepping and water content. This behaviour is best explained by different activation energies of interface reaction and chemical segregation by diffusion within the reaction front. The observed increase in lamellar spacing with increasing temperature would imply that the activation energy of interface motion is lower than the activation energy of diffusion

within the reaction front. Relatively low activation energy for interface motion compared to diffusion was reported from layer-growth experiments in the MgO–Al₂O₃ system (Götze *et al.*, 2014).

To conclude this section we note that at a given set of conditions the velocity of the reaction interface where an homogeneous precursor phase is replaced by a symplectite remains constant as long as the lamellar spacing does not change. The characteristic lamellar spacing reflects the relative contributions of the interface reaction as expressed by the intrinsic interface mobility and of the necessary component diffusion within the reaction front to the resistance against interface movement. The lamellar spacing is minimized if the diffusion within the reaction front is rate limiting, and it is comparatively large if the interface reaction is rate limiting. Experimental evidence for an increase in the characteristic lamella spacing with increasing temperature suggests that the activation energy for interface reaction is lower than for diffusion within the reaction front. As a consequence, symplectite formation is expected to be interface reaction-controlled at high temperature and likely becomes successively more diffusion-controlled towards lower temperature. In several cases, the characteristic lamellar spacing in symplectite microstructures has been observed to decrease successively towards the reaction front (Boland and Van Roermund, 1983). Based on independent constraints from mineral compositions in a myrmekite, such a pattern was interpreted as being due to symplectite growth at successively lower temperatures (Abart *et al.*, 2014).

3.2. Cellular segregation during interlayer growth

Symplectites may form layers in metasomatic reaction bands or in corona structures (Carlson and Johnson, 1991; Abart *et al.*, 2001; Yuguchi and Nishiyama, 2008; Joachim *et al.*, 2012; Gallien *et al.*, 2013). In this case, long-range diffusion across the growing layer as well as chemical segregation by diffusion within the reaction interfaces must be accounted for. Note that the chemical segregation within reaction fronts causes resistance to interface motion and implies finite interface mobility irrespective of the intrinsic interface mobility. Interlayer growth involving symplectitic microstructures may thus be expected to follow similar mixed kinetics as interlayer growth involving reaction interfaces with finite intrinsic mobility (see above). In the following a thermodynamic model describing growth of a single layer with lamellar microstructure is briefly reviewed, and some implications are discussed.

Consider the ternary system A, B, C containing phases α , β , γ and ε (Fig. 25a). Let the conditions be such that the assemblage α – β (dashed tie line in Fig. 25a) is metastable with respect to the assemblage ε – γ (solid tie line in Fig. 25a) so that a thermodynamic driving force is available for the reaction



All phases have fixed compositions with composition vectors (see equation 43) \mathbf{n}_α , \mathbf{n}_β , \mathbf{n}_γ , \mathbf{n}_ε . The stoichiometric coefficients, v_j , of the phases in the corresponding reaction equation are obtained from

$$\sum_j v_j \mathbf{n}_j = 0, \quad j = \alpha, \beta, \gamma, \varepsilon \quad (80)$$

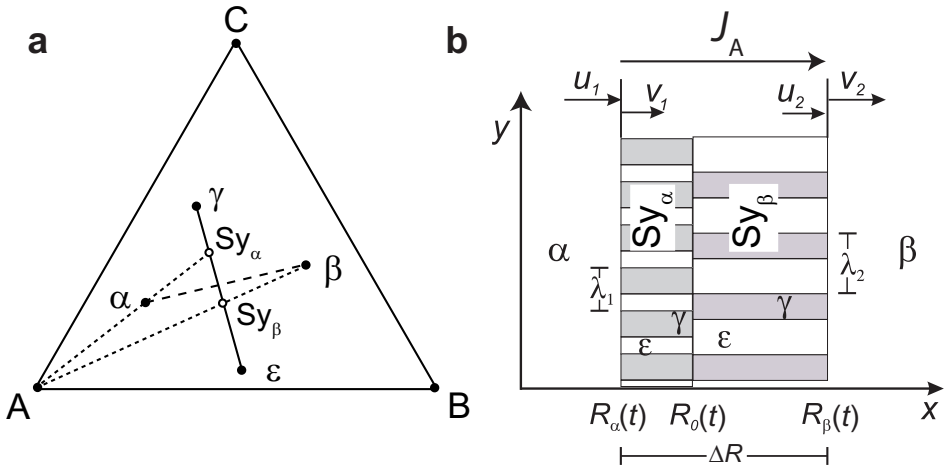


Figure 25. (a) Chemography of a ternary system A, B, C with phases α , β , ε , γ ; (b) schematic drawing of the system geometry; initially phases α and β have a common interface at R_0 extending in the y - z plane; at $t > 0$ a layer comprising two symplectite domains Sy_α and Sy_β forms; the symplectites comprise γ and ε lamellae with characteristic spacing λ_1 and λ_2 ; the reaction interfaces propagate with velocities u and v relative to the materials on either side; the positions of the fronts are at R_α and R_β , respectively.

Let the product phases ε and γ form a layer with symplectic (lamellar) microstructure along the initial α - β contact (Fig. 25b). The ε - γ two-phase layer grows from the original α - β interface at R_0 into both directions forming the domains Sy_α and Sy_β with interlamellar spacing λ_1 and λ_2 , respectively. Growth of the symplectic layer requires chemical mass transfer by diffusion over two different length scales. On the one hand, at least one component must be transferred across the growing layer. On the other hand, all three components must be re-distributed on the scale of the characteristic interlamellar spacing along the α - Sy_α and the β - Sy_β reaction interfaces. Let the component A be relatively more mobile than the components B and C. In this case, the component A is transferred across the growing layer and redistributed locally along β - Sy_β and the α - Sy_α reaction interfaces. In contrast, the less mobile components B and C are only redistributed along the reaction interfaces. For this scenario, the bulk reaction may be split into two half reactions, where we have

$$v_\alpha \mathbf{n}_\alpha + v_{\gamma 1} \mathbf{n}_\gamma + v_{\varepsilon 1} \mathbf{n}_\varepsilon + v_{A1} \mathbf{n}_A = 0 \quad (81)$$

at the α - Sy_α interface and

$$v_\beta \mathbf{n}_\beta + v_{\gamma 2} \mathbf{n}_\gamma + v_{\varepsilon 2} \mathbf{n}_\varepsilon + v_{A2} \mathbf{n}_A = 0 \quad (82)$$

at the β - Sy_β interface; $\mathbf{n}_A = (1, 0, 0)$ is the composition vector of the mobile component A. We assume overall closed-system behaviour so that $v_{A2} = -v_{A1}$. The dotted lines in Fig. 25a indicate compositions that are obtained from the reactant phases α and β , if only component A is added at the β - Sy_β reaction interface and removed from the α - Sy_α reaction interface. The intersections of the dotted lines with

the ε - γ tie line correspond to the compositions of the Sy_α and Sy_β domains. The corresponding modal proportions, m_α and m_β , of phase γ are given by

$$m_\alpha = \frac{v_{\gamma 1} \Omega_\gamma}{v_{\gamma 1} \Omega_\gamma + v_{\varepsilon 1} \Omega_\varepsilon} \quad \text{and} \quad m_\beta = \frac{v_{\gamma 2} \Omega_\gamma}{v_{\gamma 2} \Omega_\gamma + v_{\varepsilon 2} \Omega_\varepsilon} \quad (83)$$

for the domains Sy_α and Sy_β , respectively, where Ω_γ and Ω_ε are the molar volumes. The modal proportions of phase ε are $1 - m_\alpha$ and $1 - m_\beta$ in Sy_α and in Sy_β , respectively.

Combining the models of layer growth and cellular precipitation, Abart *et al.* (2012) obtained an explicit expression for the evolution of layer thickness ΔR

$$\frac{v_{A1}^2}{2L_{AA\perp}} (\Delta R)^2 + K \Delta R = v_\alpha (v_\gamma \Omega_\gamma + v_\varepsilon \Omega_\varepsilon) \Delta_{\text{rim}} G t \quad (84)$$

where $L_{AA\perp}$ is the mobility of component A in the ε - γ layer and

$$K = \left[\lambda_1^2 (v_{\varepsilon 1}^2 m_\alpha^3 + \frac{\Omega_\gamma^2}{\Omega_\varepsilon^2} v_{\gamma 1}^2 (1 - m_\alpha)^3) + \lambda_2^2 (v_{\varepsilon 2}^2 m_\beta^3 + \frac{\Omega_\gamma^2}{\Omega_\varepsilon^2} v_{\gamma 2}^2 (1 - m_\beta)^3) \right] \sum_i \frac{\Delta n_i^2}{12L_{ii}\delta}$$

where L_{ii} is the mobility of component i within the β - Sy_β and the α - Sy_α reaction interfaces ($i = A, B, C$), δ is the interface width, and

$$\Delta n_i = n_i^\gamma \frac{\Omega_\varepsilon}{\Omega_\gamma} - n_i^\varepsilon$$

Introducing

$$\bar{\kappa} = \frac{2KL_{AA\perp}}{v_{A1}^2} \quad \text{and} \quad \bar{\tau} = \frac{2L_{AA\perp} v_\alpha (v_\gamma \Omega_\gamma + v_\varepsilon \Omega_\varepsilon) \Delta_{\text{rim}} G}{v_{A1}^2} t$$

equation 84 may be written as

$$(\Delta R)^2 + \bar{\kappa} \Delta R = \bar{\tau} \quad (85)$$

which is similar to the rate law obtained for interlayer growth with finite intrinsic interface mobility (see equation 63). This indicates that similar mixed kinetic behaviour can be inferred for layer growth with symplectic internal microstructure and for layer growth involving interfaces with finite intrinsic mobility. As discussed for the latter case (see above), linear growth is expected, if interface motion is rate limiting. This is the case, when the resistance to interface motion due to chemical separation along the reaction interfaces dominates as compared to the resistance to long-range transfer of component A across the layer. Parabolic growth is expected, when long-range diffusion is rate limiting. Also, for a given set of kinetic parameters, *i.e.* for a given value of $\bar{\kappa}$, the linear term is dominant for small values of ΔR corresponding to early stages of layer growth, and the quadratic term becomes successively more important with increasing ΔR as layer growth proceeds.

It must be noted that apart from producing a single symplectic layer, reaction 79 may also produce a microstructure comprising two monomineralic layers. It can be shown, based on kinematic considerations, that the formation of a two-layer microstructure in a ternary system requires that at least two components are transferred across the layer, whereas only one component needs to be transferred across the layer if the symplectic microstructure is formed (Abart *et al.*, 2012). Hence, if a symplectic layer is formed in a ternary system, this indicates that one component is relatively more mobile than the other two. The proportions of the relatively less mobile components are then largely preserved across the β - Sy_{β} and the α - Sy_{α} reaction interfaces. For example, Mongkoltip and Ashworth (1983) found that the Al/Si proportions of the precursor phase were perfectly preserved in amphibole-spinel and amphibole-anorthite symplectite forming layers at olivine plagioclase contacts. It was argued by the latter authors that, for a two-phase symplectite to form in a general open system, at least two components must have restricted diffusion ranges. In contrast, when two components are relatively more mobile than the third one, a layered microstructure will form.

Interlayers of the lamellar and multilayer microstructural types were synthesized in the CaO–MgO–SiO₂ system by Joachim *et al.* (2012). Some run products are shown in Fig. 26. To this end, single-crystal monticellite (CaMgSiO₄) and wollastonite (CaSiO₃) were put into contact and reacted in a piston cylinder apparatus at 1.2 GPa and 900°C for 5 to 65 h to produce merwinite (Ca₃MgSi₂O₈) and diopside (CaMgSi₂O₆) according to the reaction



Thereby a merwinite–diopside reaction band was formed along the wollastonite–monticellite contact. For short run durations of 5 h, the reaction band took the form of a single merwinite–diopside layer with internal lamellar microstructure and with the Kirkendall plane in the centre of the layer (Fig. 26a). After 65 h a completely segregated reaction band with largely mono-phase layers showing the sequence merwinite–diopside–merwinite was formed (Fig. 26b).

The central position of the Kirkendall plane indicates that only MgO was transferred across the layer. In contrast, formation of the multilayer microstructure requires the

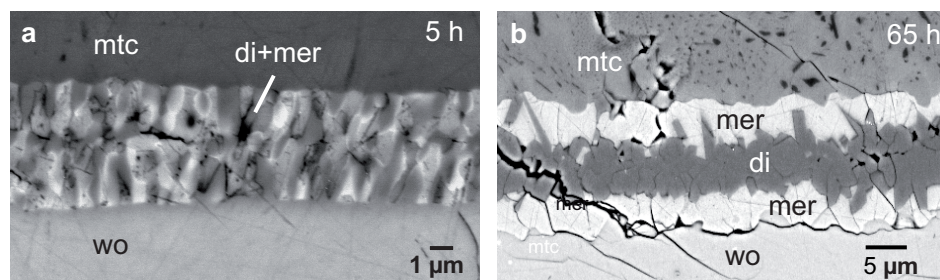


Figure 26. (a) Diopside–merwinite layer with lamellar internal microstructure, run duration 5 h; (b) merwinite–diopside–merwinite multilayer reaction band, run duration 65 h, modified from Joachim *et al.* (2012).

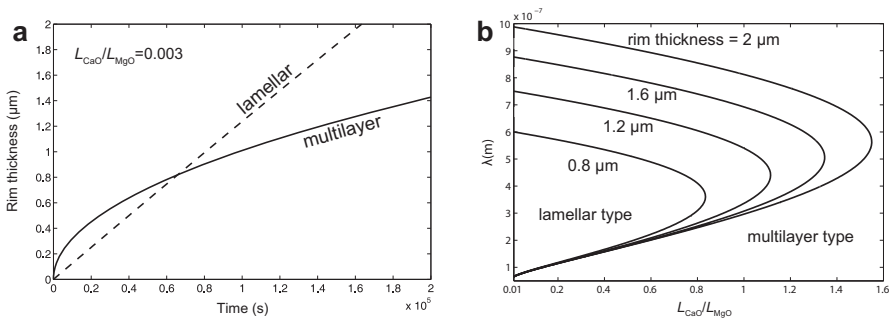


Figure 27. (a) Growth behaviour of multilayer and cellular types for a given ratio of phenomenological coefficients, where $L_{SiO_2} = L_{CaO}$ is implied; (b) parameter domains where the multilayer and the cellular microstructural types are preferred for layer thicknesses ranging from 0.8 to 2 μm , modified from Joachim *et al.* (2012).

additional transfer of either CaO or CaO and SiO₂. Considering the simplest case, where, in addition to MgO, only CaO is transferred across the layer, and based on the presumption that the microstructural type that maximizes the dissipation rate is selected by the system, parameter domains can be identified, where the different microstructural types are preferred (Abart *et al.*, 2012).

Total layer thickness is plotted vs. time in Fig. 27a for the lamellar and multilayer reaction bands and for a given L_{CaO}/L_{MgO} ratio. The material and geometrical parameters chosen are given in Table 2. The multilayer type shows parabolic growth behaviour, whereas the lamellar type shows linear growth during initial stages and parabolic growth is successively approached with increasing layer thickness. It is interesting to note that, for a given set of kinetic parameters, the growth rate is higher for the multilayer type than for the lamellar type during the initial growth stages. Towards later stages the situation reverses, and the growth rate is higher for the lamellar

Table 2. Material and system parameters used for model calculations shown in Fig. 27 (Abart *et al.*, 2012).

V_{mer}	10.06×10^{-5}	Molar volume of merwinite [m^3/Mol]
V_{di}	6.75×10^{-5}	Molar volume of diopside [m^3/Mol]
$\Delta_r G$	-1.22×10^4	Gibbs free energy of reaction [J/Mol]
δ	2×10^{-9}	Width of reaction front [m]
λ	2×10^{-6}	Characteristic spacing of cellular intergrowth [m]
σ	2	Interfacial energy [J/m^2]
L_{MgO}	5×10^{-14}	Phenomenological coefficient of diffusion of MgO [m^3/Mol]
s	1×10^{-1}	Grain boundary area fraction []

microstructural type. It is, hence, conceivable that a multilayer structure is formed during the initial stages and a symplectic microstructure is selected later. Incipient layer growth followed by symplectic intergrowth has indeed been reported from myrmekite (Abart *et al.*, 2014). Figure 27b shows the parameter domains for which the cellular and the multilayer microstructural types are preferred. The lamellar microstructure is preferred at a small $L_{\text{CaO}}/L_{\text{MgO}}$ ratio and in a limited domain of λ values. The minimum λ value is defined by the condition $\Delta_{\text{rim}}G = 0$. Towards large λ values the material redistribution within the reaction fronts becomes successively more difficult, and the multilayer microstructural type is preferred. The domain, where the lamellar microstructure is preferred, increases with increasing rim thickness. For a given rim thickness the maximum extension towards large $L_{\text{CaO}}/L_{\text{MgO}}$ values of the domain where the lamellar microstructure is preferred occurs at a specific λ_{max} , which maximizes the dissipation rate for a given set of kinetic parameters. λ_{max} increases slightly with increasing rim thickness suggesting that the characteristic wavelength of the lamellar microstructure tends to increase as the rim grows.

To conclude this section we remark that in systems with three or more components, interlayer growth may produce multilayer or symplectic microstructures. In a ternary system the multilayer microstructure is preferred when all three components have comparable diffusivities or two components have substantially higher diffusivities than the third one. A layer with symplectic microstructure is formed when one component has substantially higher diffusivity than the other two components. For a given overall reaction, chemical mass transfer across the layer is generally reduced if a symplectic microstructure is formed, as compared to the chemical mass transfer that is necessary for forming the multilayer type. For a given set of kinetic parameters, the multilayer type is preferred during the initial stages of interlayer growth, and the symplectic microstructure is preferred at later growth stages. A transition from the multilayer to the symplectic type is expected as interlayer growth proceeds. If the reverse transition, *i.e.* from symplectic to multilayer type is observed, this indicates that the diffusivity of one or both originally slow diffusing components was successively enhanced during the course of interlayer growth.

3.3. Cellular segregation involving solid solutions

When solid solutions are involved in a cellular segregation reaction, phase compositions become important. It was noted by Cahn (1959) that, if chemical segregation occurs only by diffusion within the reaction front of width δ , and the reaction front proceeds at velocity u , chemical segregation cannot go to completion. The product phases of a cellular segregation reaction in a binary system do not, in general, attain equilibrium compositions (X_c in Fig. 20) but have compositions that lie between X_c and X_0 , where X_0 represents the composition of the precursor phase. As a consequence, only a fraction ϕ of the maximum possible thermodynamic driving force $\Delta_r\bar{g}$ is available for driving interface motion. Equation 66 from above needs to be modified as

$$\Delta_r g = \phi \Delta_r \bar{g} + \frac{2}{\lambda} f_{\Omega} \sigma \quad (86)$$

Lowering the available driving force by a factor ϕ accounts for the dissipation due to diffusion within the reaction front. Cahn (1959) suggested models for cellular precipitation and for eutectoidal decomposition based on the following assumptions: (1) the reaction front is planar; (2) chemical segregation occurs by diffusion within the reaction front of thickness δ containing material with composition X_B , where X is a mole fraction; the binary inter-diffusion coefficient within the reaction front is D_B ; (3) X_B varies in the direction perpendicular to the lamellae of the cellular microstructure, $X_B = X_B(y)$; (4) the system has reached a steady state, so that neither the interlamellar spacing nor the composition $X_B(y)$ changes with time; (5) local equilibrium prevails at the interfaces between the product phases.

In his derivation Cahn (1959) expressed equations 67 and 68 from above in the form

$$\delta D_b \frac{\partial^2 X_B}{\partial^2 y} = u(X_\gamma - f_\Omega X_P) \quad (87)$$

where X_B is the composition of the material within the reaction front, and X_P is the composition of a newly formed phase in the cellular microstructure. It was further assumed that the compositions in the reaction front and the compositions of the precipitates are related through

$$X_P = kX_B$$

where k is a partition coefficient. Integration of equation 87 yields

$$X_P = X_0 + A \cosh \left(\frac{ku\lambda^2}{D_B\delta} \right)^{\frac{1}{2}} \frac{y}{\lambda} \quad (88)$$

where A is an integration constant. In the following, Cahn's derivation for cellular precipitation is summarized briefly. For an equivalent derivation of the model suitable for eutectoidal decomposition, the reader is referred to the original work by Cahn (1959).

Cellular precipitation: In the case of precipitation of β from only slightly supersaturated α_0 , the width of the β lamellae is small compared to the characteristic interlamellar spacing, and the integration constant is evaluated from the condition

$$X_P = X_e \text{ at } y = \lambda/2$$

where y is measured from the centre of the lamella of the depleted phase α . The composition of the depleted phase α as a function of position y is given by

$$\frac{X - X_0}{X_e - X_0} = \frac{\cosh \left(\frac{ku\lambda^2}{D_B\delta} \right)^{\frac{1}{2}} \frac{y}{\lambda}}{\cosh \left(\frac{ku\lambda^2}{D_B\delta} \right)^{\frac{1}{2}}} = \frac{\cosh \sqrt{\chi} \frac{y}{\lambda}}{\cosh \sqrt{\chi}} \quad (89)$$

where X_0 is the composition of the reactant phase α_0 , and X_e is the composition of α in equilibrium with β . The important parameter

$$\chi = \frac{ku\lambda^2}{D_B\delta}$$

compares the ease of front propagation as expressed by its velocity u and the resistance to motion due to diffusion within the reaction front. Thereby it is implied that $u = M_{if}\Delta_{rg}$, where Δ_{rg} is taken from equation 86, and M_{if} is the intrinsic mobility of the reaction interface. Small values of χ correspond to scenarios where the rate of reaction-front propagation is largely controlled by the interface reaction. In this case, diffusion is effective over the entire lamellar width, and the depleted phase α has close-to-equilibrium composition right across the lamella. If, in contrast, the intrinsic interface mobility is high, diffusion within the reaction front is rate limiting, and the composition of the depleted phase α varies with position. In this case, the depleted phase α attains equilibrium compositions only at the α - β interfaces, and the composition X_0 is approached in the central parts of the α lamellae.

The composition variation across a lamella of depleted phase α is shown for different values of χ in Fig. 28. For small values of χ , the equilibrium composition is approached closely everywhere in phase α , and close to 100% of the thermodynamic driving force Δ_{rg} is available for driving the interface reaction at the reaction front. For increasing values of χ , equilibrium compositions are successively more restricted to the α - β interfaces at $\pm\lambda/2$, whereas the composition of the reactant phase α_0 is successively approached in the central portions of the α lamella. The internal composition zoning of

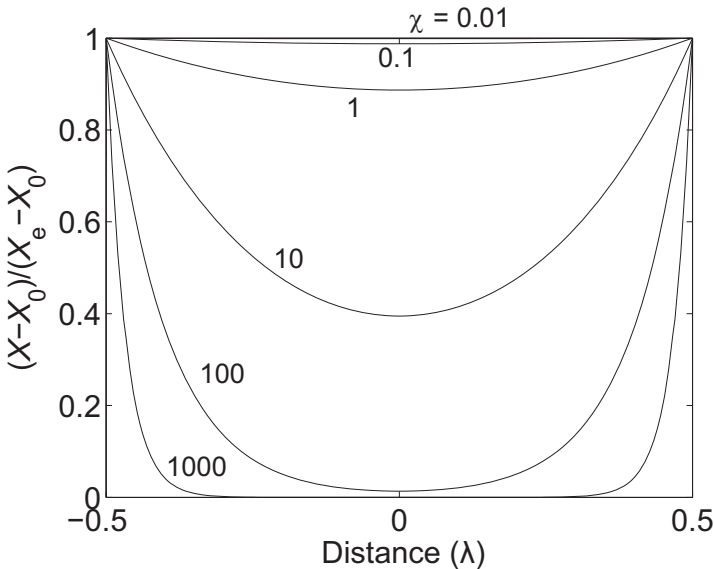


Figure 28. Composition variation across a lamella of depleted α phase for values of χ ranging from 0.01 to 1000 and expressed as fractional approach towards equilibrium composition, modified from Abart *et al.* (2014).

the lamella of depleted phase α thus bears information on the degree of departure from local equilibrium and on the fraction of the thermodynamic driving force that is locally availability at the reaction front.

Similar composition zoning as predicted from Cahn's model has been described from plagioclase feldspar forming the matrix of a myrmekite replacing perthitic alkali feldspar (Abart *et al.*, 2014). Several myrmekite generations were discerned by the latter authors with successively decreasing interlamellar spacing from the oldest portions of the myrmekite (furthest away from the reaction front) to the younger portions closer to the reaction front. The plagioclase exhibits uniform and relatively more anorthite-rich composition in the coarse-grained portions of the myrmekite, and it becomes more albite-rich, with successively greater compositional variability in the younger portions closer to the reaction front. More specifically, in the fine-grained portions of the myrmekite the plagioclase is more anorthite-rich at the interfaces with the quartz lamella than in the more central portions of the plagioclase domains, where the anorthite content approaches the one of the reactant alkali feldspar (Fig. 29). The successive decrease in characteristic grain size, the overall decrease of anorthite content, and the characteristic internal zoning of plagioclase in the latest myrmekite generation were interpreted by Abart *et al.* (2014) as an indication of myrmekite formation at decreasing temperature. The observed grain-size decrease and composition pattern indicates an increasing dominance of diffusion control over interface-reaction control with decreasing temperature. This, in turn, corroborates the view that the activation energy of the interface reaction controlling the intrinsic interface mobility is lower than the activation energy of diffusion within the reaction front.

We conclude this section by noting that symplectites are complex, but highly organized fine-grained, polyphase microstructures replacing a coarser-grained precursor minerals at a sharp reaction front. The characteristic grain size, shape, shape orientation and chemical zoning of the symplectite phases reflect the coupling between the interface reaction, by which the replacement front propagates, and diffusion within the propagating replacement front, which is necessary for the lateral chemical segregation inherent in symplectite formation. Thermodynamic models can

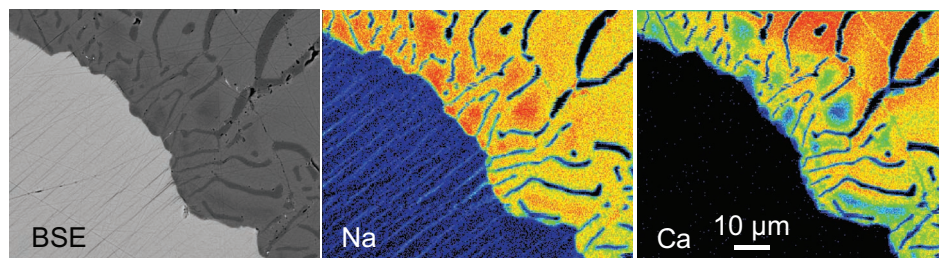


Figure 29. BSE image and Na- and Ca-element distribution maps of the youngest myrmekite generation in the Weinberg granite. Note the characteristic composition zoning with complementary Na and Ca distributions, modified from Abart *et al.* (2014).

be formulated that describe quantitatively this coupling and provide tools for extracting rate information from observed symplectite microstructures and composition patterns in an inverse approach. So far, experimental calibration of diffusion in a propagating reaction interface and of the kinetics of interface migration is largely non-existent for silicates and geologically relevant oxide systems, and the inferences drawn from this inverse approach are largely of qualitative nature. Dedicated experiments addressing these underlying processes are, however, feasible and will probably gain increasing importance so that, eventually, symplectites will be used for geo-speedometry purposes.

4. Concluding remarks

In this chapter we addressed three types of metamorphic mineral reactions: porphyroblast growth, the formation of coronas, reaction-rims or metasomatic reaction bands and symplectite formation. Typically, these reactions occur at different stages of metamorphism. Whereas porphyroblast growth is important during prograde metamorphism of rocks which have been affected previously only by diagenesis or low-grade metamorphism, corona and symplectite formation is typically associated with mineral reactions which occurred in rocks which were previously subjected to medium- or high-grade metamorphism or in magmatic rocks. All three reaction types may be classified as diffusive phase transformations, involving long-range chemical mass transport and interface reactions. It was shown that the coupling and the relative rates of chemical mass transfer and interface reactions determine the overall reaction kinetics as well as the resulting reaction microstructures and chemical patterns. During porphyroblast growth, rocks tend to be saturated with respect to a fluid phase, and chemical mass transport is fast. In contrast, corona and symplectite formation indicate sluggish chemical mass transfer. Thermodynamic models linking the underlying kinetic processes to system evolution and to reaction microstructures were discussed. The formalism presented here provides a sound basis for analysing reaction microstructures and composition patterns from experiment and from natural mineral and rock systems.

References

- Abart, R. and Petrishcheva, E. (2011) Thermodynamic model for reaction rim growth: Interface reaction and diffusion control. *American Journal of Science*, **311**, 517–527.
- Abart, R. and Sperb, R. (2001) Metasomatic coronas around hornblende xenoliths in granulite facies marble, Ivrea zone, N Italy. II: Oxygen isotope patterns. *Contributions to Mineralogy and Petrology*, **141**, 494–504.
- Abart, R., Schmid, R. and Harlov, D. (2001) Metasomatic coronas around hornblende xenoliths in granulite facies marble, Ivrea zone, N-Italy: constraints on component mobility. *Contributions to Mineralogy and Petrology*, **141**, 473–492.
- Abart, R., Kunze, K., Milke, R., Sperb, R. and Heinrich, W. (2004) Silicon and oxygen self-diffusion in enstatite polycrystals: the Milke et al. (2001) rim growth experiments revisited. *Contributions to Mineralogy and Petrology*, **147**, 633–646.
- Abart, R., Petrishcheva, E., Fischer, F. and Svoboda, J. (2009) Thermodynamic model for diffusion controlled reaction rim growth in a binary system: Application to the forsterite-enstatite-quartz system. *American Journal of Science*, **309**, 114–131.

- Abart, R., Petrishcheva, E. and Joachim, B. (2012) Thermodynamic model for growth of reaction rims with lamellar microstructure. *American Mineralogist*, **97**, 231–240.
- Abart, R., Heuser, D. and Habler, G. (2014) Mechanisms of myrmekite formation: case study from the Weinsberg granite, Moldanubian zone, Upper Austria. *Contributions to Mineralogy and Petrology*, **168**, 2–14.
- Abart, R., Svoboda, J., Jeřábek, P., Povoden-Karadeniz, E. and Habler, G. (2016) Kinetics of layer growth in a binary system with intermediate solid-solution and interfaces with finite mobility acting as non-ideal sources and sinks for vacancies: thermodynamic model and application to magnesio-aluminate spinel layer growth. *American Journal of Science*, **316**, 309–328.
- Ague, J.J. and Carlson, W.D. (2013) Metamorphism as garnet sees it: the kinetics of nucleation and growth, equilibration, and diffusional relaxation. *Elements*, **9**, 439–445.
- Anczkiewicz, R., Chakraborty, S., Dasgupta, S., Mukhopadhyay, D. and Koltonik, K. (2014) Timing, duration and inversion of prograde Barrovian metamorphism constrained by high resolution Lu-Hf garnet dating: A case study from the Sikkim Himalaya, NE India. *Earth and Planetary Science Letters*, **407**, 70–81.
- Ashworth, J. and Birdi, J. (1990) Diffusion modeling of coronas around olivine in an open system. *Geochimica et Cosmochimica Acta*, **54**, 2389–2401.
- Ashworth, J. and Chambers, A. (2000) Symplectic reaction in olivine and the controls of intergrowth spacing in symplectites. *Journal of Petrology*, **41**, 285–304.
- Baddeley, A. and Turner, R. (2000) Practical maximum pseudolikelihood for spatial point patterns. *Australian and New Zealand Journal of Statistics*, **42**, 283–322.
- Balashov, V. and Lebedeva, M. (1991) Macrokinetic model of origin and development of a monomineralic bimetasomatic zone. Pp. 167–195 in: *Progress in Metamorphic and Magmatic Petrology* (L.L. Perchuk, editor). Cambridge University Press, Cambridge, UK.
- Baldwin, J.A., Powell, R., White, R.W. and Stipska, P. (2015) Using calculated chemical potential relationships to account for replacement of kyanite by symplectite in high pressure granulites. *Journal of Metamorphic Geology*, **33**, 311–330.
- Balluffi, R.W., Allen, S.M. and Carter, W.C. (2005) *Kinetics of Materials*. John Wiley & Sons Inc..
- Bethune, K. and Davidson, A. (1997) Grenvillian metamorphism of the Sudbury diabase dyke-swarm: From protolith to two-pyroxene–garnet coronite. *The Canadian Mineralogist*, **35**, 1191–1220.
- Boland, J. and Van Roermund, H. (1983) Mechanisms of exsolution in omphacites from high temperature, type b, eclogites. *Physics and Chemistry of Minerals*, **9**, 30–37.
- Brady, J. and McCallister, R. (1983) Diffusion data for clinopyroxenes from homogenization and self-diffusion experiments. *American Mineralogist*, **68**, 95–105.
- Cahn, J. (1959) The kinetics of cellular segregation reactions. *Acta Metallurgica*, **7**, 18–28.
- Cahn, J. and Hagel, W. (1962) Theory of pearlite reaction. Pp. 131–192 in: *Decomposition of Austenite by Diffusional Processes* (V.F. Zackay and H.I. Aaronson, editors). Interscience Publishers, New York.
- Callen, H. (1985) *Thermodynamics and an Introduction to Thermostatistics*, 2nd edition. John Wiley & Sons, Chichester, UK.
- Carlson, W.D. (1989) The significance of intergranular diffusion to the mechanism and kinetics of porphyroblast crystallization. *Contributions to Mineralogy and Petrology*, **103**, 1–24.
- Carlson, W.D. (1991) Competitive diffusion-controlled growth of porphyroblasts. *Mineralogical Magazine*, **55**, 317–330.
- Carlson, W.D. (2002) Scales of disequilibrium and rates of equilibration during metamorphism. *American Mineralogist*, **87**, 185–204.
- Carlson, W.D. (2011) Porphyroblast crystallization: linking processes, kinetics, and microstructures. *International Geology Review*, **53**, 406–445.
- Carlson, W.D. and Johnson, C.D. (1991) Coronal reaction textures in garnet amphibolites of the Llano uplift. *American Mineralogist*, **76**, 756–772.
- Carlson, W.D., Denison, C. and Ketcham, R.A. (1995) Controls on the nucleation and growth of porphyroblasts: kinetics from natural textures and numerical models. *Geological Journal*, **30**, 207–225.
- Carter, R. (1961) Mechanism of solid-state reaction between magnesium oxide and aluminum oxide and between magnesium oxide and ferric oxide. *Journal of the American Ceramical Society*, **44**, 116–120.

- Cashman, K.V. and Ferry, J.M. (1988) Crystal size distribution (CSD) in rocks and the kinetics and dynamics of crystallization. 3. Metamorphic crystallization. *Contributions to Mineralogy and Petrology*, **99**, 401–415.
- Chernoff, C.B. and Carlson, W.D. (1997) Disequilibrium for Ca during growth of pelitic garnet. *Journal of Metamorphic Geology*, **15**, 421–438.
- Chernoff, C.B. and Carlson, W.D. (1999) Trace element zoning as a record of chemical disequilibrium during garnet growth. *Geology*, **27**, 555–558.
- Christian, J.W. (2002) *The Theory of Transformations in Metals and Alloys*. Elsevier, Amsterdam.
- Cox, R. and Indares, A. (1999) Transformation of Fe-Ti gabbro to coronite, eclogite and amphibolite in the Baie du Nord segment, Manicouagan Imbricate Zone, eastern Grenville Province. *Journal of Metamorphic Geology*, **17**, 537–555.
- Cserhati, C., Balogh, Z., Csik, A., Langer, G. and Erdelyi, Z. (2008) Linear growth kinetics of nanometric silicides in Co/amorphous-Si and Co/CoSi/amorphous-Si thin films. *Journal of Applied Physics*, **104**, Art. No. 024311.
- Cutts, K.A., Stevens, G., Hoffmann, J.E., Buick, I.S., Frei, D. and Muenker, C. (2014) Paleo- to Mesoarchean polymetamorphism in the Barberton Granite-Greenstone Belt, South Africa: constraints from U-Pb monazite and Lu-Hf garnet geochronology on the tectonic processes that shaped the belt. *Geological Society of America Bulletin*, **126**, 251–270.
- Cygan, R.T. and Lasaga, A.C. (1982) Crystal growth and formation of chemical zoning in garnets. *Contributions to Mineralogy and Petrology*, **79**, 187–200.
- Daniel, C.G. and Spear, F.S. (1998) Three-dimensional patterns of garnet nucleation and growth. *Geology*, **26**, 503–506.
- Daniel, C.G. and Spear, F.S. (1999) The clustered nucleation and growth processes of garnet in regional metamorphic rocks from north-west Connecticut, USA. *Journal of Metamorphic Geology*, **17**, 503–520.
- de Capitani, C. and Brown, T.H. (1987) The computation of chemical equilibrium in complex systems containing non-ideal solutions. *Geochimica et Cosmochimica Acta*, **51**, 2639–2652.
- De Groot, S. and Mazur, S. (1984) *Non-Equilibrium Thermodynamics*. Dover Publications, New York.
- Deal, B. and Grove, A. (1965) General relationship for thermal oxidation of silicon. *Journal of Applied Physics*, **36**, 3770–3778.
- Degi, J., Abart, R., Török, K., Bali, E., Wirth, R. and Rhede, D. (2009) Symplectite formation during decompression induced garnet breakdown in lower crustal mafic granulite xenoliths: mechanisms and rates. *Contributions to Mineralogy and Petrology*, **159**, 293–314.
- Denison, C. and Carlson, W.D. (1997) Three-dimensional quantitative textural analysis of metamorphic rocks using high-resolution computed X-ray tomography: Part II. Application to natural samples. *Journal of Metamorphic Geology*, **15**, 45–57.
- Denison, C., Carlson, W.D. and Ketcham, R.A. (1997) Three-dimensional quantitative textural analysis of metamorphic rocks using high-resolution computed X-ray tomography: Part I. Methods and techniques. *Journal of Metamorphic Geology*, **15**, 29–44.
- Dohmen, R. and Milke, R. (2010) Diffusion in polycrystalline materials: grain boundaries, mathematical models, and experimental data, Pp. 921–970 in: *Diffusion in Minerals and Melts* (Y. Zhang and D.J. Cherniak, editors) Reviews in Mineralogy and Geochemistry, **72**. Mineralogical Society of America and the Geochemical Society, Washington, D.C.
- Dybkov, V. (1986) Reaction diffusion in heterogeneous binary systems. Part 2 Growth of the chemical compound layers at the interface between two elementary substances: two compound layers. *Journal of Materials Science*, **21**, 3085–3090.
- Farrell, H., Gilmer, G. and Suenaga, M. (1975) Diffusion mechanisms for growth of Nb₃Sn intermetallic layers. *Thin Solid Films*, **25**, 253–264.
- Faryad, S.W., Kachlik, V., Slama, J. and Hoinkes, G. (2015) Implication of corona formation in a metatroctolite to the granulite facies overprint of HP-UHP rocks in the Moldanubian Zone (Bohemian Massif). *Journal of Metamorphic Geology*, **33**, 295–310.
- Field, S. (2008) Diffusion, discontinuous precipitation, metamorphism, and metasomatism: The complex history of South African upper-mantle symplectites. *American Mineralogist*, **93**, 618–631.
- Fischer, F.D. and Simha, N.K. (2004) Influence of material flux on the jump relations at a singular interface in a

- multicomponent solid. *Acta Mechanica*, **171**, 213–223.
- Fischer, F.D., Svoboda, J. and Petryk, H. (2014) Thermodynamic extremal principles for irreversible processes in materials science. *Acta Materialia*, **67**, 1–20.
- Fischer, G. (1973) Nonequilibrium thermodynamics as a model for diffusion-controlled metamorphic processes. *American Journal of Science*, **273**, 897–924.
- Fisler, D. and Mackwell, S. (1994) Kinetics of diffusion-controlled growth of fayalite. *Physics and Chemistry of Minerals*, **21**, 156–165.
- Fisler, D., Mackwell, S. and Petsch, S. (1997) Grain boundary diffusion in enstatite. *Physics and Chemistry of Minerals*, **24**, 264–273.
- Florence, F.P. and Spear, F.S. (1991) Effects of diffusional modification of garnet growth zoning on P-T path calculations. *Contributions to Mineralogy and Petrology*, **107**, 487–500.
- Foster, Jr., C.T. (1981) A thermodynamic model of mineral segregations in the lower sillimanite zone near Rangeley, Maine. *American Mineralogist*, **66**, 260–277.
- Foster, Jr., C.T. (1999) Forward modeling of metamorphic textures. *The Canadian Mineralogist*, **37**, 415–429.
- Frantz, J. and Mao, H. (1976) Bimetasomatism resulting from intergranular diffusion. 1. Theoretical-model for monomineralic reaction zone sequences. *American Journal of Science*, **276**, 817–840.
- Frantz, J. and Mao, H. (1979) Bimetasomatism resulting from intergranular diffusion. 2. Prediction of multi-mineralic zone sequences. *American Journal of Science*, **279**, 302–323.
- Fukuyama, M., Nishiyama, T., Urata, K. and Mori, Y. (2006) Steady-diffusion modelling of a reaction zone between a metamorphosed basic dyke and a marble from Hirao-dai, Fukuoka, Japan. *Journal of Metamorphic Geology*, **24**, 153–168.
- Gaidies, F. (2017) Nucleation in geological materials. Pp. 447–371 in: *Mineral Reaction Kinetics: Microstructures, Textures and Chemical Compositions* (R. Abart and W. Heinrich, editors). EMU Notes in Mineralogy, **16**. European Mineralogical Union and the Mineralogical Society of Great Britain & Ireland, London.
- Gaidies, F., de Capitani, C. and Abart, R. (2008a) THERIA G: a software program to numerically model prograde garnet growth. *Contributions to Mineralogy and Petrology*, **155**, 657–671.
- Gaidies, F., de Capitani, C., Abart, R. and Schuster, R. (2008b) Prograde garnet growth along complex P-T-t paths: results from numerical experiments on polyphase garnet from the Wolz Complex (Austroalpine Basement). *Contributions to Mineralogy and Petrology*, **155**, 673–688.
- Gaidies, F., Krenn, E., de Capitani, C. and Abart, R. (2008c) Coupling forward modelling of garnet growth with monazite geochronology: an application to the Rappold Complex (Austroalpine crystalline basement). *Journal of Metamorphic Geology*, **26**, 775–793.
- Gaidies, F., Pattison, D.R.M. and de Capitani, C. (2011) Toward a quantitative model of metamorphic nucleation and growth. *Contributions to Mineralogy and Petrology*, **162**, 975–993.
- Gaidies, F., Petley-Ragan, A., Chakraborty, S., Dasgupta, S. and Jones, P. (2015) Constraining the conditions of Barrovian metamorphism in Sikkim, India: P-T-t paths of garnet crystallization in the Lesser Himalayan Belt. *Journal of Metamorphic Geology*, **33**, 23–44.
- Gallien, F., Mogessie, A. and Bjerg, E. (2013) On the origin of multilayer coronas between olivine and plagioclase at the gabbro-granulite transition, Valle Fertil-la Huerta ranges, San Juan Province, Argentina. *Journal of Metamorphic Geology*, **30**, 281–302.
- Gamsjäger, E. (2007) A note on the contact conditions at migrating interfaces. *Acta Materialia*, **55**, 4823–4833.
- Gardés, E. and Heinrich, W. (2011) Growth of multilayered polycrystalline reaction rims in the MgO-SiO₂ system, part II: modelling. *Contributions to Mineralogy and Petrology*, **162**, 37–49.
- Gardés, E., Wunder, B., Wirth, R. and Heinrich, W. (2011) Growth of multilayered polycrystalline reaction rims in the MgO-SiO₂ system, part I: experiments. *Contributions to Mineralogy and Petrology*, **161**, 1–12.
- Gardés, E., Wunder, B., Marquardt, K. and Heinrich, W. (2012) The effect of water on intergranular mass transport: new insights from diffusion-controlled reaction rims in the MgO-SiO₂ system. *Contributions to Mineralogy and Petrology*, **164**, 1–16.
- George, F. and Gaidies, F. (2016) Characterization of a garnet population from the Sikkim Himalaya: implications for the mechanisms and rates of porphyroblast crystallization. *Geophysical Research Abstracts*, **18**, EGU2016-5040.

- Gittins, J., Fawcett, J., Brooks, C. and Rucklidge, J. (1980) Intergrowths of nepheline, potassium feldspar and kalsilite-potassium feldspar: A re-examination of the 'pseudo-leucite problem'. *Contributions to Mineralogy and Petrology*, **73**, 119–126.
- Glicksman, M.E. (2000) *Diffusion in Solids*. John Wiley & Sons, Chichester, UK.
- Gösele, U. and Tu, K. (1982) Growth kinetics of planar binary diffusion couples: "thin-film case" versus "bulk cases". *Journal of Applied Physics*, **53**, 3252–3260.
- Götze, L., Abart, R., Rybacki, E., Keller, L., Petrishcheva, E. and Dresen, G. (2010) Reaction rim growth in the system MgO-Al₂O₃-SiO₂ under uniaxial stress. *Mineralogy and Petrology*, **99**, 2263–2277.
- Götze, L., Abart, R., Milke, R., Schorr, S., Zizak, I., Dohmen, R. and Wirth, R. (2014) Growth of magnesio-aluminate spinel in thin film geometry – in-situ monitoring using synchrotron X-ray diffraction and thermodynamic model. *Physics and Chemistry of Minerals*, **99**, 999–1001.
- Grant, S. (1988) Diffusion-models for corona formation in metagabbros from the western-Grenville-province, Canada. *Contributions to Mineralogy and Petrology*, **98**, 49–63.
- Grant, T., Milke, R. and Wunder, B. (2014) Experimental reactions between olivine and orthopyroxene with phonolite melt: implications for the origins of hydrous diopside + amphibole + phlogopite bearing metasomatic veins. *Contributions to Mineralogy and Petrology*, **168**, 1073.
- Harley, S. and Santosh, M. (1995) Wollastonite at Muliyam, Kerala, southern India – a reassessment of CO₂-infiltration and charnockite formation at a classic locality. *Contributions to Mineralogy and Petrology*, **120**, 83–94.
- Harlov, D. and Milke, R. (2002) Stability of corundum + quartz relative to kyanite and sillimanite at high temperature and pressure. *American Mineralogist*, **87**, 424–432.
- Heinrich, W. (1993) Fluid infiltration through metachert layers at the contact aureole of the Bufa-del-Diente intrusion, northeast Mexico – implications for wollastonite formation and fluid immiscibility. *American Mineralogist*, **78**, 804–818.
- Hillert, M. (1972) On theories of growth during discontinuous precipitation. *Metallurgical Transactions*, **2**, 2729–2741.
- Hirsch, D.M. (2000) *Quantitative studies of porphyroblastic textures*. Dissertation, University of Texas at Austin, Texas, USA.
- Hirsch, D.M. (2008) Controls on porphyroblast size along a regional metamorphic field gradient. *Contributions to Mineralogy and Petrology*, **155**, 401–415.
- Hirsch, D.M. (2011) Reduce3D: A tool for three-dimensional spatial statistical analysis of crystals. *Geosphere*, **7**, 724–732.
- Hirsch, D.M. and Carlson, W.D. (2006) Variations in rates of nucleation and growth of biotite porphyroblasts. *Journal of Metamorphic Geology*, **24**, 763–777.
- Hirsch, D.M., Ketcham, R.A. and Carlson, W.D. (2000) An evaluation of spatial correlation functions in textural analysis of metamorphic rocks. *Geological Materials Research*, **2**, 1–42.
- Hollister, L.S. (1966) Garnet zoning: an interpretation based on the Rayleigh fractionation model. *Science*, **154**, 1647–1651.
- Hoschek, G. (2013) Garnet zonation in metapelitic schists from the Eclogite Zone, Tauern Window, Austria: comparison of observed and calculated profiles. *European Journal of Mineralogy*, **25**, 615–629.
- Illian, J., Penttinen, P., Stoyan, H. and Stoyan, D. (2008) *Statistical Analysis and Modelling of Spatial Point Patterns*. J. Wiley & Sons, Chichester, UK.
- Indares, A. and Rivers, T. (1995) Textures, metamorphic reactions and thermobarometry of eclogitized metagabbros - a proterozoic example. *European Journal of Mineralogy*, **7**, 43–56.
- Jeřábek, P., Abart, R., Rybacki, E. and Habler, G. (2014) Microstructure and texture evolution during growth of magnesio-aluminate spinel at corundum–periclase interfaces under uniaxial load: the effect of loading on reaction progress. *American Journal of Science*, **314**, 1–26.
- Joachim, B., Gardes, E., Abart, R. and Heinrich, W. (2011) Experimental growth of akermanite reaction rims between wollastonite and monticellite: evidence for volume diffusion control. *Contributions to Mineralogy and Petrology*, **161**, 369–399.
- Joachim, B., Gardes, E., Abart, R., Velikov, B. and Heinrich, W. (2012) Experimental growth of diopside + merwinite reaction rims: The effect of water on microstructure development. *American Mineralogist*, **97**,

- 220–230.
- Joesten, R. (1977) Evolution of mineral assemblage zoning in diffusion metamorphism. *Geochimica et Cosmochimica Acta*, **41**, 649–670.
- Joesten, R. (1986) The role of magmatic reaction, diffusion and annealing in the evolution of coronitic microstructure in troctolitic gabbro from Risør, Norway. *Mineralogical Magazine*, **50**, 441–467.
- Joesten, R. (1991) Local equilibrium in metasomatic processes revisited – diffusion-controlled growth of chert nodule reaction rims in dolomite. *American Mineralogist*, **76**, 743–755.
- Joesten, R. and Fisher, G. (1988) Kinetics of diffusion-controlled mineral growth in the Christmas Mountains (Texas) contact aureole. *Geological Society of America Bulletin*, **100**, 714–732.
- Johnson, C. and Carlson, W. (1990) The origin of olivine-plagioclase coronas in metagabbros from the Adirondack mountains, New-York. *Journal of Metamorphic Geology*, **8**, 697–717.
- Jones, K.A. and Galwey, A.K. (1966) Size distribution, composition, and growth kinetics of garnet crystals in some metamorphic rocks from the west of Ireland. *Quarterly Journal of the Geological Society*, **122**, 29–44.
- Keller, L., Abart, R., Stunitz, H. and De Capitani, C. (2004) Deformation, mass transfer and mineral reactions in an eclogite facies shear zone in a polymetamorphic metapelite (Monte Rosa nappe, Western Alps). *Journal of Metamorphic Geology*, **22**, 97–118.
- Keller, L., Abart, R., Wirth, R., Schmid, D. and Kunze, K. (2006) Enhanced mass transfer through short-circuit diffusion: Growth of garnet reaction rims at eclogite facies conditions. *American Mineralogist*, **91**, 1024–1038.
- Keller, L., Wirth, R., Rhede, D., Kunze, K. and Abart, R. (2008) Asymmetrically zoned reaction rims: assessment of grain boundary diffusivities and growth rates related to natural diffusion-controlled mineral reactions. *Journal of Metamorphic Geology*, **26**, 99–120.
- Keller, L., Götze, L., Rybacki, E., Dresen, G. and Abart, R. (2010) Enhancement of solid-state reaction rates by non-hydrostatic stress effects on polycrystalline diffusion kinetics. *American Mineralogist*, **95**, 1399–1407.
- Kelly, E.D., Carlson, W.D. and Ketcham, R.A. (2013) Crystallization kinetics during regional metamorphism of porphyroblastic rocks. *Journal of Metamorphic Geology*, **31**, 963–979.
- Ketcham, R.A. and Carlson, W.D. (2001) Acquisition, optimization and interpretation of X-ray computed tomographic imagery: applications to the geosciences. *Computers and Geosciences*, **27**, 381–400.
- Ketcham, R.A. and Carlson, W.D. (2012) Numerical simulation of diffusion-controlled nucleation and growth of porphyroblasts. *Journal of Metamorphic Geology*, **30**, 489–512.
- Ketcham, R.A., Meth, C.E., Hirsch, D.M. and Carlson, W.D. (2005) Improved methods for quantitative analysis of three-dimensional porphyroblastic textures. *Geosphere*, **1**, 42–59.
- Khisina, N.R., Wirth, R., Abart, R., Rhede, D. and Heinrich, W. (2013) Oriented chromite-diopside symplectic inclusions in olivine from lunar regolith delivered by “Luna-24” mission. *Geochimica et Cosmochimica Acta*, **104**, 84–98.
- Konrad-Schmolke, M., Zack, T., O’Brien, P.J. and Jacob, D.E. (2008) Combined thermodynamic and rare earth element modelling of garnet growth during subduction: Examples from ultrahigh-pressure eclogite of the Western Gneiss Region, Norway. *Earth and Planetary Science Letters*, **272**, 488–498.
- Korzhinskii, D. (1959) *Physicochemical Basis of the Analysis of the Paragenesis of Minerals*. Consultants Bureau.
- Korzhinskii, D. (1970) *Theory of Metasomatic Zoning*. Clarendon Press, Oxford, UK.
- Kretz, R. (1966) Grain size distribution for certain metamorphic minerals in relation to nucleation and growth. *Journal of Geology*, **75**, 147–173.
- Kretz, R. (1969) On the spatial distribution of crystals in rocks. *Lithos*, **2**, 39–66.
- Kretz, R. (1973) Kinetics of the crystallization of garnet at two localities near Yellowknife. *The Canadian Mineralogist*, **12**, 1–20.
- Kretz, R. (1974) Some models for the rate of crystallization of garnet in metamorphic rocks. *Lithos*, **7**, 123–131.
- Kretz, R. (1993) A garnet population in Yellowknife schist, Canada. *Journal of Metamorphic Geology*, **11**, 101–120.
- Kretz, R. (1994) *Metamorphic Crystallization*. Wiley, Chichester, UK.
- Larikova, T.L. and Zaraisky, G.P. (2009) Experimental modelling of corona textures. *Journal of Metamorphic*

- Geology*, **27**, 139–151.
- Lasaga, A. (1998) *Kinetic Theory in the Earth Sciences*. Princeton University Press, Princeton, New Jersey, USA.
- Liu, M., Peterson, J. and Yund, R. (1997) Diffusion-controlled growth of albite and pyroxene reaction rims. *Contributions to Mineralogy and Petrology*, **126**, 217–223.
- Loomis, T.P. (1982) Numerical simulation of the disequilibrium growth of garnet in chlorite-bearing aluminous pelitic rocks. *The Canadian Mineralogist*, **20**, 411–423.
- Loomis, T.P. (1986) Metamorphism of metapelites – calculations of equilibrium assemblages and numerical simulations of the crystallization of garnet. *Journal of Metamorphic Geology*, **4**, 201–229.
- Loomis, T.P. and Nimick, F.B. (1982) Equilibrium in Mn-Fe-Mg aluminous pelitic compositions and the equilibrium growth of garnet. *The Canadian Mineralogist*, **20**, 393–410.
- Lucassen, F., Dulski, P., Abart, R., Franz, G., Rhede, D. and Romer, R.L. (2010) Redistribution of HFS elements during rutile replacement by titanite. *Contributions to Mineralogy and Petrology*, **160**, 279–295.
- Martyushev, L. and Seleznev, V. (2006) Maximum entropy production principle in physics, chemistry and biology. *Physics Reports*, **426**, 1–45.
- Mehrer, H. (2007) *Diffusion in Solids – Fundamentals, Methods, Materials, Diffusion-Controlled Processes*. Springer Series in Solid State Sciences, **155**. Berlin.
- Messiga, B. and Bettini, E. (1990) Reactions behavior during kelyphite and symplectite formation - a case-study of mafic granulites and eclogites from the Bohemian massif. *European Journal of Mineralogy*, **2**, 125–144.
- Milke, R. and Heinrich, W. (2002) Diffusion-controlled growth of wollastonite rims between quartz and calcite: Comparison between nature and experiment. *Journal of Metamorphic Geology*, **20**, 467–480.
- Milke, R., Wiedenbeck, M. and Heinrich, W. (2001) Grain boundary diffusion of Si, Mg, and O in enstatite reaction rims: a SIMS study using isotopically doped reactants. *Contributions to Mineralogy and Petrology*, **142**, 15–26.
- Milke, R., Dohmen, R., Becker, H.-W. and Wirth, R. (2007) Growth kinetics of enstatite reaction rims studied on nano-scale, part I: Methodology, microscopic observations and the role of water. *Contributions to Mineralogy and Petrology*, **154**, 519–533.
- Milke, R., Kolzer, K., Koch-Müller, M. and Wunder, B. (2009a) Orthopyroxene rim growth between olivine and quartz at low temperatures (750–950°C) and low water concentration. *Mineralogy and Petrology*, **97**, 223–232.
- Milke, R., Abart, R., Kunze, K., Koch-Mueller, M., Schmid, D. and Ulmer, P. (2009b) Matrix rheology effects on reaction rim growth I: evidence from orthopyroxene rim growth experiments. *Journal of Metamorphic Geology*, **27**, 71–82.
- Milke, R., Abart, R., Keller, L. and Rhede, D. (2011) The behavior of Mg, Fe, and Ni during the replacement of olivine by orthopyroxene: experiments relevant to mantle metasomatism. *Mineralogy and Petrology*, **103**, 1–8.
- Milke, R., Neusser, G., Kolzer, K. and Wunder, B. (2013) Very little water is necessary to make a dry solid silicate system wet. *Geology*, **41**, 247–250.
- Milke, R., Heinrich, W., Götze, L. and Schorr, S. (2017) New avenues in experimentation on diffusion-controlled mineral reactions Pp. 5–36 in: *Mineral Reaction Kinetics: Microstructures, Textures and Chemical Compositions* (R. Abart and W. Heinrich, editors). EMU Notes in Mineralogy, **16**. European Mineralogical Union and Mineralogical Society of Great Britain & Ireland, London.
- Miyazaki, K. (1991) Ostwald ripening of garnet in high P/T metamorphic rocks. *Contributions to Mineralogy and Petrology*, **108**, 118–128.
- Miyazaki, K. (1996) A numerical simulation of textural evolution due to Ostwald ripening in metamorphic rocks: A case for small amount of volume of dispersed crystals. *Geochimica et Cosmochimica Acta*, **60**, 277–290.
- Miyazaki, K. (2015) Diffusion-controlled growth and degree of disequilibrium of garnet porphyroblasts: is diffusion-controlled growth of porphyroblasts common? *Progress in Earth and Planetary Science*, **2**, 25.
- Mongkoltip, P. and Ashworth, J. (1983) Quantitative estimation of an open-system symplectite-forming reaction – restricted diffusion of Al and Si in coronas around olivine. *Journal of Petrology*, **24**, 635–661.
- Morishita, T. and Arai, S. (2003) Evolution of spinel-pyroxene symplectite in spinel-lherzolites from the

- Horoman complex, Japan. *Contributions to Mineralogy and Petrology*, **144**, 509–522.
- Moynihan, D.P. and Pattison, D.R.M. (2013) An automated method for the calculation of P-T paths from garnet zoning, with application to metapelitic schist from the Kootenay Arc, British Columbia, Canada. *Journal of Metamorphic Geology*, **31**, 525–548.
- Mullins, W.W. and Sekerka, R.F. (1964) Stability of a planar interface during solidification of a dilute binary alloy. *Journal of Applied Physics*, **35**, 444–451.
- Nishi, M., Nishihara, Y. and Irifune, T. (2013) Growth kinetics of MgSiO₃ perovskite reaction rim between stishovite and periclase up to 50 GPa and its implication for grain boundary diffusivity in the lower mantle. *Earth and Planetary Science Letters*, **377**, 191–198.
- Nishiyama, T. (1983) Steady diffusion model for olivine – plagioclase corona growth. *Geochimica et Cosmochimica Acta*, **47**, 283–294.
- Obata, M. (2011) Kelyphite and symplectite: textural and mineralogical diversities and universality, and a new dynamic view of their structural formation, Pp. 93–122 in: *New Frontiers in Tectonic Research - General Problems, Sedimentary Basins and Island Arcs* (E.V. Sharkov, editor). In Tech Publishers, Croatia.
- Obata, M. and Ozawa, K. (2011) Topotaxial relationships between spinel and pyroxene in kelyphite after garnet in mantle-derived peridotites and their implications to reaction mechanism and kinetics. *Mineralogy and Petrology*, **101**, 217–224.
- Obata, M., Ozawa, K., Nakamura, K. and Miyake, A. (2013) Isochemical breakdown of garnet in orogenic garnet peridotite and its implication to reaction kinetics. *Mineralogy and Petrology*, **107**, 881–895.
- Onsager, L. (1931) Reciprocal relations in irreversible processes. I. *Physical Review*, **37**, 405–426.
- Pattison, D.R.M. and Debuhr, C.L. (2015) Petrology of metapelites in the Bugaboo aureole, British Columbia, Canada. *Journal of Metamorphic Geology*, **33**, 437–462.
- Petley-Ragan, A., Gaidies, F. and Pattison, D.R.M. (2016) A statistical analysis of the distribution of cordierite and biotite in hornfels from the Bugaboo contact aureole: implications for the kinetics of porphyroblast crystallization. *Journal of Metamorphic Geology*, **34**, 85–101.
- Petrishcheva, E. and Abart, R. (2017) Interfaces. Pp. 295–345 in: *Mineral Reaction Kinetics: Microstructures, Textures and Chemical Compositions* (R. Abart and W. Heinrich, editors). EMU Notes in Mineralogy, **16**. European Mineralogical Union and Mineralogical Society of Great Britain & Ireland, London.
- Pfeiffer, T. and Schmalzried, H. (1989) Spinel formation – a detailed analysis. *Zeitschrift für Physikalische Chemie Neue Folge*, **161**, 1–17.
- Phillips, E.R. (1974) Myrmekite – one hundred years later. *Lithos*, **7**, 181–194.
- Prigogine, I. (1967) *Introduction to Thermodynamics of Irreversible Processes*. Interscience Publishers, New York.
- Proyer, A., Rolfo, F., Castelli, D. and Compagnoni, R. (2014) Diffusion-controlled metamorphic reaction textures in an ultrahigh-pressure impure calcite marble from Dabie Shan, China. *European Journal of Mineralogy*, **26**, 25–40.
- Remmert, P., Heinrich, W., Wunder, B., Morales, L., Wirth, R., Rhede, D. and Abart, R. (2017) Experimental symplectite formation in the system CaO-MgO-SiO₂: Influence of temperature and water content on reaction microstructures. In prep.
- Ripley, B.D. (1981) *Spatial Statistics*. Wiley, New York.
- Rossi, R. and Fulrath, R. (1963) Epitaxial growth of spinel by reaction in the solid state. *Journal of the American Ceramic Society*, **46**, 145–149.
- Schmalzried, H. (1974) Solid-state reactions between oxides. Pp. 83–108 in: *Defects and Transport in Oxides* (M. Seltzer and R. Jaffee, editors), Plenum Press, New York.
- Schmid, D.W., Abart, R., Podladchikov, Y.Y. and Milke, R. (2009) Matrix rheology effects on reaction rim growth II: coupled diffusion and creep model. *Journal of Metamorphic Geology*, **27**, 83–91.
- Schwarz, J.-O., Engi, M. and Berger, A. (2011) Porphyroblast crystallization kinetics: the role of the nutrient production rate. *Journal of Metamorphic Geology*, **29**, 497–512.
- Scott, J.M., Konrad-Schmolke, M., O'Brien, P.J. and Guenter, C. (2013) High-T, Low-P formation of rare olivine-bearing symplectites in Variscan eclogite. *Journal of Petrology*, **54**, 1375–1398.
- Smigelskas, A. and Kirkendall, E. (1947) Zinc diffusion in alpha-brass. *Transactions of The American Institute of Mining and Metallurgical Engineers*, **171**, 130–142.

- Spacek, P., Ackerman, L., Habler, G., Abart, R. and Ulrych, J. (2013) Garnet breakdown, symplectite formation and melting in basanite-hosted peridotite xenoliths from Zinst (Bavaria, Bohemian Massif). *Journal of Petrology*, **54**, 1691–1723.
- Spear, F.S. (1993) *Metamorphic Phase Equilibria and Pressure-Temperature-Time Paths*. Monograph, **1**. Mineralogical Society of America, Washington, D.C.
- Spear, F.S. and Daniel, C.G. (1998) Three-dimensional imaging of garnet porphyroblast sizes and chemical zoning: nucleation and growth history in the garnet zone. *Geological Materials Research*, **1**, 1–44.
- Spear, F.S. and Daniel, C.G. (2001) Diffusion control of garnet growth, Harpswell Neck, Maine, USA. *Journal of Metamorphic Geology*, **19**, 179–195.
- Spear, F.S. and Florence, F.P. (1992) Thermobarometry in granulites: pitfalls and new approaches. *Precambrian Research*, **55**, 209–241.
- Spear, F.S., Kohn, M.J., Florence, F.P. and Menard, T. (1991a) A model for garnet and plagioclase growth in pelitic schists: implications for thermobarometry and P-T path determinations. *Journal of Metamorphic Geology*, **8**, 683–696.
- Spear, F.S., Peacock, S.M., Kohn, M.J., Florence, F.P. and Menard, T. (1991b) Computer programs for petrologic P-T-t path calculations. *American Mineralogist*, **76**, 2009–2012.
- Spry, A. (1969) *Metamorphic Textures*. Pergamon Press, Oxford, UK.
- Strauss, D.J. (1975) A model for clustering. *Biometrika*, **62**, 467–475.
- Svoboda, J. and Fischer, F. (2013) A new computational treatment of reactive diffusion in binary systems. *Computational Materials Science*, **78**, 39–46.
- Svoboda, J. and Turek, I. (1991) On diffusion-controlled evolution of closed solid-state thermodynamic systems at constant temperature and pressure. *Philosophical Magazine Part B*, **64**, 749–759.
- Svoboda, J., Turek, I. and Fischer, F. (2005) Application of the thermodynamic extremal principle to modeling of thermodynamic processes in material sciences. *Philosophical Magazine*, **85**, 3699–3707.
- Svoboda, J., Fischer, F. and Fratzl, P. (2006a) Diffusion and creep in multi-component alloys with non-ideal sources and sinks for vacancies. *Acta Materialia*, **54**, 3043–3053.
- Svoboda, J., Gasmjaeger, E., Fischer, F. and Kozeschnik, E. (2006b) Modeling of kinetics of diffusive phase transformation in binary systems with multiple stoichiometric phases. *Journal of Phase Equilibria and Diffusion*, **27**, 622–628.
- Svoboda, J., Fischer, F. and Abart, R. (2010) Modeling of diffusional phase transformation in multi-component systems with stoichiometric phases. *Acta Materialia*, **58**, 2905–2911.
- Svoboda, J., Fischer, F. and Abart, R. (2011) Modeling the role of sources and sinks for vacancies on the kinetics of diffusive phase transformation in binary systems with several stoichiometric phases. *Philosophical Magazine*, **92**, 67–76.
- Svoboda, J., Fischer, F. and Kozeschnik, E. (2017) Thermodynamic modelling of irreversible processes. Pp. 181–214 in: *Mineral Reaction Kinetics: Microstructures, Textures and Chemical Compositions* (R. Abart and W. Heinrich, editors). EMU Notes in Mineralogy, **16**. European Mineralogical Union and Mineralogical Society of Great Britain & Ireland, London.
- Tajcmanova, L., Abart, R., Neusser, G. and Rhede, D. (2011) Growth of plagioclase rims around metastable kyanite during decompression of high-pressure felsic granulites (Bohemian Massif). *Journal of Metamorphic Geology*, **29**, 1003–1018.
- Tan, W., Wang, C.Y., He, H., Xing, C., Liang, X. and Dong, H. (2015) Magnetite-rutile symplectite derived from ilmenite-hematite solid solution in the Xinjie Fe-Ti oxide-bearing, mafic-ultramafic layered intrusion (SW China). *American Mineralogist*, **100**, 2348–2351.
- Thompson, J.B. (1959) Local equilibrium in metasomatic processes. Pp. 427–457 in: *Researches in Geochemistry*, **1** (P.H. Abelson, editor). Wiley, New York.
- van Loo, F., Pleumeekers, M. and van Dal, M. (2000) Intrinsic diffusion and Kirkendall effect in Ni-Pd and Fe-Pd solid solutions. *Acta Materialia*, **48**, 385–396.
- Vernon, R. (2004) *A Practical Guide to Rock Microstructure*. Cambridge, University Press, Cambridge, UK.
- Watson, E. and Price, J. (2001) Kinetics of the reaction $\text{MgO} + \text{Al}_2\text{O}_3 = \text{MgAl}_2\text{O}_4$ and Al-Mg interdiffusion in spinel at 1200–2000°C and 1.0–4.0 GPa. *Geochimica et Cosmochimica Acta*, **66**, 2123–2138.
- Yuguchi, T. and Nishiyama, T. (2008) The mechanism of myrmekite formation deduced from steady-diffusion

- modeling based on petrography: Case study of the Okueyama granitic body, Kyushu, Japan. *Lithos*, **106**, 237–260.
- Yund, R. (1997) Rates of grain boundary diffusion through enstatite and forsterite reaction rims. *Contributions to Mineralogy and Petrology*, **126**, 224–236.
- Zaraysky, G., Balashov, V. and Lebedeva, M. (1989) Macrokinetic model of metasomatic zonality. *Geokhimiya*, **10**, 1386–1395.
- Zener, C. (1949) Theory of growth of spherical precipitates from solid solution. *Journal of Applied Physics*, **20**, 950–953.
- Zener, C. (1958) Kinetics of the decomposition of austenite. *Transactions of The American Institute of Mining and Metallurgical Engineers*, **167**, 550.
- Zhang, R. and Liou, J. (1997) Partial transformation of gabbro to coesite-bearing eclogite from Yangkou, the Sulu terrane, eastern China. *Journal of Metamorphic Geology*, **15**, 183–202.
- Ziegler, H. (1961) Two extremal principles in irreversible thermodynamics. *Ingenieur Archive*, **30**, 410–416.